Plastic deformation of cubic zirconia single crystals:
The influence of the orientation of compression axis and
yttria stabilizer content

Dissertation

Zur Erlangung des akademischen Grades

Doctor rerum naturalium (Dr. rer. Nat.)

Vorgelegt der Mathematisch-Naturwissenschaftlich-Technischen Fakultät
(mathematisch-naturwissenschaftlicher Bereich)
der Martin-Luther-Universität Halle-Wittenberg

von Alexander Tikhonovsky

geb. am 01.04.1974 in Kiew

Gutachter:

1. Prof. Dr. H.-R. Höche
2. Prof. Dr. U. Messerschmidt
3. Prof. Dr. M. Rühle

Die öffentliche Verteidigung der Dissertation fand am 27.04.2001 statt.

Table of contents

1.   Introduction

Cubic zirconia (c-ZrO$_2$) is an industrially attractive material that has a wide range of applications. It is used in automotive sensors [1] and solid electrolyte fuel cells [2, 3] because of its high-temperature ionic conductivity. Besides, cubic zirconia is known to be widely utilized in jewelry as a remarkable substitute of natural diamonds. Other phases of zirconium dioxide, i.e. the tetragonal and monoclinic modifications, are of high interest due to the transformation toughening of materials involving the tetragonal-to-monoclinic transformation [5, 6] as well as ferroelastic behavior of the metastable t'-ZrO$_2$ phase [7]. Both phenomena can increase the strength and fracture toughness of zirconia-containing ceramics. The former is used in zirconia toughened alumina alloys (ZTA) known for their high wear resistance [8]. The tetragonal phase may also be dispersed as precipitates in a cubic zirconia matrix leading to the so-called partially stabilized zirconia (PSZ). Owing to precipitation hardening, these materials have a high flow stress up to high temperatures [9]. That the plastic properties of the different zirconia-based materials can be understood, an in-depth background in the microprocesses of deformation of cubic zirconia single crystals is indispensable, mostly because the material is a frequently used component of other ceramics.

There have been several attempts of investigating plastic deformation of cubic zirconia single crystals so far, and during different periods of time [4, 10-27]. Cubic zirconia is a high-temperature phase of zirconia. It can be stabilized down to room temperature by adding aliovalent oxides, particularly Y$_2$O$_3$ or CaO [28-30]. The previous papers on deformation of cubic zirconia single crystals dealt primarily with the dependence of the flow stress on the temperature and the concentration of the stabilizer as well as the defect microstructure of deformed specimens, i.e. with studies of the dislocation structure and of point defects [31-35]. From the studies of the dislocation structure and macroscopic deformation parameters, several dislocation mechanisms have been identified (for a review, see [17]). The mechanisms govern the flow stress of the zirconia single crystals at different temperatures. These are lattice friction at low temperatures, thermally activated overcoming of localized obstacles

and athermal long-range dislocation interactions at intermediate temperatures, and dislocation recovery at high temperatures.

In spite of the substantial amount of work done on the plastic deformation of cubic zirconia, the basic deformation processes are still incompletely understood. Firstly, most of the former studies were performed at high temperatures, particularly at 1400°C. Only the experiments of Teracher et al. [15] under a confining pressure and of the plasticity group at the Max Planck Insitute in Halle [4, 17-22, 46, 47] span the temperature range below about 1200°C revealing the dislocation mechanisms listed above. However, the latter experiments are restricted mostly to a single specimen orientation and a single concentration of the yttria stabilizer. Therefore, it is not clear whether these mechanisms act on all possible slip systems in zirconia. Secondly, very little is known about the ways that yttria dopant influences the flow stress. In view of this, the objective of this thesis is to carry out a detailed study on the plastic deformation of c-ZrO$_2$ with two main series of experiments:

- activation of other slip systems by applying another sample orientation with the same yttria concentration as that done so far in [4] and the related papers;
- using other (higher) stabilizer concentrations with the same sample orientation as that done so far.

To achieve these goals, compression experiments are conducted in air at a constant strain rate at various temperatures. The microstructure after deformation is investigated by transmission electron microscopy. It was tried to attain experimental temperatures as low as possible, taking due account that cubic zirconia single crystals is very brittle at these temperatures. All the experiments are aimed at clarifying the deformation mechanisms on different slip systems of cubic zirconia and at the part of the yttria stabilizer in controlling the flow stress.

2.   Introduction to plastic deformation of crystals

As we know from fundamentals of plastic deformation of crystalline solids (e.g. [36]), Hooke's law is valid only in the elastic region of deformation. With increasing stress, the proportionality between the stress and strain gradually vanishes, and a range of plasticity occurs. Unlike the elastic range where deformation is fully reversible, applying a stress in the anelastic region results in a permanent plastic strain.

2.1. Microscopic models of plastic deformation of crystalline solids

2.1.1. Critical resolved shear stress

In crystalline materials, plastic deformation usually occurs by glide on slip planes along certain slip directions. A slip plane and a slip direction constitute a slip system. Glide can thus be understood as sliding or successive displacement of one plane of ato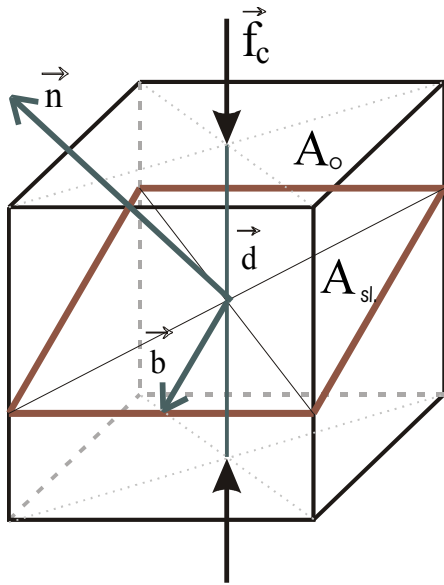ms over another one in a certain direction. That a dislocation can start moving on its glide plane, a characteristic shear stress is required. Consider a cubic crystal illustrated in Fig. 2.1.1. Let it be deformed in compression, $\vec{f}_c$ being a compressive force applied normal to the face A_o of the crystal. This produces a stress $\sigma = f_c / A_o$. Assume a dislocation on a slip plane $A_{sl.}$ with the Burgers vector $\vec{b}$ and a force $\vec{f}_b$ acting along its direction. The shear stress resolved on the slip plane $A_{sl.}$ due to the applied stress equals

Fig. 2.1.1. Definition of the orientation factor

$$\tau = \frac{\vec{f}_b}{A_{sl.}} = \frac{\vec{f}_c}{A_o} \cos(\vec{b},\vec{d}) \cos(\vec{n},\vec{d}) \qquad (2.1.1)$$

where $\vec{d}$ is the direction of compression axis, $\vec{n}$ is the normal to the slip plane. This equation is Schmid's law [37], and the product of cosines is called the orientation factor m_s. Consequently, eq. (2.1.1.) becomes

$$\tau = \sigma \times m_s \qquad (2.1.2)$$

3

with

$$m_s = \cos(\vec{b}, \vec{d}) \cos(\vec{n}, \vec{d}) \qquad (2.1.3)$$

It is possible to define a critical resolved shear stress (CRSS), above which the plastic deformation sets in as slip on a given slip plane.

Microscopically, slip is realized by the motion of line defects in the crystal structure, that is dislocations. While moving through a crystal, dislocations bring about the plastic strain $\varepsilon_{pl.}$. If moving dislocations of a density ρ_m are displaced by a distance x each, the plastic strain will be $\varepsilon_{pl.} = m_s \rho_m bx$. The derivation of this equation with respect to time yields the Orowan equation

$$\dot{\varepsilon}_{pl.} = m_s \rho_m bv \qquad (2.1.4)$$

where v is the velocity of the moving dislocations. The Orowan equation establishes a direct connection between the macroscopic parameter $\dot{\varepsilon}_{pl.}$ and the microscopic one v.

2.1.2. Thermal activation of dislocation motion

Consider a dislocation gliding in the x direction under an applied resolved shear stress τ which gives rise to a force τb per unit length of the line (for a review, see [38]). Assume the dislocation encounters obstacles, each of which produces a resisting force f_r, as sketched in Fig. 2.1.2. The forces depend on the position of the dislocation with respect to the obstacle. The obstacles can be of different nature. Let the spacing of the obstacles along the dislocation line be l, so that the applied forward force on the line per obstacle is τbl. At the temperature of 0 K, glide will cease if τbl is less than the obstacle strength f_{max}, and the dislocation line will stop at the position x_1. In order to overcome the barrier, the line must move to x_2, which can occur on account of thermal atomic fluctuations at temperatures above 0 K. In this case, an energy has to be supplied

$$\Delta G = \int_{x_1}^{x_2} (f_r - \tau * bl) dx \qquad (2.1.5)$$

where ΔG is the change in the Gibbs free energy between the two states x_1 and x_2.

On the other hand, when a dislocation oscillates with an attempt frequency χ ($\leq$ an atomic vibration frequency) at a given temperature, it successfully overcomes $\chi \exp(-\Delta G/kT)$ barriers per second. Hence, the dislocation velocity becomes
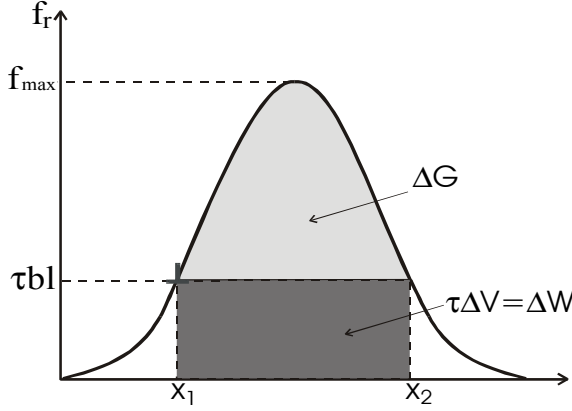
$$v = \kappa \nu \exp\left(-\frac{\Delta G}{kT}\right) \qquad (2.1.6)$$

where κ is the forward distance of the dislocation after a successful activation. Substituting this dislocation velocity into the Orowan equation of the macroscopic plastic strain (2.1.4) yields an Arrhenius rate equation for the plastic strain rate

$$\dot{\varepsilon}_{pl.} = \dot{\varepsilon}_o \exp(-\frac{\Delta G}{kT}) \qquad (2.1.7)$$

Fig. 2.1.2. The resisting force f_r versus distance x for the thermal barriers that oppose dislocation motion

where $\dot{\varepsilon}_o$ is the pre-exponential factor, which is supposed to be constant.

According to [39, 41-43] (for a review, see [40]), the Gibbs free energy of activation (lightly shaded area in the Fig. 2.1.2.) is given by

$$\Delta G = \Delta U - T\Delta S - \tau \Delta V = \Delta U - T\Delta S - \Delta W \qquad (2.1.8)$$

where ΔU is the change of the internal energy, ΔS, the change of the activation entropy, ΔV, the activation volume, and ΔW is the so-called work term (dark shaded area in Fig. 2.1.2) that reflects the work done on the system by the shear stress τ during thermal activation

$$\Delta W = \tau b \Delta x \qquad (2.1.9)$$

with $\Delta x = x_2 - x_1$. Besides, $\Delta U - T\Delta S$ is the Helmholtz free energy

$$\Delta F = \Delta U - T\Delta S \qquad (2.1.10)$$

Consequently, formula (2.1.8) becomes

$$\Delta G = \Delta F - \tau b \Delta x \qquad (2.1.11)$$

The quantity $lb\Delta x$ is the activation volume introduced above

$$\Delta V = lb\Delta x \qquad (2.1.12)$$

The activation volume can be understood as the activation area swept by a dislocation segment of length l over the activation distance Δx multiplied by the Burgers vector of the dislocation. This quantity is also given by the thermodynamical relation

$$\Delta V = -(\frac{\partial \Delta G}{\partial \tau})_T \tag{2.1.13}$$

The activation volume can be determined from macroscopical deformation experiments by logarithmic differentiation of the Arrhenius equation (2.1.7), taking eq. (2.1.13) into account, too

$$\Delta V = kT \left(\frac{\partial \ln \frac{\dot{\varepsilon}}{\dot{\varepsilon}_o}}{\partial \tau} \right)_T \tag{2.1.14}$$

Assuming $\dot{\varepsilon}_o = \text{const}$, this equation can be converted, so that it contains only experimentally measurable quantities [40]

$$V = kT \left(\frac{\Delta \ln \dot{\varepsilon}}{\Delta \sigma} \right)_T \frac{1}{m_s} \tag{2.1.15}$$

where m_s is the orientation factor introduced above. The term in parentheses is the inverse strain rate sensitivity r. It will be described in chapter 2.3.

Logarithmic differentiation of eq. (2.1.7) with respect to the temperature yields the thermodynamical activation enthalpy

$$kT^2 \left(\frac{\partial \ln \frac{\dot{\varepsilon}}{\dot{\varepsilon}_o}}{\partial T} \right)_\tau = \Delta G - T \left(\frac{\partial \Delta G}{\partial T} \right)_{\tau^*} = \Delta H \tag{2.1.16}$$

where $\left(\frac{\partial \Delta G}{\partial T} \right)_\tau = -\Delta S$ is the entropy change mentioned above. Schöck has shown that under the assumption that the main contribution to the activation entropy results from the temperature dependence of the shear modulus μ, the Gibbs free energy of activation can be calculated [39]

$$\Delta G = \frac{\Delta H + \frac{T}{\mu} \frac{d\mu}{dT} m_s \sigma V}{1 - \frac{T}{\mu} \frac{d\mu}{dT}} \tag{2.1.17}$$

This formula contains only measurable quantities, as do the equations (2.1.15) and (2.1.16)

2.2. Dislocation mechanisms controlling plastic deformation of crystals

Fundamentally, the motion of a dislocation is opposed by two different types of barriers: short-range interactions with dislocations that can be overcome by thermal activation described in the chapter 2.1. and long-range interactions due to, for instance, dislocations on parallel slip planes that cannot be surmounted with the help of thermal activation. Thus, the (shear) flow stress comprises two contributions: the thermal component τ^* and the athermal component τ_i (e.g. [38]). Hence,

$$\tau = \tau^* + \tau_i \qquad (2.2.1)$$

The long-range component τ_i leads to a local decrease in the applied stress τ, so that only the component τ^* acts to overcome the short-range obstacles. τ^* is therefore called the effective stress. Dislocation mechanisms governing the plastic deformation of solids will be hereafter considered with respect to their contributions to the thermal and athermal parts of the flow stress.

2.2.1. Thermally activated contribution

Lattice friction (Peierls mechanism)

Because of the periodicity of the crystal structure, a moving dislocation in a crystal experiences a potential energy, or more exactly a free energy, of displacement that varies with the lattice periodicity. This potential energy is called the Peierls potential. The stress necessary for the dislocation to surmount it is named the Peierls stress (for reviews, see [44-48]). In the case of a screw dislocation at 0 K, this stress is given by

$$\tau_{fr.} = \frac{2\mu}{(1-\nu)} \exp(-\frac{2\pi a}{b}) \qquad (2.2.2)$$

where μ is the shear modulus, ν, Poisson's ratio, and a, the interplanar distance between neighboring glide planes. Twice the amplitude of the periodic part of the Peierls potential is called the Peierls energy, and it is related to the Peierls stress by

$$U_{fr.} = \tau_{fr.} ab/\pi \qquad (2.2.3)$$

Consider the influence of temperature on the dislocation movement. At a finite temperature, a dislocation cannot be completely straight, and it does not overcome the Peierls barrier simultaneously all along its line but contains so-called kinks due to thermal fluctuations. Two kinks of opposite sign (a kink pair) place short dislocation segments into the adjacent lattice energy valleys (energy minima), the distance between which equals the distance between two neighboring rows atoms, i.e. the kink height h.
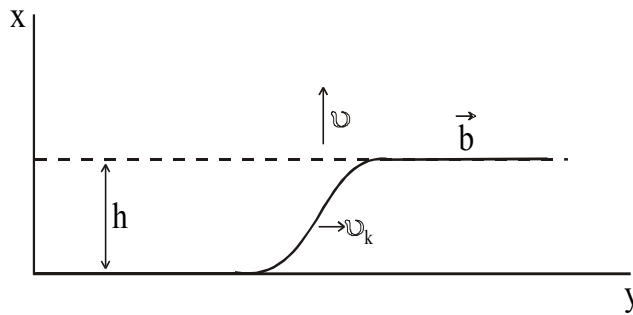

Fig. 2.2.1. A kink moving with a velocity υ_k under an applied stress

Under a small applied stress, the kinks undergo a diffusive drift, thereby bringing about the glide motion of the entire dislocation. Consider a kink in a screw dislocation, and let τ be the shear stress component in the glide plane, acting in the direction of $\vec{b}$ (Fig. 2.2.1.) The velocity of the kink is then

$$\upsilon_k = D_k \frac{\tau b h}{kT} \tag{2.2.4}$$

where D_k is the diffusion coefficient of the kinks. In the limit of small external stress, the concentration of the kinks is almost equal to their thermal equilibrium concentration

$$c_k = \frac{2}{d} \exp\left(-\frac{\Delta F_k}{kT}\right) \tag{2.2.5}$$

where d is the shortest repeat distance along the dislocation line, thus being of the magnitude order of b. All these kinks have a drift velocity given by the equation (2.2.4), with the positive and negative kinks drifting in opposite directions. The net velocity of the dislocation normal to itself is then

$$\upsilon = h c_k \upsilon_k \tag{2.2.6}$$

Combining the three equations (2.2.4) to (2.2.5) yields the dislocation velocity

$$\upsilon = \frac{2\tau b h^2}{d\,kT} D_k \exp\left(-\frac{\Delta F_k}{kT}\right) \tag{2.2.7}$$

It can be shown that this relation is valid in a broad range of stresses [44]. The kink formation energy can be expressed by the Peierls energy

$$\Delta F_k = (2h/\pi)\sqrt{(2U_{fr.}\Gamma)} \tag{2.2.8}$$

where Γ is the line tension.

Chemical hardening: solution and precipitation hardening

Solution hardening is defined as an increase of the flow stress of a crystal containing non-diffusing foreign atoms dissolved in its lattice owing to interactions between the atoms, so-called solute atoms, and dislocations in the crystal. The dislocations are hindered by these interactions. At zero temperature, their movement is possible only if the applied shear stress is higher than a critical shear stress τ_c [49, 50]. At the critical stress, the force a dislocation exerts on the obstacles τ_c bl is just high enough to overcome the interaction force of the obstacles. In addition to electrical interactions in ionic crystals and semiconductors, the origin of the local interaction forces f_{int} may be due to the paraelastic interaction on account of a size misfit between the solute atoms and the matrix as well as due to the dielastic interaction because of a modulus misfit between them. There may also be interactions owing to a possible non-spherical symmetry of the stress fields of the point defects.

Real crystalline solids frequently contain a certain amount of precipitates, that is extrinsic particles. Dislocation interaction with these defects causes the so-called precipitation hardening. Two different cases of such interactions may occur. The particles may be either impenetrable or penetrable for dislocations [51]. In the former case, a dislocation is forced by the applied stress to bow around the particle and by-pass it. The by-passing dislocation leaves a loop around the particle. This mechanism was suggested by Orowan and is therefore called the Orowan mechanism. In the latter case, the particle is sheared by the dislocation as the latter moves through the crystal. This can only occur if the interface between the particle and the matrix is coherent. The coherent interface does not show any geometric discontinuity in the atomic arrangement.

Both the Orowan and the cutting mechanisms can be discussed in terms of the interaction of a single dislocation with a linear array of particles of diameter D and a

center to center distance l between them. This discussion leads to an expression for the critical resolved shear stress needed for the dislocation to overcome a row of equidistant obstacles in the slip plane as shown in Fig. 2.2.2. The dislocation line is pressed against the row by the applied stress and bends between the particles with a bending angle ψ.
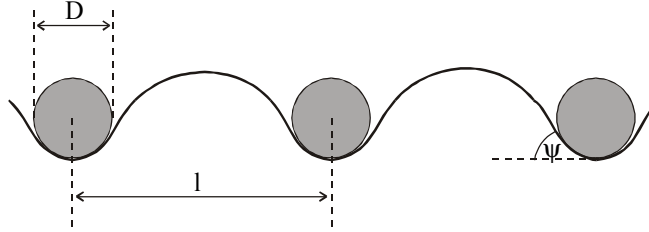

Fig. 2.2.2. Interaction of a
dislocation with a row of obstacles

The angle ψ depends on inter-particle distance l, their diameter D, the increase in the applied shear stress $\Delta\tau$ due to the interaction with the particles, the magnitude of the Burgers vector b, and the line tension Γ according to the equation

$$\Delta\tau b(l - D) = 2\Gamma\sin\psi \qquad\qquad (2.2.9)$$

The right part of this equation describes the pinning force exerted by each particle on the dislocation

$$f_{pin} = 2\Gamma\sin\psi \qquad\qquad (2.2.10)$$

Depending on the origin of the interaction between the particle and the dislocation, there exists a maximum force f_m, which the particle can sustain. Its value depends on the distance of the slip plane with respect to the particle center. If this maximum force is reached before the bending angle becomes 90°C, the particle will be cut by the dislocation. However, in the case that the bending angle becomes 90°C before f_m is reached, the dislocation by-passes the particle by the Orowan mechanism. Assuming this is the beginning of plastic deformation at 0 K, the following equations indicate the increase in CRSS, $\Delta\tau_o$:

Cutting mechanism $\Delta\tau_o = f_m /(b(l - D))$ for $f_m < 2\Gamma$ $\qquad\qquad$ (2.2.11)

Orowan mechanism $\Delta\tau_o = 2\Gamma /(b(l - D))$ for $f_m \geq 2\Gamma$ $\qquad\qquad$ (2.2.12)

If the precipitates are small, they can be treated similarly to the solute atoms. In this case, the obstacles interact with the dislocations only along a short part of their total length. The obstacles can then be called localized obstacles or point obstacles (D=0) in eq. (2.2.11). Up to this point in our approach, the obstacles were considered to be arranged in a regular array. In practice, they are distributed irregularly, which can be treated in many cases by a random arrangement, as shown in the Fig. 2.2.3. In this case, the average obstacle spacing becomes dependent on the stress, and eq. (2.2.11) thus reads

$$f_m = \tau_c \, b l(\tau_c) \qquad (2.2.13)$$

The statistical problem was treated for the first time by Friedel [52]. The average spacing between obstacles is

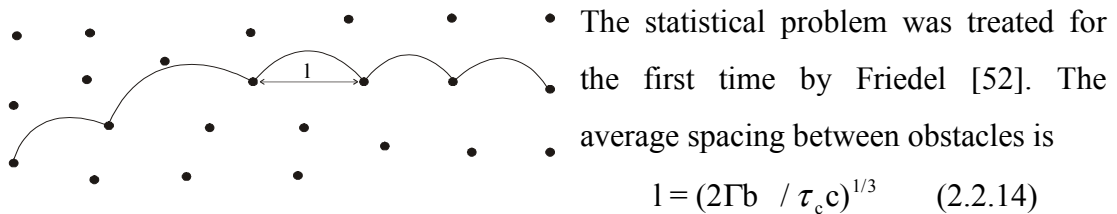$$l = (2\Gamma b \ / \ \tau_c c)^{1/3} \qquad (2.2.14)$$

Fig. 2.2.3. Dislocation in a field of point obstacles

where c is the atomic fraction of foreign atoms. Combining the last two equations yields

$$\tau_c = f_m^{3/2} c^{1/2} \ / \ b^2 (2\Gamma)^{1/2} \qquad (2.2.15)$$

This formula describes the contribution of a random array of localized obstacles to the flow stress at zero temperature. At finite temperatures, this theory has to be combined with the theory of thermal activation, described in chapter 2.1.2. The Orowan process is always of athermal nature.

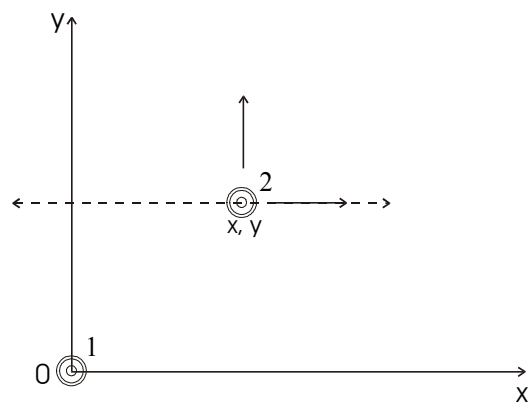## 2.2.2. Athermal contribution to the flow stress

Consider two screw dislocations 1 and 2 lying parallel to the z axis (Fig. 2.2.4.) [38, 53]. Assume that y is constant. The interaction force per length between the two screw dislocations with respect to the motion in x direction is

$$f_x = \frac{\mu b^2}{2\pi} \frac{x}{x^2 + y^2} \qquad (2.2.16)$$

Fig. 2.2.4. Interaction between two screw dislocations

The maximum interaction force is obtained

by differentiation of this equation with respect to the coordinate x of dislocation motion with subsequently equating the result to zero, which yields

$$\frac{\partial f_x}{\partial x} = \frac{\mu b^2}{2\pi} \frac{y^2 - x^2}{(x^2 + y^2)^2} = 0 \qquad (2.2.17)$$

and hence

$$f_{x_{max}} = \pm \frac{\mu b^2}{4\pi y} \qquad (2.2.18)$$

According to Taylor's theory, the critical shear stress to move one dislocation in the array of other parallel dislocations can be identified as the stress required to force two dislocations lying on parallel slip planes of a minimum spacing y past each other against their elastic interaction just defined. Hence,

$$\tau_p = \frac{\mu b}{4\pi y} \qquad (2.2.19)$$

Should the stress exceed the interaction force between the two dislocations, they can pass against each other. The minimum slip plane distance is considered to be some fraction of the average mutual dislocation distance. In an array of parallel dislocations of a density ρ, the average distance is $\approx \rho^{-1/2}$, so that the contribution of the interaction between parallel dislocations to the flow stress can be rewritten as

$$\tau_p = \alpha \frac{\mu b}{2\pi} \rho^{1/2} \qquad (2.2.20)$$

where $\alpha / 2\pi$ is a numerical constant of about 0.5.

2.2.3. Work-hardening and recovery

During deformation, the dislocation density increases, giving rise to an increase in the athermal component of the flow stress, in accordance with eq. (2.2.20). The increase of the flow stress is called work-hardening. Recovery is a thermal diffusional rearrangement of crystal defects where internal strains present in a crystal are relieved. Such a rearrangement may result in dislocation migration and annihilation leading to energetically favorable dislocation arrays like subgrain boundaries, with the subsequent growth of the subgrains [54, 55]. This phenomenon is named polygonization. When it takes place, the flow stress of a crystal decreases, and the latter becomes more ductile. Apart from the poligonization, the decrease of the flow

stress is also associated with mutual annihilation of dislocations (e.g. [36]). There are several recovery controlled creep models of crystals known up to date, and we will briefly consider the most essential points of these. Firstly, we assume that the applied stress of creep is a function of time and strain [56]

$$d\sigma = \left(\frac{\partial \sigma}{\partial t}\right)_\varepsilon dt + \left(\frac{\partial \sigma}{\partial \varepsilon}\right)_t d\varepsilon = -Y_{rec} dt + \Theta d\varepsilon \qquad (2.2.21)$$

where Y_{rec} and Θ are defined as the recovery rate and the work-hardening rate, respectively (Fig. 2.2.5.). During creep at constant stress, the last formula turns into the Bailey-Orowan equation. Consequently, the steady state strain rate can be expressed

$$\dot{\varepsilon}_{st} = -\frac{(\partial \sigma / \partial t)_\varepsilon}{(\partial \sigma / \partial \varepsilon)_t} \qquad (2.2.22)$$

$$Y_{rec} = \left(\frac{\Delta\sigma}{\Delta t}\right)_{\Delta\sigma \to 0} \qquad \Theta = \left(\frac{\Delta\sigma}{\Delta\varepsilon}\right)_{\Delta\sigma \to 0}$$
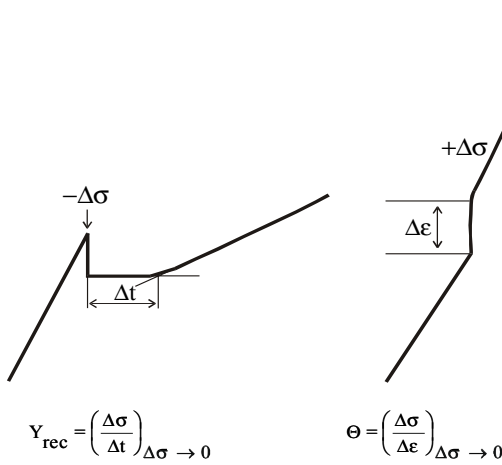
Fig. 2.2.5. Schematic display for estimating recovery and work-hardening rates

and it is reduced to

$$\dot{\varepsilon}_{st} = \frac{Y_{rec}}{\Theta} \qquad (2.2.23)$$

2.3. Macroscopic compression experiments

The previous chapters show that the flow stress measured during a deformation experiment depends on the temperature and the strain rate applied owing to the thermal part of the flow stress. Furthermore, the deformation behavior is a function of the crystal orientation in accordance with Schmid's law. Since the microstructure of the sample is changed during the deformation as a result of dislocation production and annihilation, the deformation behavior depends also on the degree of the sample deformation. Therefore, the crystal microstructure should be considered a function of the strain [57, 58].

2.3.1. The stress-strain curve

One of the macroscopic methods to study plastic deformation consists in compression tests along a defined deformation axis. The material is deformed at a constant strain
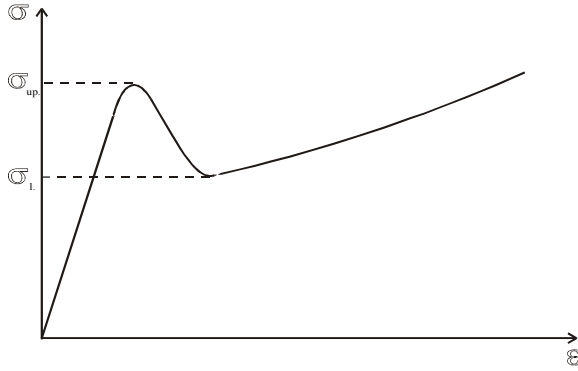
Fig. 2.3.1. Schematic representation of the yield point effect. $\sigma_{up.}$ and $\sigma_{l.}$ are the upper and lower yield stresses, respectively

rate and temperature, and the stress-strain or deformation curve, i.e. a plot of the stress applied to the sample versus its strain, is measured (e.g. [59]). It can have several different regions, two of them being the yield point and work-hardening ranges, as shown in Fig. 2.3.1. The former constitutes a phenomenon where after the stress reaches a maximum (the "upper yield point"), a finite amount of plastic deformation occurs at decreasing stress, so that the flow stress drops to the level of the "lower yield stress", after which the plastic deformation can occur without adding to the stress. This interval is called the steady state. After that, work-hardening starts taking place, that is the flow stress increases constantly as the strain rises. The work-hardening may be of various origins [36]. Mainly, the increase of the flow stress is a consequence of the increasing dislocation density. This can be due to the mutual interaction between dislocations moving on parallel slip planes, as was described by eq. (2.2.20) of chapter 2.2.2. Besides, dislocations moving on non-parallel slip planes intersect each other. Hence, the produced elastic interactions give rise to the flow stress, with the latter depending on the dislocation density in a similar way as eq. (2.2.20) says. In addition, dislocation intersections result in the formation of jogs, the motion of which contributes to the flow stress, too. The work-hardening coefficient is inferred from eq. (2.2.21), and according to [60], becomes

$$\Theta = \frac{\partial \sigma}{\partial \varepsilon}\bigg|_{\dot{\varepsilon}, \, T} \tag{2.3.1}$$

The total strain during a compression experiment consists of elastic and plastic parts

$$\varepsilon = \varepsilon_{el.} + \varepsilon_{pl.} = \sigma / E + \varepsilon_{pl.} \tag{2.3.2}$$

where $\varepsilon_{el.}$ is a function of compressive stress according to Hooke's law. E is Young's modulus. As a result, the total strain rate $\dot{\varepsilon}$ contains elastic and plastic parts

$$\dot{\varepsilon} = \dot{\varepsilon}_{pl.} + \dot{\sigma} / E \tag{2.3.3}$$

2.3.   Macroscopic compression experiments

By means of special tests within the macroscopic deformation experiments, one can identify the parameters of thermal activation described in chapter 2.1.2. Their numerical values allow one to conclude on the mechanisms controlling the plastic deformation, which were discussed in chapter 2.2.

2.3.2. The strain rate sensitivity

The dependence of the flow stress on the plastic strain rate can be expressed using the so-called strain rate sensitivity:

$$r = \frac{\partial \sigma}{\partial \ln \dot{\varepsilon}_{pl.}} \qquad (2.3.4)$$

or the stress exponent

$$m^* = \frac{\partial \ln \dot{\varepsilon}}{\partial \ln \sigma} \qquad (2.3.5)$$

The strain rate sensitivity can be measured by a strain rate cycling experiment. It consists in an instantaneous change of the strain rate $\dot{\varepsilon}$ of the compression experiment, so that one can identify the resulting stress increment $\Delta\sigma$ and hence r according to eq. (2.3.4)

Another way to obtain the strain rate sensitivity is to do stress relaxation tests. These are a sudden stop of the loading process where the sample continues to deform at a diminishing strain-rate and under the action of a decreasing stress, while the total strain remains constant [61, 62]. Therefore, the plastic part of the strain rate becomes proportional to the negative stress rate according to equation (2.3.3)

$$\dot{\varepsilon}_{pl} = -\dot{\sigma}/E \qquad (2.3.6.)$$

If one plots the logarithm of the negative stress rate versus the decreasing stress, one obtains the so-called relaxation curve of the test, the inverse slope of which is the strain rate sensitivity r.

2.3.3. The temperature sensitivity

The temperature sensitivity of the flow stress $-\dfrac{\Delta\sigma}{\Delta T}$ is measured by means of temperature cycling tests. During such a test, the sample is unloaded, the specimen temperature is increased or decreased, and the sample is reloaded. Hence, an

increment of the flow stress $\Delta\sigma$ appears. Using eq. (2.1.16) and keeping in mind that

$$\frac{\partial \ln\dot{\varepsilon}/\dot{\varepsilon}_o}{\partial T}\bigg|_{\tau} = -\frac{\partial \ln\dot{\varepsilon}/\dot{\varepsilon}_o}{\partial \tau}\bigg|_{T} * \frac{\partial \tau}{\partial T}\bigg|_{\dot{\varepsilon}}$$ [53], the activation enthalpy can be calculated

$$\Delta H = - kT_1 T_2 \left(\frac{\Delta\sigma}{\Delta T}\right)\left(\frac{2}{r_1 + r_2}\right) \tag{2.3.7}$$

where k is the Boltzman constant, T_1 and T_2 are temperatures before and after the change takes place, and r_1 and r_2 are the strain rate sensitivities before and after the cycle. This equation deals with the proper averages of the temperatures and strain rate sensitivities before and after the temperature change.

3. Cubic zirconia single crystals

3.1. Structure and phase relationship of cubic zirconium dioxide

Pure zirconia (ZrO_2) undergoes two crystallographic transformations between room temperature and its melting point: monoclinic to tetragonal at $\approx 1170°C$ and tetragonal to cubic at $\approx 2370°C$. The volume changes associated with these transformations are sufficiently large, so that thermal deviations through the transformations tend to shatter objects made of pure zirconia. The high-temperature tetragonal and cubic forms can be stabilized with a variety of oxide additions, one of which is yttria (Y_2O_3) [28, 29, 63]. The relevant phase diagram is shown in Fig. 3.1.1. According to it, cubic zirconium dioxide exists down to room temperatures when the concentration

Fig. 3.1.1 Phase diagram of the ZrO_2-Y_2O_3 system [64]

of yttria is higher than 8mol%. When investigated, cubic zirconia is mostly stabilized with 10mol% Y_2O_3, so as to make sure that the tetragonal phase does not affect the data on the cubic phase.

Cubic zirconia has the ideal calcium fluorite (CF_2) structure [65, 66, 22]. Its lattice parameter is 0.517 nm. The zirconium atoms are situated in an fcc lattice, i.e. at the corners of the cubic elementary cell as well as at the halves of the $\langle 110 \rangle$ directions. Oxygen atoms lie at the quarters of $\langle 111 \rangle$ directions (Fig. 3.1.2.).

Zirconium

Oxygen

Fig. 3.1.2. Ideal cubic zirconia elementary cell

17

3.1.   Structure and phase relationship of cubic zirconium dioxide

The space group of the structure had been believed to be $Fm\overline{3}m$ until this was proved not to be the case. According to neutron and X-ray scattering analysis [67] and to convergent beam electron diffraction [63], it was revealed that oxygen atoms are displaced from their ideal position by up to 0.05 nm along the $\langle 100 \rangle$ or $\langle 111 \rangle$ axes, and the space group $P\overline{4}3m$ was identified.

The cations of oxides stabilizing the cubic form of zirconia down to room temperature are of lower valance than Zr. To maintain charge neutrality, either cation interstitials or anion vacancies must form. In zirconia alloys, anion vacancies are generated. These are thought to be largely responsible for the stabilization of the cubic phase. There is also substantial evidence that the stabilizing cations are incorporated by substituting zirconium.

The precise mechanism of stabilization of cubic zirconia with Y_2O_3 is not clear so far. According, e.g., to [66], compensating anion oxygen vacancies must appear in the system ZrO_2-Y_2O_3, in order to maintain the charge balance of the composition because zirconium valence is higher than that of yttrium. The compensating oxygen vacancies are in some way spaced in the ZrO_2-Y_2O_3 lattice, as are Y solute cations

Model 1: Y-Vo-Y   Model 2: Y-Vo-Zr   Model 3: Zr-Vo-Zr
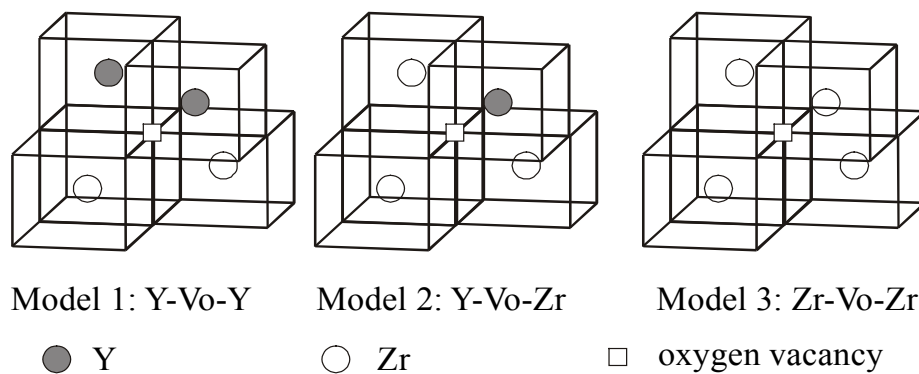
⬤ Y   ◯ Zr   ☐ oxygen vacancy

Fig. 3.1.3. Schematic illustration of three models for cation-oxygen vacancy association in cubic zirconia stabilized with yttrium oxide [68]

[68]. Besides, each charge-compensating oxygen vacancy is generated by every two substitutional Y atoms. There are three possibilities for the position of this vacancy (Fig. 3.1.3.). Further, it was postulated in the same paper that the model 3 was most consistent, i.e. no Y ion is in a nearest neighbor position of the oxygen vacancy.

Hence, it is inferred that the distance between yttrium and oxygen ions must remain constant (Y maintains eightfold coordination), and this was in turn calculated to 0.233 nm. However, the mechanism whereby the oxygen vacancies retain cubic zirconia at room temperatures remains a point to clarify.

Elastic constants of single crystals of yttria-stabilized zirconia
That one can study dislocation mechanisms controlling the flow stress of a crystalline material, one has to be familiar with its elastic constants. In the case of cubic
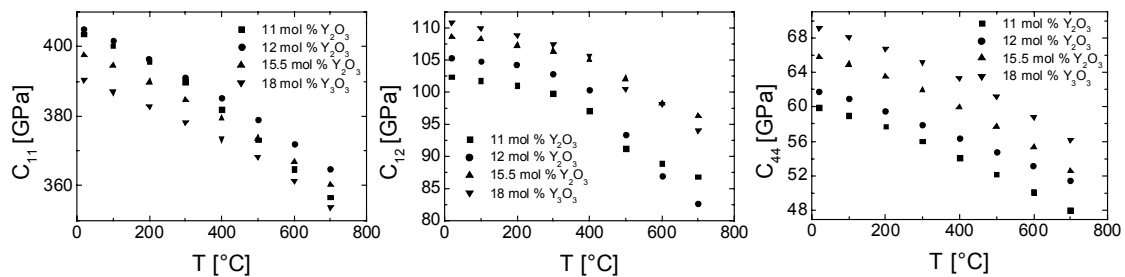
Fig. 3.1.4. Elastic constants of cubic zirconia single crystals at different yttria concentrations and temperatures up to 700°C [28]

zirconium dioxide, only three elastic constants C_{11}, C_{12} as well as C_{44} have to be introduced. There are a number of papers on the elastic constants of cubic zirconia with respect to the yttria concentration and temperature [28, 69-71]. Temperature dependencies of the constants are shown in Fig. 3.1.4. One can conclude from the figure that the elastic constants decrease with increasing temperature. Unlike this, the effect of yttria dopant concentration is somewhat more complicated since an increase
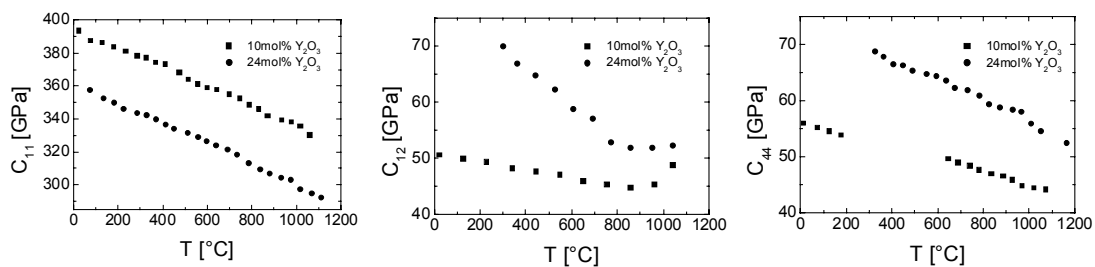
Fig. 3.1.5. Elastic constants of c-ZrO$_2$ at two concentrations of yttria and different temperatures [71]

of the latter adds to C_{12} and C_{44} but diminishes C_{11}, the explanation of which was given in the framework of a shell model and forces of interaction in fluorite structures.

The figure 3.1.5. features other data on the elastic constants of cubic zirconia, measured by Brillouin scattering experiments. The dependencies are similar to those shown above both qualitatively and quantitatively.

Point defect structure of cubic zirconia

The properties of point defects influence the plastic deformation in many ways. At high temperatures, dislocation climb is controlled by diffusion. Besides, the motion of dislocations may be impeded by point defect segregation or by reorientation of defect clusters in the stress field of the dislocations (e.g. [44]). That the incorporation of two yttrium ions into the cubic zirconia lattice is accompanied with the formation of an anion vacancy in order to preserve electrical neutrality, as well as the fact that such vacancies are not arranged randomly, was already described in the subchapter 3.1 of this doctoral thesis. It is also known there is a strong tendency for such vacancies to cluster in pairs as well as a weaker tendency for the clusters to form even larger aggregates having $Zr_3Y_4O_{12}$ as the structural unit [34].

Oxygen vacancies and substitutional yttrium atoms tend to form dipoles. This tendency was shown by [35, 31, 32] using mechanical loss (internal friction) experiments. In turn, it leads to an atomic model of the cubic fluorite cell where oxygen ions corresponding to 8-fold coordination are situated around the site of a Zr^{4+} ion which is occupied by a substitutional dopant ion (Y^{3+}). The oxygen vacancy may be positioned at one of eight nearest neighbor sites around the dopant ion with $\langle 111 \rangle$ orientation of the dipole axis in each case. The mobility of the vacancies decreases with increasing yttria content, whereas the diffusivity of Zr via oxygen vacancies increases with rising concentration of Y_2O_3.

3.2. Dislocation plasticity in cubic zirconia single crystals

3.2.1. Glide planes, Burgers vectors, and slip geometry of c-ZrO$_2$

Basically, the main slip system of the calcium fluorite structure is of the type $\{001\}1/2\langle 110 \rangle$. It was observed in [72] together with the secondary slip system

{110}1/2⟨110⟩, although the secondary slip was reported to occur on {001}1/2⟨110⟩, too. That dislocations can also glide on {111} planes was postulated in [73] for UO$_2$ whose structure is similar to that of ZrO$_2$. In all the cases, the Burgers vector is 1/2⟨110⟩ (see [74]).

More or less the same situation has been observed in cubic zirconium dioxide by several investigators. Initially, the glide system {001}1/2⟨110⟩ was observed in [27, 10], the so-called easy slip system. The compression axis was ⟨112⟩. This axis is called a soft orientation because it activates single slip on the system with the cube plane whose orientation factor is 0.47 (the highest possible at this deformation axis in cubic zirconia). In [11-13] and later in [23], the {001}1/2⟨110⟩ primary slip system was postulated; the experiments have been mostly performed at 1400°C. Apart from compression experiments at a constant strain rate, a few sets of indentation tests with yttria-stabilized cubic zirconia have been carried out by [24, 25, 65] at temperatures up to 1000°C. Repeatedly, these indicated {001}1/2⟨110⟩ slip.
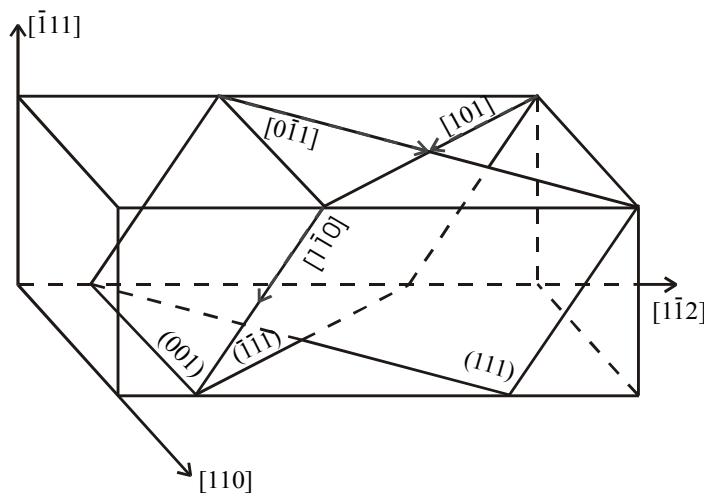
Fig. 3.2.1. Slip systems of cubic zirconia single crystals deformed along ⟨112⟩ axis [11]

Some of the above-stated papers have also dealt with secondary slip planes possible in c-ZrO$_2$ deformed along the [1$\bar{1}$2] compression direction, which appeared to be of the {111} type, specifically (111)1/2[0$\bar{1}$1] and ($\bar{1}\bar{1}$1)1/2[101] with the orientation factors of 0.41. These are shown in figure 3.2.1 together with the primary slip plane.

In recent years, many sets of compression experiments along the [112] axis on cubic zirconia doped with yttria have been carried out in a broad range of lower temperatures; their results are found elsewhere [4, 18-21]. According to the post-

mortem optical and transmission electron microscopy analyses, the {001} slip plane has been unambiguously confirmed the primary slip plane with the Burgers vector $1/2\langle 110\rangle$. As far as secondary slip systems are concerned, these have been identified as (010) and (100), their Burgers vector directions being [101] and $[0\overline{1}1]$. This result is rather unusual since the orientation factor of the secondary cube planes is 0.35 at the $\langle 112\rangle$ axis, whereas that of {111} planes is 0.41, and CRSS of the secondary cube planes was concluded to be actually the same as that of {111} planes [14].

In the case of the deformation along the $\langle 100\rangle$ compression direction, one cannot but admit a serious lack of experimental data. The compression axis is chosen in order to suppress the easy glide on the cube planes and activate other glide systems. In [10], the duplex $\{111\}1/2\langle 1\overline{1}0\rangle$ slip was revealed at 1300°C, which was later confirmed by [78], the experimental temperatures having been not higher than 500°C, as well as in [14] at 1400°C. The orientation factor of the slip system is 0.41. That the $\{111\}1/2\langle 110\rangle$ slip systems are
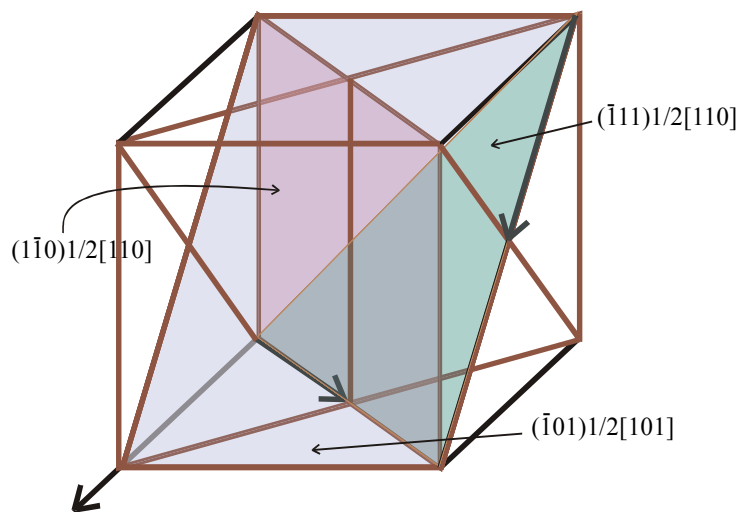
Fig. 3.2.2. Slip systems of cubic zirconia single crystals deformed along $\langle 100\rangle$ axis

engaged during the deformation along the $\langle 100\rangle$ axis was questioned in [16], and four equivalent $\{110\}1/2\langle 110\rangle$ systems with the orientation factor 0.5 were believed to be activated instead, which was somewhat later confirmed in [4, 19]. These investigators did not, however, go lower than 1150°C. All the slip systems possible in cubic zirconia single crystals deformed in $\langle 100\rangle$ compression direction are exhibited in the Fig. 3.2.2 as a summary of the above-described studies.

3.2.2. Compression experiments at a constant strain rate

Macroscopic compression experiments on cubic zirconia single crystals have a long historical tradition that spans more than a dozen years. We will briefly analyze some

of these results, whereas a comprehensive review can be found in [17]. The first attempt to study plastic deformation of ZrO_2 fully stabilized with Y_2O_3 was made in [27], where the deformation of the material was investigated along the $\langle 112 \rangle$ compression axis at 1400°C at a strain rate of $1.3*10^{-5}$ s^{-1}. All the studied samples exhibited apparent well-defined upper and lower yield points followed by a transitional region leading to flow with zero work hardening, which proved to be similar to the dependence observed in [30], where plastic deformation of calcia stabilized cubic zirconia was analyzed. The flow stress increased with increasing yttria content whose maximum value was 18.0 mol%. In [10], fully stabilized zirconia single crystals were studied at 1400°C with the same strain rate as in [27] along three different compression axes: $\langle 100 \rangle$, $\langle 111 \rangle$, and $\langle 112 \rangle$. The stress-strain curves of the $\langle 111 \rangle$ and $\langle 112 \rangle$ crystals showed the yield point effect and modest work hardening thereafter, whereas those of the $\langle 100 \rangle$ samples did not exhibit any yield point effect at all, yet a considerable work hardening region occurred, which was accounted for the difference between single and duplex slip of the deformation in $\langle 112 \rangle$ or $\langle 111 \rangle$ and $\langle 100 \rangle$, respectively, according to the opinion of the investigators. In [12-14], plastic deformation of cubic zirconia was studied in the $\langle 112 \rangle$ axis in the temperature range from 1200°C up to 1500°C. The relevant stress-strain curves did not show the yield point effect at 1200-1300°C, which was explained by an increased work hardening rate and decreased recovery rate with decreasing temperature.

The dependence of the flow stress of cubic zirconia single crystals on the yttria concentration was investigated in [23] by compression tests at 1400°C. When the dopant concentration was up to 18mol%, the stress-strain curves exhibited the yield point. Unlike it, the stress-strain curves of the crystals stabilized with a higher yttria content did not show the yield drop, but were serrated, which was understood by the formation of Lüders bands in these samples. The maximum of the flow stress was observed with the sample doped with 21mol% yttria, which was subsequently proved in [16, 26].

A study of plastic deformation of fully stabilized zirconia doped with three different concentrations of yttria (10, 12.5, and 15mol%) has been carried out by [15]. The

investigators made three sets of compression experiments along $\langle 112 \rangle$ from 250°C up to 550°C under confining hydrostatic pressure lest the samples have broken before the plastic deformation began. The basic strain rate was chosen $2*10^{-4}$ s^{-1}. It was found in the framework of the research that the flow stress of cubic zirconia single crystals increased with increasing yttria content up to a maximum at 15mol%, and it is with that concentration that the yield point effect was observed at 450°C, being absent in all the other cases, whereas work hardening was registered during most of the experiments. As to the compression experiments along the $\langle 100 \rangle$ axis, these were performed on ZrO_2-10mol%Y_2O_3 single crystals from 350°C up to 500°C with the same basic strain rate as in the case of the soft mode. The apparent stress-strain curves showed the yield point effect at all temperatures barring 400°C, the flow stress of the curves being higher than that obtained on ZrO_2-10mol%Y_2O_3 during the deformation along $\langle 112 \rangle$ at the respective temperatures, which might be because the $\langle 112 \rangle$ compression samples had mostly broken before any essential portion of plastic deformation could be attained.

Over the recent ten years, several series of macroscopic compression experiments on cubic zirconia have also been performed, most fundamental of these being [4, 17-22] carried out in the plasticity group in the MPI of Microstructure Physics in Halle. They studied the plastic deformation of ZrO_2-10mol%Y_2O_3 single crystals along the $\langle 112 \rangle$ compression axis in the temperature range from 500°C, for it was the lowest possible experimental temperature, up to 1400°C at the basic strain rate 10^{-6} s^{-1}, although several additional tests were made at 10^{-4} s^{-1} at 1400°C. All the experiments were carried out in air environment. According to the results of the research, the flow stress of

Fig. 3.2.3. Stress-strain curves of ZrO_2-10mol%Y_2O_3 in $\langle 112 \rangle$ [4]

the cubic zirconia decreases gradually with increasing experimental temperature, as shown in the Fig. 3.2.3. Similarly to the previous research, the yield drop occurs at 1400°C but disappears from 1200°C down to 700°C, the relevant stress-strain curves exhibiting work-hardening instead.

Below 600°C, the yield drop starts to take place again. Within the performed compression experiments, SRC and SR tests were made. The results of these were used to calculate the strain rate sensitivity of the flow stress. The flow stress is very sensitive to the strain rate near 1400°C and down from 600°C, the interval from 800°C up to 1200°C being the least sensitive to the experimental strain rate. The temperature dependence of the strain rate sensitivity below 1250°C is presented in Fig. 3.2.4. It shows that
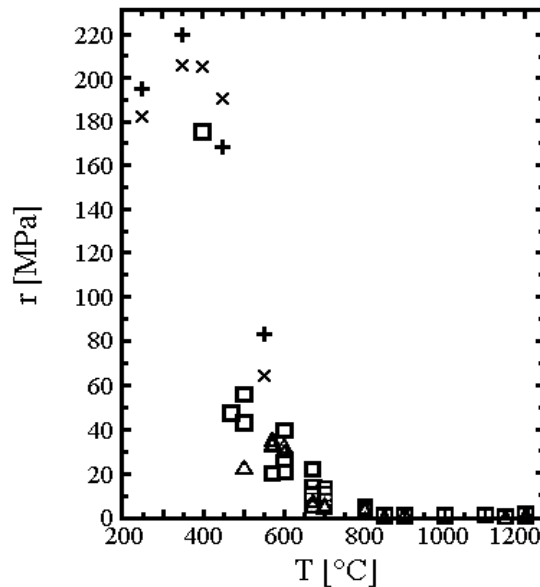
Fig. 3.2.4. Temperature dependence of the strain rate sensitivity of ZrO_2-10mol%Y_2O_3 in $\langle 112 \rangle$ [4]

the strain rate sensitivity decreases constantly with increasing temperature, being less than 10 MPa from about 800°C up to 1200°C.

The same group of researchers studied plastic deformation of cubic zirconia single crystals in the $\langle 100 \rangle$ compression direction, too, but one cannot help admitting a lack of relevant experimental data. The experiments were carried out at 1400°C with the basic strain rates 10^{-4} s^{-1} and 10^{-6} s^{-1}, and another test was made at 1150°C at 10^{-6} s^{-1}. The stress-strain curves show the yield point effect at 1400°C with both strain rates, but it does not appear in the 1150°C compression experiment.

Apart from the compression experiments, high-temperature creep behavior of yttria stabilized zirconia single crystals as well as the influence of the yttria concentration on this behavior have been investigated [75-77]. The concentration of yttria was from 9.4 up to 21mol%, and the entire range of the experimental temperatures lay between

1300°C and 1800°C. The creep behavior was explained in terms of a transition between glide and climb controlled creep. As regards the yttria concentration dependence of the creep rate in that the latter increased with decreasing yttria content, it was accounted for by assuming a strong dependence of cation diffusion on the concentration of yttria. The decrease of the creep rate at constant stress with increasing yttria concentration is explained by a strong dependence of the cation diffusion coefficient on the latter.

3.2.3. Dislocation microstructure of cubic zirconia
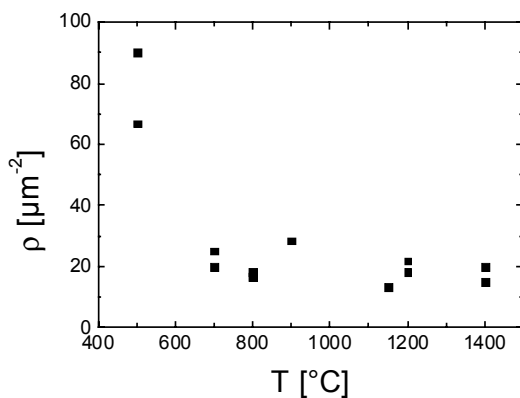
Fig. 3.2.5. Dislocation density in the $\{001\}1/2\langle110\rangle$ slip system versus temperature [4]

Transmission electron microscopy analysis of ZrO_2 single crystals stabilized with yttria followed the deformation experiments described in the previous subchapter. We will briefly announce some of the most essential results of these. In [21], the dislocation microstructures of 10mol% cubic zirconia single crystals deformed at 700°C - 1150°C in the $\langle112\rangle$ compression direction were investigated (further 700°C-sample, 800°C-sample, etc.). The dislocations were found to be concentrated in localized bands that were separated by dislocation-free regions of a width in the order of 10 μm. The dislocation density inside the bands was $2*10^{13}$ m^{-2}. Most of the dislocations were identified to be of screw character. Besides, dipoles of the screw dislocations were detected. Quite the same picture was observed by [20], although edge dislocations, loops, and debris were found, too. The screw dislocations were jogged and bowed out between pinning points, while the edge dislocations were rather smooth. At temperatures of 870°C and 1150°C, single crystals of cubic zirconia doped with 10mol% yttria were studied by in situ straining with the $\langle112\rangle$ tensile axis inside a high-voltage electron microscope [18, 90]. Unlike the above-mentioned investigations, at 1150°C, dislocations or half-loops of distinctive edge character were observed, rarely screw dislocations, and so-called alpha-shaped dislocation configurations. These alpha-shaped configurations

consisted of a straight screw segment and a more or less bowed edge one. These configurations are intermediate stages of dislocation multiplication. In addition, a high number of dislocation loops occurred. It was also reported that the dislocations were created instantaneously in a region larger than the area under observation of about 15 μm in diameter. The dislocations moved very jerkily at jump distances usually larger than the viewing area. One in situ experiment was started at 1150°C, after which the temperature was reduced down to 870°C, so as to compare both microstructures. At 870°C the dislocation loops were much smaller and the screw dislocations were curly-shaped. The glide behavior was similar to that observed at 1150°C. The dislocations moved very jerkily, too, but their jump distances were shorter. These were measured as 0.3 μm.

In [78], the dislocation microstructure of cubic zirconia single crystals deformed at 250°C - 550°C in compression was studied by TEM. Long screw dislocation segments with numerous pinning points and dislocation loops were observed. At 250°C, the loops were elongated in the screw orientation leaving behind screw dipoles. Long dipolar loops of screw character resulted from a local recombination of these dipoles. At 550°C, the edge components of the loops were longer than at 250°C, but the screw segments still dominated. That dislocations of screw character were hindered by pinning points at temperature lower than 900°C was also registered by [4, 17, 21]. At 500°C, dislocation density was so high that the individual dislocations could not be discerned. A temperature dependence of dislocation density is presented in the Fig. 3.2.5. In the same temperature range, pairs of dislocations were detected. These lay practically on neighbouring slip planes, and their Burgers vectors were anti-parallel. Such dislocation pairs could appear due to mutual impeding of the two constituent separate dislocations as they glided beside one another. Sometimes, one of the two could overcome the mutual attraction, so that it moved over some distance. Finally, it reached out another dislocation and became hindered again.

In [27], the dislocation microstructure of a 9.4mol% cubic zirconia single crystal deformed at 1400°C in the ⟨112⟩ compression was studied, and many curved dislocations together with small dislocation loops were observed. Also, various

dislocation reactions were believed to occur. In [10], the dislocation network of a 1200°C sample was compared with that of a 1400°C. In both cases, dislocation loops were observed, but the dislocation density of the 1400°C sample was lower than that of the 1200°C, which was somewhat later confirmed with the results of [13]. Similar loops as well as dislocation dipoles were determined by [12] where 1400°C samples were investigated at different levels of deformation. The dipoles were guessed to form by pinning of screw dislocations by solute or impurity atoms. In turn, the loops formed out of the dipoles by climb and/or cross-slip. Besides, a number of dislocation nodes was observed, particularly at high deformation level. These were guessed to originate from the intersection of primary and secondary slip planes in cubic zirconia single crystals according to the following dislocation reaction:

$$\frac{1}{2}[1\overline{1}0]+\frac{1}{2}[\overline{1}0\overline{1}]\rightarrow\frac{1}{2}[0\overline{1}\,\overline{1}]$$
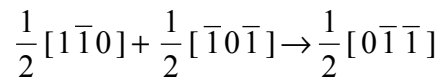
The formation of nodes and dislocation loops were also detected by [77, 79] where high-temperature creep of cubic zirconia was studied from 1300°C up to 1600°C. Cross slip was reported to occur, too.

3.2.4. Microprocesses of plastic deformation of cubic zirconia single crystals.

Typical dislocation models (lattice friction, athermal interaction between parallel dislocations, thermal recovery, to name but a few) controlling plastic deformation of crystalline materials are presented in the subchapter 2.2 of this doctoral dissertation. Let us now take an insight into the models, insofar as these have to do with zirconia single crystals deformed at different temperatures.

As has been already pointed out, a certain number of Y ion – O vacancy dipoles exists in cubic zirconia. These may give rise to contributions to the flow stress by reorientation in the stress field of moving dislocations, the so-called Snoek effect. The latter can in turn cause transient effects after changes of the strain rate. However, since the stress increments owing to these are negligibly small [17], elastic interactions between dislocations and isolated point defects as well as small clusters of such defects cannot be of importance in the plastic deformation of cubic zirconia. As discussed and presented in [4, 17, 22], from 1000°C up to 1200°C, plastic deformation of cubic zirconia is controlled by athermal long-range interactions

between parallel dislocations (Taylor hardening). Furthermore, dislocations can be hindered by jogs in this temperature region, thereby forming dislocation loops.

At temperatures from 1000°C down to nearly 600°C, the solution-hardening may take place [27, 10, 26]. It is assumed in this model that a gliding dislocation takes a zigzag" configuration when it interacts with an array of transient pinning points, each pinning point comprising a cluster containing solute atoms (and possibly other point defects). Such a cluster contains Y^{3+} ions and charge compensating oxygen vacancies. In order to unpin the dislocation from the cluster, one has to supply an amount of stress.

In the same temperature range, precipitation hardening is believed to influence the flow stress of cubic zirconia single crystals in that dislocations interact with localized obstacles of possibly hafnium nature [21]. A similar model has been proposed for the deformation of cubic zirconia matrix with tetragonal ZrO_2 precipitates, too [27]. Unlike these, zirconium nitride (ZrN) precipitates were observed in c-ZrO_2 [79]. The origin of these is probably due to absorption of atmospheric nitrogen by liquid zirconia when the crystals are produced in air or by the skull melting process, the essence of which was also proved by [80, 81].

In [46, 47], the mechanisms controlling the plastic deformation were supposed to change gradually from the pinning by localized obstacles to the lattice friction below 700°C. The authors stated that kink pairs formed on segments of dislocations bowing out under the action of an applied stress, that is the authors did not separate both mechanisms but considered them to act simultaneously. With the pinning by localized obstacles predominant, the experimental activation volume appeared relatively large, which corresponded to low values of the strain rate sensitivity, whereas the lattice friction being of more influence, the activation volume was empirically found low, and high values of the strain rate sensitivity were thus obtained.

At the temperatures of 1300°C - 1600°C, thermal recovery takes place and governs plastic deformation of cubic zirconia [26, 75-77, 4, 19], i.e. a mechanism of

dislocation annihilation. The rate of the annihilation is controlled by a diffusional processes where dislocation climb is involved.

3.2.5. Aim of the present doctoral thesis

While the plastic deformation of cubic zirconia single crystals doped with 10mol% Y_2O_3 has been thoroughly investigated in the soft mode, i.e. involving macroscopic compression experiments along the $\langle 112 \rangle$ axis, the plastic deformation of cubic zirconia in the $\langle 100 \rangle$ compression direction is not very well studied. Moreover, the existing papers on the $\langle 112 \rangle$ material are geared primarily to cubic zirconia single crystals stabilized with 10mol% yttria, and there are only a couple of studies of cubic zirconium dioxide doped with any other concentration of Y_2O_3.

With respect to the aforesaid, the objective of the present doctoral dissertation is to investigate the plastic deformation of cubic zirconia single crystals doped with 10 mol% yttria in the $\langle 100 \rangle$ compression direction, expressly and extensively. In order to achieve this, compression experiments with a constant strain rate in air environment is to be used. Since the deformation in the $\langle 100 \rangle$ direction suppresses glide on the easy {100} planes, other slip systems must be activated at the deformation in this axis. That one can analyse the slip systems after relevant compression samples have been deformed, transmission electron microscopy observations are to be applied.

As the second part of this thesis, the plastic deformation of cubic zirconia single crystals stabilized with 15 and 20mol% yttria will be investigated, so that the concentration dependence of the flow stress of the material could be empirically found out. Finally, an interwoven and elaborated dependence of the flow stress of cubic zirconia on the concentration of yttria dopant and the deformation direction is to be postulated. According to the magnitude of experimental variables such as the strain rate sensitivity of the flow stress yielding the activation volume as well as the results of transmission electron microscopy analyses, the dislocation mechanisms responsible for the plastic deformation of cubic zirconia are to be determined.

4. Experimental

4.1. Macroscopic deformation experiments
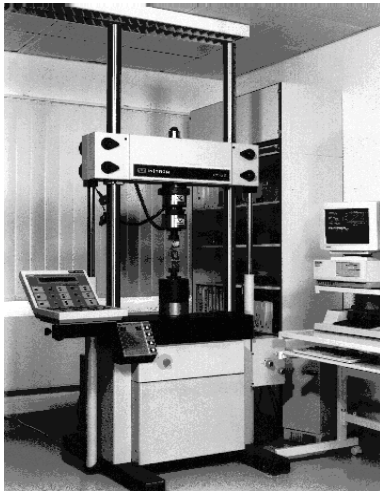
Fig. 4.1.1. Single-screw testing machine Instron 8562

The macroscopic deformation experiments were carried out in a single screw testing machine of the type Instron 8562 (Fig. 4.1.1.) in compression. It works by lifting the lower push rod gradually against the upper one by means of an electromechanical screw drive, so that a sample, inserted between both rods, can be deformed (Fig. 4.1.2.). When the screw is displaced, its position is registered, as well as the relevant load is measured by a load gage, and the change of the degree of the sample deformation is determined,

too, all of which can be used for working out a compression experiment. As a rule, only the change of the strain at a finite strain rate and the load are used. The deformation machine is digitally controlled. It enables to register both digital and analogue data. The temperature of the experiment can be set with an oven, which operates in air environment as a rule. As a potential reader is referred to the handbooks of the Instron company for a detailed description of the machine and the deformation process [82], these are dealt with in the following only briefly.
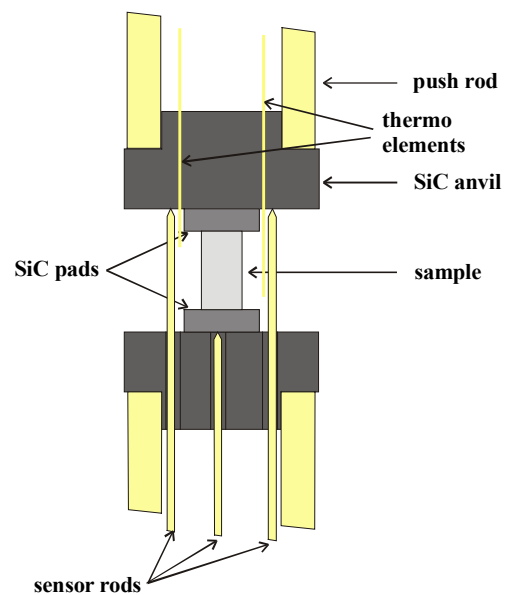
Fig. 4.1.2. A location of a sample during a compression test in Instron 8562

The upper and lower push rods are made of aluminum oxide (Al_2O_3). Their length is 310 mm, the width of their walls is 8 mm. The material of the upper and lower anvils is silicon carbide (SiC). Since the anvils are rather sensitive to the damaging imprint of the sample during compression, silicon carbide pads are inserted between the

sample grip faces and the anvils, for protection. These protective pads are 10 mm in diameter.

The load measuring gage is manufactured to function up to a maximum loading force of 10 kN. Because of durability of the aluminum oxide machine parts, the maximum loading force of 1 kN is set. The compression stress σ is calculated from the measured load and the initial cross-section of the deformed sample

$$\sigma = \frac{\left| \vec{f_c} \right|}{A}$$
(4.1.1)

Conveniently, the measuring gage of the strain is manufactured in such a way that the deformation process can be registered in close proximity of the sample. This gage is called the Linear Variable Displacement Transducer (LVDT). It is embedded in a water-cooled flange below the lower push rod. Information on the sample deformation degree is carried by three aluminum oxide sensor rods to the LVDT, one of which records the position of the lower surface of the lower pad, and the other two touch the upper SiC anvil. By means of a swing system, an average magnitude of the positions of both upper sensor rods is obtained. From this and the position of the lower anvil, the distance difference between the upper anvil and the lower pad is registered. Since the imprint of the sample into the anvils as well as the deformability of the preventing pads can be neglected on account of the high-temperature strength and stiffness of silicon carbide and the large cross-section of the pads, the measured displacement is almost equal to the sample deformation, according to the above-introduced procedure. During a compression experiment at a constant strain rate, the compliance of the frame of the Instron 8562 can be neglected because of the digital closed-loop operation of the machine in strain control. Mostly, compression samples are deformed only by a few percent of strain, because of which the strain is approximately computed as the difference between the initial value j_o and the variable value j of the strain recording divided by the initial length of the sample.

$$\varepsilon = \frac{j_o - j}{p_o}$$
(4.1.2)

In order to acquire scientific data within a compression experiment, the deformation machine is equipped with a General Purpose Interface Bus (GPIB) of National Instruments Corporation [83] and the data are lead to a PC using a program in

Turbopascal [4]. The program can be used for data acquisition and storage, although the control of an experiment is carried out manually. During such an experiment, data are recorded either after a step of 2 N load or of 0.2 μm strain. Also, the program enables to set other steps of both strain and load. The course of experiment can be displayed on the monitor as a stress-strain diagram, and it is also shown in form of curves written by the recorders simultaneously.

That compression experiments can be conducted at high temperatures, the deformation machine is equipped with an oven of the firm Severn Furnaces Limited [84]. An array of six molybdenum disilicide heating elements are mounted parallel to the furnace axis to provide symmetrical radial heating of the working chamber. The furnace is regulated with a Eurotherm 818 P controller. Its highest possible temperature is 1500°C. The outer face of the oven and the bases of the rods are water-cooled using a COLORA FK 3500 heat exchanger. In order to protect the push rods from a thermal shock, the oven's temperature can be changed by 12 K per minute, both at heating and cooling. The upper push rod is provided with two additional thermoelements, so that the temperatures near the upper and lower ends of the compression sample can be measured.

Before a compression test at both high and low temperature is started, one has to make sure that the grip faces of the sample fit the upper and lower pads in that the sample faces and the surfaces of anvils should be as parallel as possible, in order to achieve uniaxial loading. Furthermore, to avoid temperature gradients near the sample, two convex ceramic shields are placed in the oven, so that these encircle the sample completely. Finally, the oven is closed and clamped. A compression experiment can be started as soon as the experimental temperature is constant, and the strain oscillations are lower than 0.02 μm/min.

Mostly, experiments are performed at a constant strain rate, although the latter is changed in order to carry out strain rate cycling tests (SRC) for the sake of obtaining the strain rate sensitivity of the flow stress, or the deformation process is stopped when making relaxation tests (SR). That the temperature sensitivity of

the flow stress can be obtained, the temperature cycling tests are conducted, too. When the temperature is being changed, the sample should partially be unloaded, so that the plastic strain will not change, unregistered. If a compression experiment is finished by quickly unloading the sample at constant temperature, the elastic stiffness of the sample can be determined.

4.2. Transmission electron microscopy experiments

The dislocation structure of the deformed compression samples of cubic zirconia was investigated by transmission electron microscopy techniques. As a device for the experiments, the JOEL High-Voltage Electron Microscope JEM 1000 (HVEM) was used, a microscope that makes for in-depth studies of the dislocation structure of crystalline solids. Since the maximum acceleration voltage of the microscope is 1000 kV as well as its penetrating power is about 2.8 times that of a 100 kV transmission electron microscope, investigated specimens can be fairly thick [85]. In the same reference, a reader can also find the apparatus and principle of work of this microscope. Although cubic zirconia single crystals doped with yttria are electrically non-conductive, the specimens did not need coating because of the high accelerating voltage.

4.3. Diffraction patterns and dislocation contrast in a TEM

4.3.1. Diffraction of electrons

Because of the small wave-length of electrons λ, a very small diffraction angle is characteristic of the electron beam when the latter leaves the surface of the specimen. Therefore, the reflecting lattice planes are nearly parallel to the primary electron beam (see [86]). Assume a crystalline specimen and the primary beam falling onto its surface (Fig. 4.3.1.). According to the figure, L is the distance between the specimen and the photographic film (camera length), ß is the Bragg angle, and R the distance on the photographic plate between the transmitted beam

4.3.1. The basics of electron diffraction

and a diffraction spot. Besides, ß approximately equals to R/2L since the diffraction angle is small. Consequently, the Bragg equation can be written as

$$\lambda L = Ra \qquad (4.3.1)$$

where a is the interplanar spacing. When electrons are of the same energy, the product λL is constant. Therefore, a conclusion can be drawn that the distance R of each diffraction spot from the primary beam is inversely proportional to the interplanar spacing a, as well as the position vector of each diffraction spot $\vec{R}$ is normal to its relevant diffracting plane.

Fig. 4.3.2. A scheme on the relation between real and reciprocal space
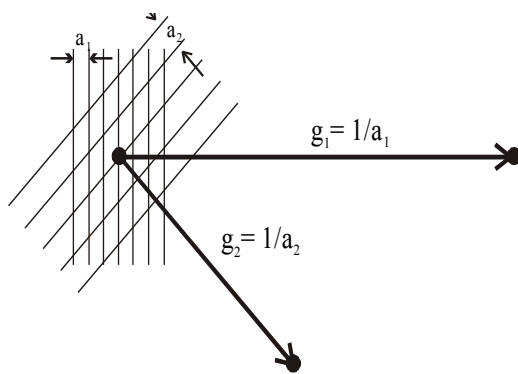
Diffraction patterns of crystals are interpreted by the model of a reciprocal lattice. While the definition of a reciprocal lattice and its unit vectors can be found elsewhere [86], we confine to a statement which is, however, essential to transmission electron microscopy

$$|\vec{g}| = \frac{1}{a} \qquad (4.3.2)$$

where $\vec{g}$ is the position of the lattice points of a reciprocal lattice, or the reciprocal lattice vector, as shown in Fig. 4.3.2. Hence, eq. (4.3.1) can be rewritten

$$R = \lambda L g \qquad (4.3.3)$$

Following the equations and statements introduced in this chapter, diffraction patterns can be constructed and indexed. One assumes to look from above -- along the direction of the primary beam -- onto the crystal and considers which planes with what a-values are parallel to the beam. Besides, one has to take into account the extinction law, which says reflections occur only on planes with unmixed indices.

4.3.2. Dislocation contrast

Dislocation contrast and extinction will be considered below only insofar as these are relevant to the objective of this dissertation; a kinematic theory of diffraction to explain contrast observation in transmission electron microscopy can be found elsewhere   [86].

When the electron beam encounters a dislocation or rather a space wherein lattice planes are bent due to the distortion caused by the dislocation, the intensity of the directly transmitted beam will be reduced (and that of the diffracted beam increased). As a result, the dislocation will appear as a dark line in the bright-field image (or as a bright line in a dark-field image). This line can also be invisible, which may be exploited to determine the Burgers vector of the dislocation.

A dislocation is invisible when its Burgers vector is orthogonal to the imaging vector of the reciprocal lattice (e.g. [87]), that is when

$$\vec{g} \cdot \vec{b} = 0 \tag{4.4.4}$$

More generally, only a screw dislocation is invisible when imaged with a reflection for which eq. (4.4.4) is valid. If the specimen is tilted in the microscope to find two different diffraction vectors $\vec{g}_1$ and $\vec{g}_2$ for which the dislocation line is invisible, its Burgers vector must be perpendicular to both $\vec{g}_1$ and $\vec{g}_2$ and therefore has the direction of $\vec{g}_1 \times \vec{g}_2$. For an edge dislocation, all planes parallel to its line are bent, which is why an edge dislocation does not disappear completely when imaged with $\vec{g} \cdot \vec{b} = 0$, but a very small contrast is still present. However, its Burgers vector can still be determined.

4.4. Preparation of samples

4.4.1. Macroscopic compression samples

In this work, three sets of cubic zirconia single crystals were used. The first of these was ZrO_2-10mol%Y_2O_3 single crystals oriented for the deformation in the $\langle 100 \rangle$ axis. The second and the third sets were both oriented along $\langle 112 \rangle$ for easy glide on $\{100\}$ planes, but the dopant concentration of these was different, namely 15mol% and 20mol% yttria. The crystals were oriented using the Laue back-reflection X-ray technique.

Compression samples were made according to the following scheme: the oriented crystals were cut into small bars by a wire saw and boron-carbide slurry, taking due account of the compression axes of the samples. In order to make their opposite sides parallel, these were ground with a Multipol precision polishing machine using a

mixture of boron-carbide powder and glycerine. Finally, the samples were successively polished with diamond pastes whose polishing particles were 3 μm and 1 μm in diameter, respectively. For this, a Minimet polishing machine was used.

Since edges of a rectangular deformation sample often contain microcracks that can become sources of unplanned and undesirable brittle fraction even before any essential portion of plastic deformation can be attained [88, 89], these were polished with abrasive paper, after which they were finally polished with 6 μm down to 1 μm diamond pastes sprayed onto the rough side of photographic paper. On account of the high brittleness of cubic zirconia single crystals, particularly of high concentrations of Y_2O_3, many compression samples were irretrievably damaged so that they could not be studied in compression. Otherwise, the samples were as closely as possible $2*2*8$ mm^3.

4.4.2. Transmission electron microscopy specimens

That the dislocation structure of cubic zirconia single crystals can be investigated, some of the compression samples deformed along ⟨100⟩ were used to prepare transmission electron microscopy foils. The specimens were cut into slices about 400 μm in thickness, ground and polished in the same way as the compression samples discussed above. The final thickness of the specimens was from 150 μm to 200 μm. After that, the specimens were dimpled with copper and rubber wheels, successively, so that the final thickness in the center of the specimens was about 40 μm. Further, the specimens were thinned down to 1 μm by ion milling with argon ions of 3-5 kV and a beam current up to 3 mA, after they had been glued onto aluminum ringlets for further convenient handling.

5.   Experimental results of the compression experiments

In the following chapters, the results of the performed compression experiments are presented considering two points of view, namely the dependence of the plastic properties of ZrO_2-10mol%Y_2O_3 single crystals on the orientation of the deformation axis as well as that of zirconia single crystals oriented along the soft $\langle 112 \rangle$ axis on the yttria concentration.

5.1. Effect of the deformation axis

Typical stress-strain curves of the compression experiments with ZrO_2-10mol%Y_2O_3 single crystals deformed along the $\langle 100 \rangle$ axis in air are shown in Fig. 5.1.1.
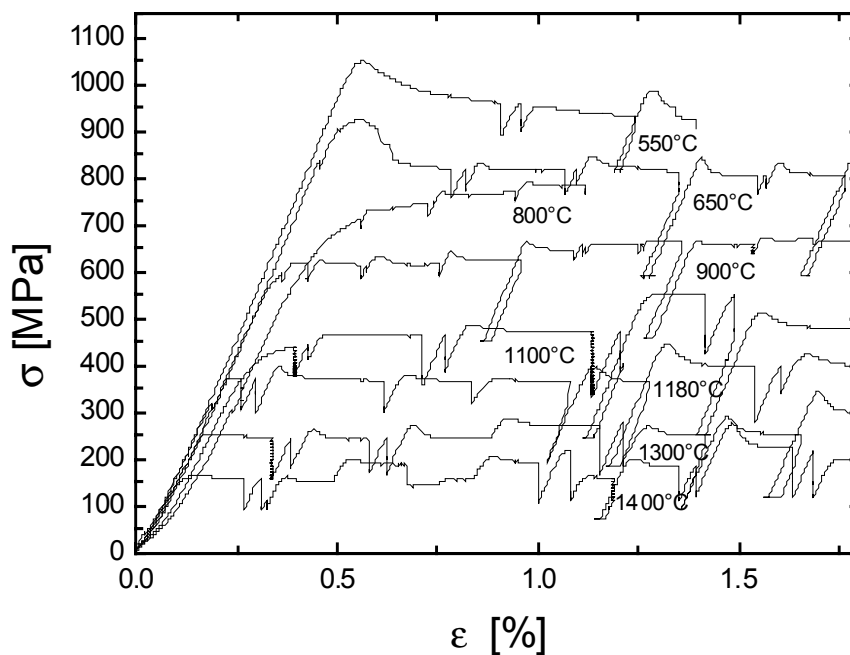
Fig. 5.1.1. Stress-strain curves of ZrO_2-10mol%Y_2O_3 deformed
in the $\langle 100 \rangle$ compression direction

The basic strain rate of all the experiments along this compression axis was 10^{-5} s^{-1}, except an experiment at 800°C done at 10^{-6} s^{-1} and an experiment at 1150°C performed at 10^{-4} s^{-1} (these are not shown in the figure but nevertheless used for the further evaluation).

5.1.   Effect of the deformation axis

Within all compression tests, SRC and SR experiments have been carried out to measure the strain rate sensitivity of the flow stress. The behavior of the flow stresses of the displayed curves is compared to that shown in Fig. 3.2.2 and obtained before [4], where the deformation axis was $\langle 112 \rangle$, and the stain rate 10^{-6} s^{-1}.

According to the shape of the curves of specimens deformed along $\langle 100 \rangle$, three temperature ranges can be distinguished. In the range from 1400°C down to about 1200°C, a yield point effect does not occur after the primary loading, but takes place after almost every change of the strain rate. No work hardening is observed in this temperature range, which is also the case for the curves of the samples deformed along $\langle 112 \rangle$. In the intermediate temperature range from 1100°C down to 800°C, the deformation curves along $\langle 100 \rangle$ do not exhibit a yield point effect during primary loading, but work hardening is registered. The stress-strain curves along $\langle 112 \rangle$ show the same phenomena at intermediate temperatures, the upper limit of which is 1200°C, though. Finally, the low temperature region starts occurring at 650°C for $\langle 100 \rangle$ and at 600°C for $\langle 112 \rangle$ compression axes. In this region, a very pronounced yield drop effect occurs after the initial loading without any work hardening thereafter. However, yield drop effects appear after stress relaxation tests. The work hardening rates of the $\langle 100 \rangle$ deformation curves are listed in Tab. 5.1.1. together with those obtained by [4] for the $\langle 112 \rangle$ deformation.

Table 5.1.1. The work hardening rates of ZrO_2-10mol%Y_2O_3 single crystals deformed along the $\langle 100 \rangle$ and $\langle 112 \rangle$ [4] compression axes.

Temperature [°C]	Work hardening coefficient, Θ [GPa]	
	$\langle 100 \rangle$ compression axis	$\langle 112 \rangle$ compression axis
1400	0.770	-0.769
1300	0.631	-
1200	4.641	5.736
1000	4.738	4.711
900	3.970	7.032
800	9.573	6.994
700	3.198	4.574
600	-1.711	-2.812
550	-7.570	-5.908

According to the table, the work hardening coefficient is very small or even negative at high temperatures for both compression directions. Since the intermediate temperature region for the $\langle 112 \rangle$ deformation starts from 1200°C, the values of the work hardening are larger at this compression axis than those for the $\langle 100 \rangle$ direction at the same temperature. For both orientations, the hardening coefficients increase with decreasing temperature, but they begin decreasing below 800°C. Below this temperature, the work hardening disappears, and the corresponding coefficients are again negative.

For the deformation in the $\langle 100 \rangle$ compression direction, the yield stress (critical flow stress) is displayed in Fig. 5.1.2 as a function of temperature. In addition, the temperature dependence of the yield stress along $\langle 112 \rangle$ is shown in this figure, too. These values are estimated from the stress-strain curves exhibited in Fig. 3.2.2. Since several of the stress-strain curves of both compression axes did not contain yield point effects, the yield stresses were obtained by extrapolation of the stress-strain curves to zero plastic strain.
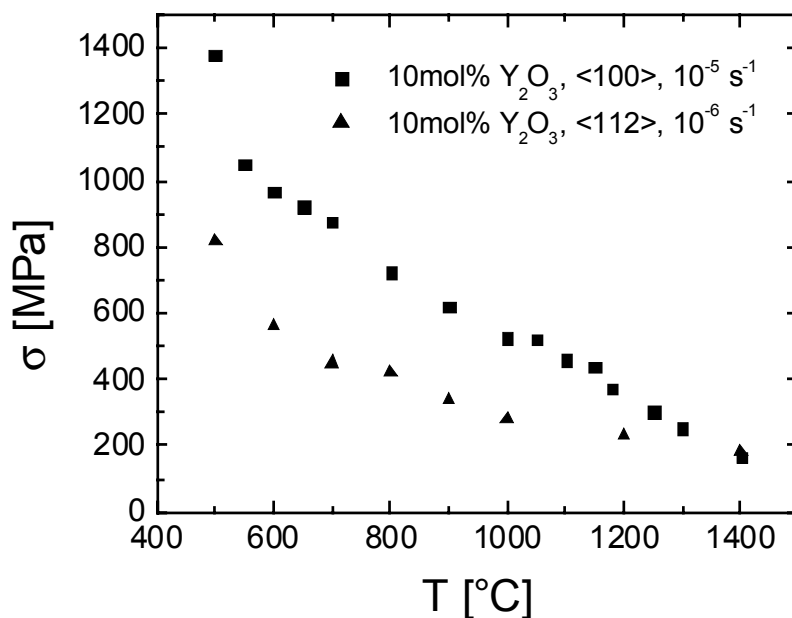
Fig. 5.1.2. Temperature dependence of the flow stress of c-ZrO$_2$ stabilized with 10mol%Y$_2$O$_3$ along $\langle 100 \rangle$ and $\langle 112 \rangle$ axes

As shown in Fig. 5.1.2., the yield stresses of both orientations are the same only at 1400°C, being somewhat lower than 200 MPa. From 1200°C down to 800°C, the critical flow stress values of the specimens deformed along $\langle 100 \rangle$ are almost twice as high as those of the samples deformed along $\langle 112 \rangle$. The values of the yield stresses along $\langle 100 \rangle$ increase from 400 MPa up to 800 MPa with decreasing temperature; the values of those along $\langle 112 \rangle$, from 200 MPa up to 400 MPa, respectively. Below 800°C, the difference in the yield stresses between both orientations remains approximately constant. Their maximum magnitudes constitute 1400 MPa for the $\langle 100 \rangle$ and 800 MPa for the $\langle 112 \rangle$ compression direction.

The temperature sensitivity of the $\langle 100 \rangle$ flow stress obtained from temperature cycling tests is shown in Fig. 5.1.3. It was calculated using the following method: After the temperature of a compression experiment had been changed, the corresponding stress increment was measured. This increment was between the first steady state and the second steady state, both of which straddled the temperature alteration.

When a work hardening region occurred after the temperature had been altered, the hardening coefficient was also taken into consideration in order to amend the upper flow stress, in which case the latter was obtained using the formula
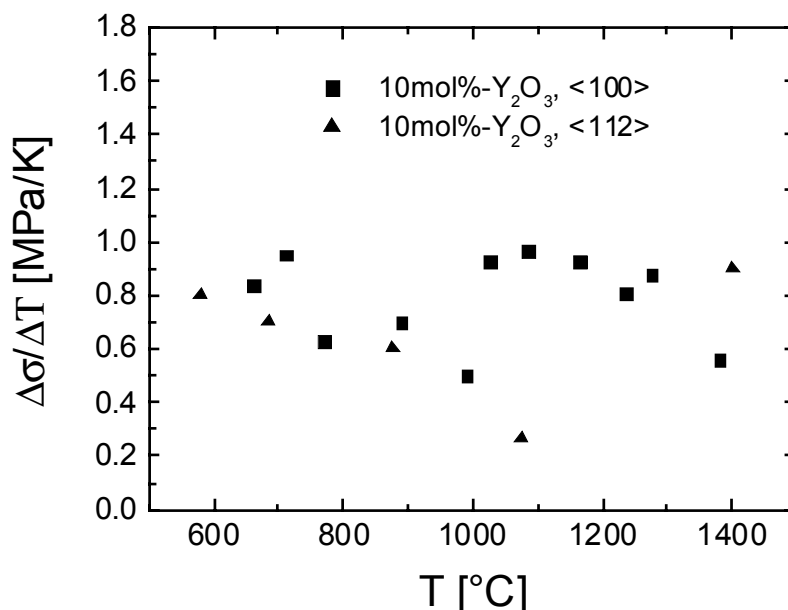
Fig. 5.1.3. Temperature sensitivity of the flow stress $\Delta\sigma/\Delta T$ of ZrO_2-10mol%Y_2O_3 along the $\langle 100 \rangle$ and $\langle 112 \rangle$ axes

$\sigma_{up.} = \sigma_{rel.} - \Theta * \Delta\varepsilon$, where $\sigma_{up.}$ is the flow stress of the second steady state, $\sigma_{rel.}$ is the starting stress of the relaxation test adjacent to the temperature cycling experiment after the temperature is changed, Θ is the hardening coefficient along the stress-strain curve between this relaxation and the position, up to which the work hardening was measured, and $\Delta\varepsilon$ is the strain increment between the reloading part of the stress-strain curve and the relaxation test adjacent to the temperature cycling experiment after the temperature is altered.

Finally, the calculated stress increment was divided by the temperature difference, the result of which constituted the temperature sensitivity. For comparison, the temperature sensitivity of the flow stress of ZrO_2-10mol%Y_2O_3 along $\langle 112 \rangle$ is also shown in the figure. While the temperature sensitivity of the flow stress of the cubic zirconia single crystals deformed in the $\langle 112 \rangle$ compression direction decreases constantly from 0.8 MPa/K down to 0.3 MPa/K in the temperature range 600 - 1100°C and increases up to 0.9 MPa/K at 1400°C, that of the flow stress of the cubic zirconia single crystals deformed in the $\langle 100 \rangle$ axis decreases from about 0.9 MPa/K down to 0.4 MPa/K within the temperature range of 650 - 1000°C and rises to 0.9
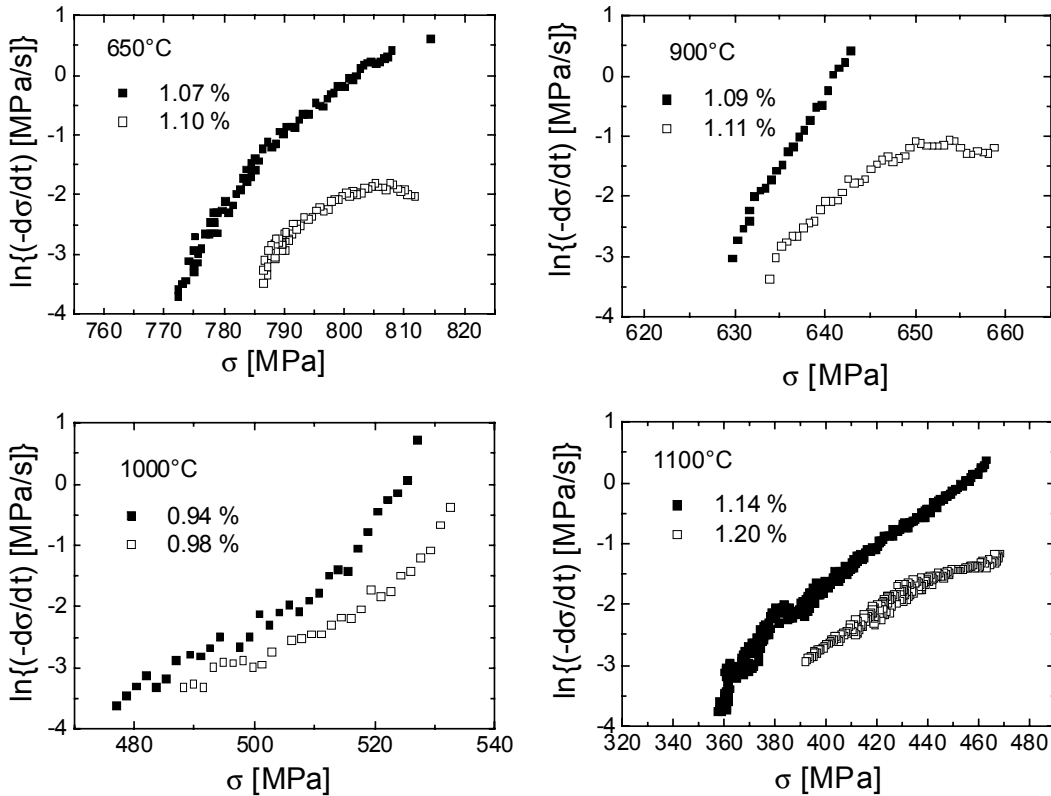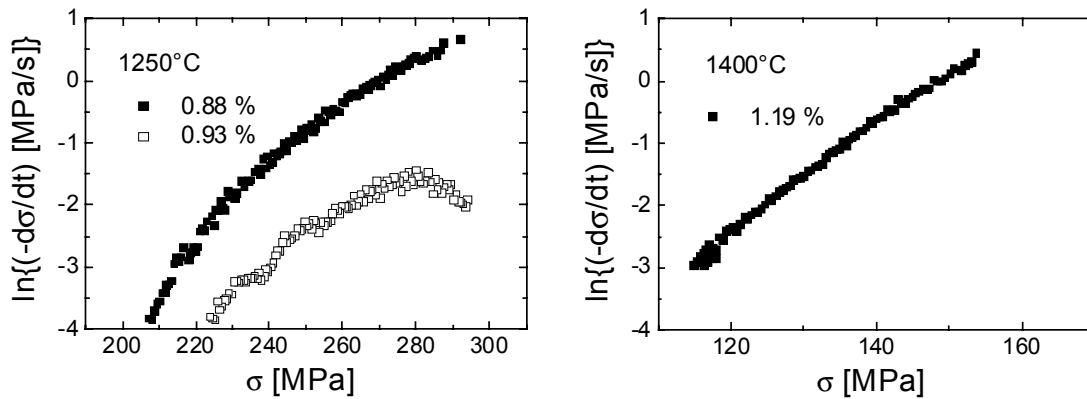
Fig. 5.1.4. Typical stress relaxation curves during compression experiments on ZrO_2-$10mol\%Y_2O_3$ deformed in $\langle 100 \rangle$. The strain is near 1 %. Solid symbols correspond to primary relaxation curves; open ones, to repeated relaxation curves.

MPa/K after a little higher than the latter temperature. It remains constant till around 1150°C and then decreases, reaching 0.56 MPa/K at 1400°C.

As mentioned above, stress relaxation tests have been carried out within the compression experiments with the ZrO_2-$10mol\%Y_2O_3$ deformed in $\langle 100 \rangle$. Typical relaxation curves are shown in Fig. 5.1.4.

Primary relaxation curves differ from repeated relaxation curves in that the latter start after the reloading of primary relaxation tests before the yield point effect can occur. Therefore, one may say that the amount of plastic strain attained between the primary relaxation and the following repeated relaxation is very low. Repeated relaxations are performed in order to study the change in the microstructure of the material during relaxations.

The form of the relaxation curves in Fig. 5.1.4. is mostly convex upwards, except the relaxation curves of the compression experiment done at 1000°C whose forms are concave. This may indicate that there are two different dislocation processes involved during these relaxations, whereas a continually convex form suggests a single dislocation process, as is the case with the other relaxation curves.

As was already mentioned in chapter 2.3.2., the inverse slope of the relaxation curves constitutes the strain rate sensitivity. In order to estimate the slope of the curves shown in Fig. 5.1.4., the data were approximated using polynomial regression of the type $\ln(-\dot{\sigma}) = a + b\sigma + c\sigma^2$. Hence, the strain rate sensitivity corresponding to the deformation before the relaxation test was calculated according to $r = 1/(b + 2c\sigma)$, where σ is the stress at the beginning of the stress relaxation test.

Since the strain rate sensitivity of the flow stress along ⟨100⟩ depended on the plastic strain attained, the dependence of r on temperature should be displayed at a certain magnitude of the plastic strain. This strain should be the same for all compression experiments. Therefore, the values of the strain rate sensitivity were plotted versus the plastic strain and were then extrapolated to zero magnitude of strain. Finally, the
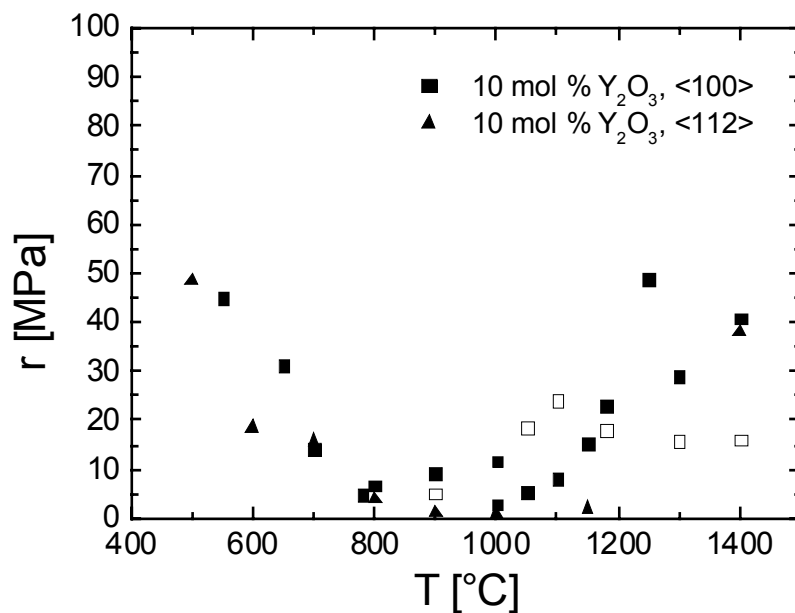
Fig. 5.1.5. Strain rate sensitivity of ZrO$_2$-10mol%Y$_2$O$_3$. The deformation axes are ⟨100⟩ (squares) and ⟨112⟩ (triangles) [4]. Solid symbols correspond to SR tests; open ones, to SRC tests.

extrapolated values were plotted in Fig. 5.1.5. against the temperatures of the compression experiments together with the values of the strain rate sensitivity derived from strain rate cycling tests. Taking due account of the data scatter, the curves for the ⟨100⟩ and ⟨112⟩ axes are qualitatively equal. Both start at about 45 MPa at low

temperatures, manifest a minimum from 800°C to 1000°C and increase again up to 40 MPa at 1400°C. The two values at 1000°C correspond to the two ranges of the inversely curved stress relaxation curves.

In Fig. 5.1.5., one also notices that the strain rate sensitivity along $\langle 100 \rangle$ measured from strain rate cycling experiments differs considerably from that of stress relaxation tests in the temperature range from 1000°C up to 1300°C. This is because the values of r derived from the strain rate cycling tests were so few that they could not be extrapolated to zero plastic strain but were plotted at whatever plastic strains they had been obtained.

5.2. Effect of yttria content
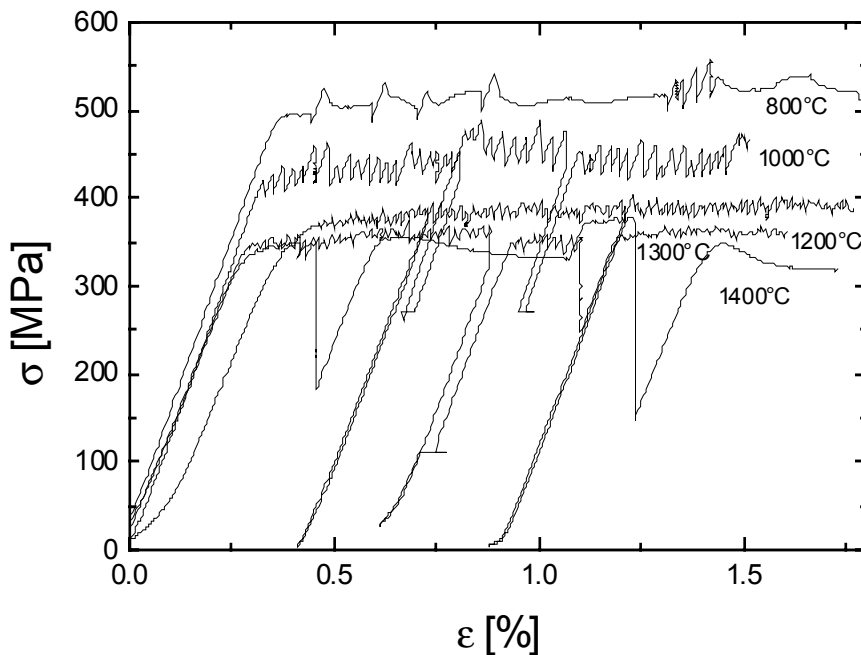
Fig. 5.2.1. Stress-strain curves of ZrO_2-15mol%Y_2O_3
deformed in the $\langle 112 \rangle$ compression direction

Typical stress-strain curves of the compression experiments with ZrO_2-15mol%Y_2O_3 single crystals deformed along the $\langle 112 \rangle$ axis in air are shown in Fig. 5.2.1. The basic strain rate of this set of experiments was 10^{-5} s^{-1}. Let us compare the behavior of the stress-strain curves of this material with that of ZrO_2-10mol%Y_2O_3 studied in [4] along the same compression axis (Fig. 3.2.2.).

In general, only the curves at 1400°C and 800°C have a similar shape for both concentrations of yttria stabilizer, although at 1400°C, the yield point effect after each stress relaxation test is more pronounced for the 15mol% material. The yield drop effect occurs at 800°C for the ZrO_2-15mol%Y_2O_3 single crystals, too, which is not observed for the 10mol% material. Unlike the stress-strain curves of the 10mol% cubic zirconia deformed along $\langle 112 \rangle$, in the temperature range from 1300°C down to some temperature above 800°C, serrated flow occurs at the 15mol% material. The serrations are particularly noticeable at 1000°C. Their amplitude along the axis of stresses is the highest at this temperature.
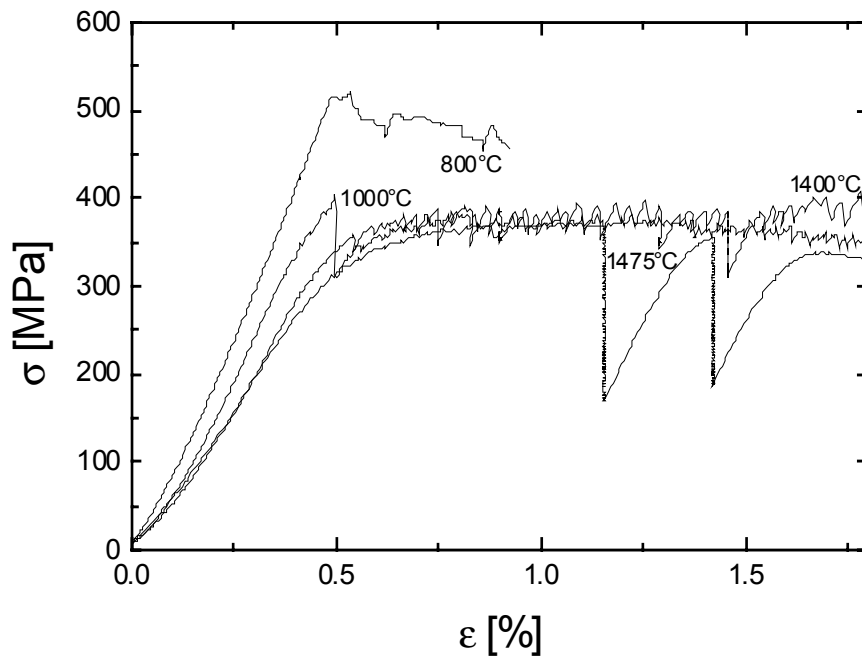
Fig. 5.2.2. Stress-strain curves of the ZrO_2-20mol%Y_2O_3
deformed in the $\langle 112 \rangle$ compression axis

Fig. 5.2.2. displays typical stress-strain curves of ZrO_2-20mol%Y_2O_3 deformed in the $\langle 112 \rangle$ compression orientation in air. The flow stress of the 20mol% material is approximately equal to that of the 15mol% material at the respective temperatures. The compression test at 1000°C obviously failed at about 0.5 % total strain, which is why its flow stress did not become higher than that of the experiment at 1400°C. Serrated flow occurs at high temperatures, being less prominent at 1475°C. The yield point effect is observed only at 800°C, though this may well be just a very unstable deformation.

For the stress-strain curves of the 15mol% material, the work-hardening coefficient was measured. It amounted to 1.85, 2.12, and 1.85 GPa at 800°C, 1000°C, and 1200°C, respectively. These are about half the values of those of the 10mol% material. For the 20mol% material, the work-hardening coefficient was zero.

Fig. 5.2.3. presents the temperature dependence of the yield stresses of the 15 and 20mol% materials together with that of the 10mol% material taken from Fig. 3.2.2. The yield stresses of the three materials decrease with increasing temperature, and the data of the 20 and 15mol% materials are almost equal. The two materials of high
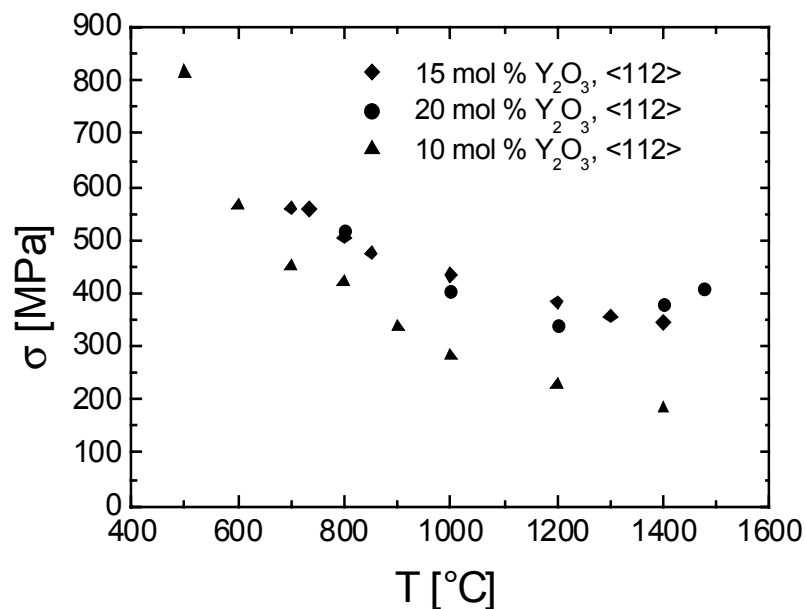
Fig. 5.2.3. Temperature dependence of the flow stress of ZrO_2-15 and 20mol%Y_2O_3 deformed in $\langle 112 \rangle$ versus that of ZrO_2-10mol%Y_2O_3 [4]

yttria content show a higher flow stress than that of the 10mol% material. This difference increases from about 100 MPa at 800°C up to 200 MPa at 1400°C.

Fig. 5.2.4. compares the temperature sensitivity of the flow stress of the 15 and 20mol% yttria materials with that of the 10mol% zirconia. $-(\Delta\sigma / \Delta T)$ was again determined from temperature cycling tests. Considering the scatter of the data, the values are equal for all materials at the respective temperatures. They decrease from about 0.6 MPa/K down to 0.1 MPa/K in the temperature range from 700 – 1200°C and then increase again, the temperature sensitivity of the 15mol% material being the

highest at 1400°C. It amounts to 1.5 MPa/K. This magnitude is almost twice as high as that of the 10mol% zirconia and three times higher than that of the 20mol% material at this temperature.
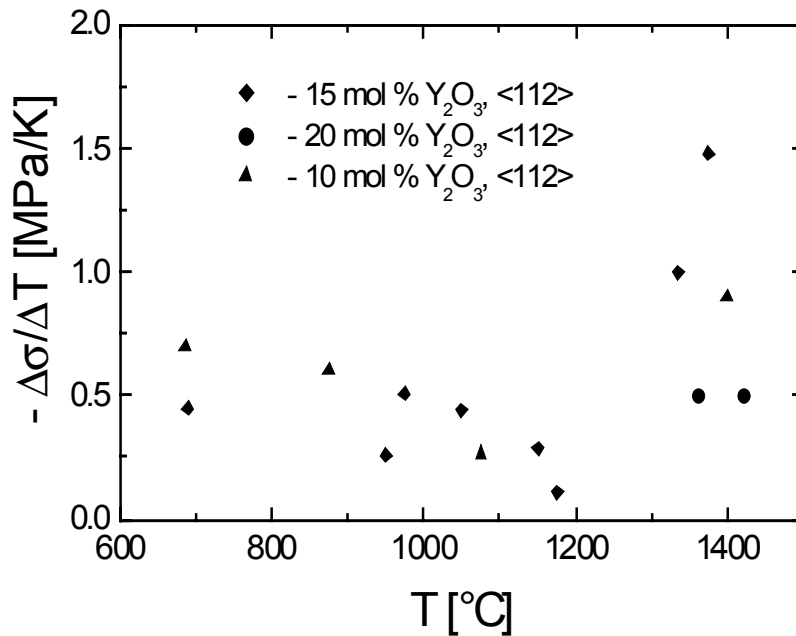
Fig. 5.2.4. The temperature sensitivity of the flow stress of ZrO_2-15 and 20mol%Y_2O_3 deformed in $\langle 112 \rangle$ versus that of ZrO_2-10mol%Y_2O_3 [4]

As with the ZrO_2-10mol%Y_2O_3 deformed in the $\langle 100 \rangle$ compression direction, relaxation tests were also performed with the 15mol% material, several of which are shown in Fig. 5.2.5. Their form is similar to that of most relaxation curves of the 10mol% cubic zirconia deformed along $\langle 100 \rangle$, which is convex.
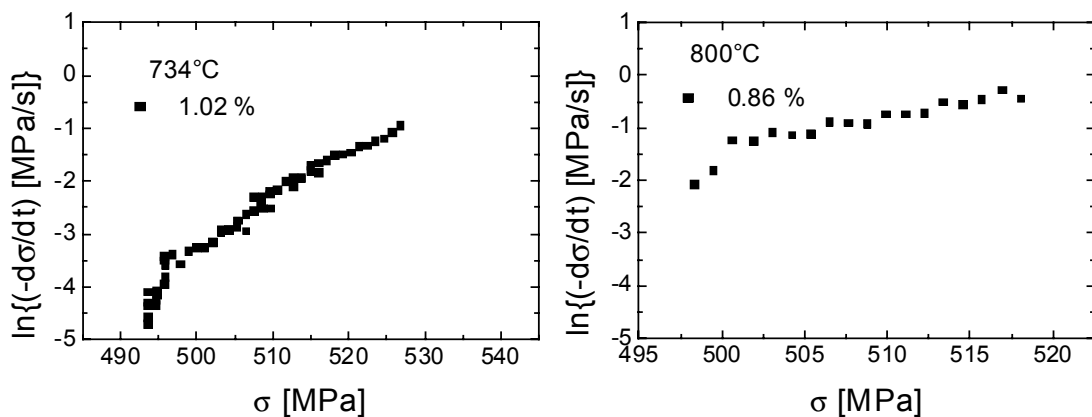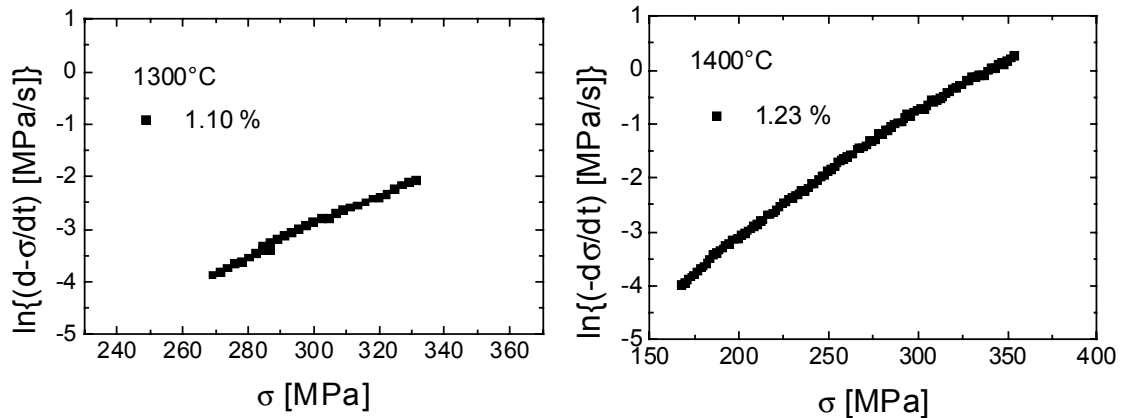
Fig. 5.2.5. Typical relaxation curves during compression experiments on the ZrO_2-15mol%Y_2O_3 in $\langle 112 \rangle$. The plastic strain is near 1 %.

The strain rate sensitivity r of the flow stress of the 15 and 20mol% materials was calculated from the SR and SRC tests using the methods described in Section 5.1. When the serrated flow took place, the strain rate sensitivity could not be estimated by this method. However, r was finally determined, albeit by another method. It consisted in plotting the decreasing stresses of the relaxation tests versus time. Then, two successive parts of the curves were approximated using above regressions. That the approximated stress-time curves did not contain stress drops was essential.

Along each regression interval, two time points t_1 and t_2 were selected. Using these, the corresponding stresses were calculated by $\sigma_i = A + A_1 t_i + A_2 t_i^2$ and the stress rate by $\dot{\sigma}_i = A_1 + 2 A_2 t$. Finally, the strain rate sensitivity r was determined using the formula $r = \dfrac{\Delta \sigma}{\ln \{ |\dot{\sigma}_1| / |\dot{\sigma}_2| \}}$.

The results of the extrapolation of the strain rate sensitivity to zero plastic strain are demonstrated in Fig. 5.2.6. Within the scatter of the data, the strain rate sensitivities of all the three materials are equal. These decrease from 50 MPa at 500°C down to almost zero between 1000°C and 1200°C and start increasing thereafter.
Unfortunately, only a single (very high) value is available for the 20mol% material above 1400°C.
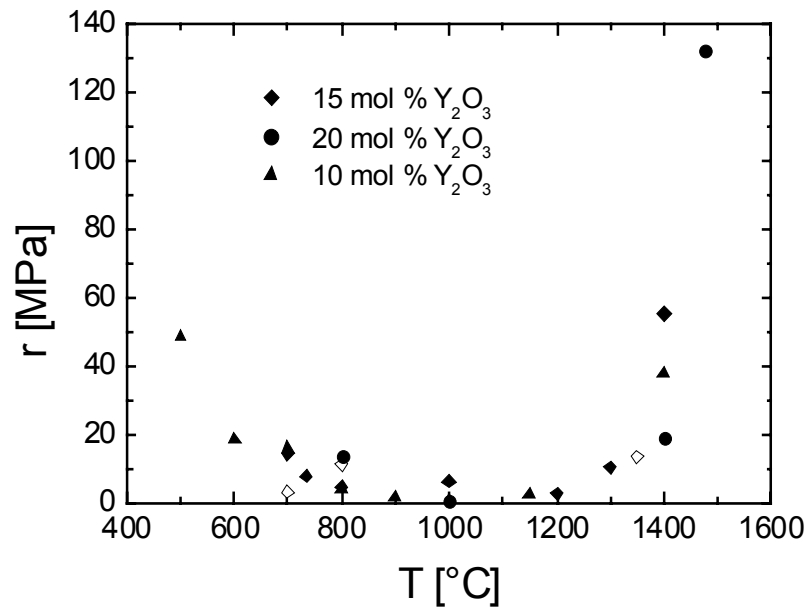
Fig. 5.2.6. Strain rate sensitivity of ZrO_2-15 and 20mol%Y_2O_3. The deformation axis is $\langle 112 \rangle$. Open symbols correspond to SRC tests; solid ones, to SR tests

5.3. Plastic instabilities in cubic zirconia single crystals

As already mentioned in section 5.2., the plastic deformation along the $\langle 112 \rangle$ orientation may become unstable within some ranges of the stabilizer concentration, the deformation temperature, and the strain rate. The unstable behavior consists in rapid load drops along the stress-strain curve, and the drops are followed by a reloading phase. The phenomenon may be called serrated yielding or the Portevin-LeChatellier (PLC) effect. Hence, the plastic instabilities along the stress-strain curve are conveniently called "serrations".

In order to study the ranges where the plastic instabilities occur, deformation experiments were in most detail carried out on the material containing 15mol% yttria at different temperatures and strain rates of 10^{-6} and 10^{-4} s^{-1} in addition to the standard strain rate of 10^{-5} s^{-1}. Fig. 5.3.1 presents a deformation curve at a standard strain rate of 10^{-5} s^{-1} at temperatures between 1300°C and 800°C. This figure shows that the deformation takes place in an almost stable way at 1300°C, turns unstable between
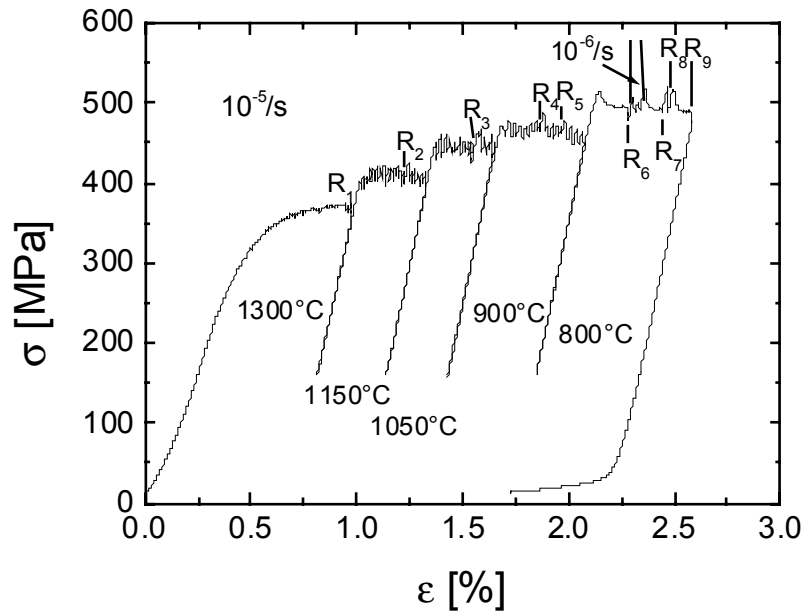
Fig 5.3.1. Stress-strain curve of ZrO_2-15mol%Y_2O_3
deformed in $\langle 112 \rangle$ from 1300°C to 800°C.

1300°C and 1160°C and becomes stable again between 900°C and 800°C, although the plastic instabilities occur at 800°C when the strain rate is diminished to 10^{-6} s^{-1}. The phenomenon is displayed in the next figure more thoroughly. Stable deformation at 800°C and a strain rate of 10^{-5} s^{-1} becomes unstable by changing the strain rate to 10^{-6} s^{-1} (Fig. 5.3.2a), but becomes stable again with the same rate change at about 1350°C (Fig. 5.3.2b).
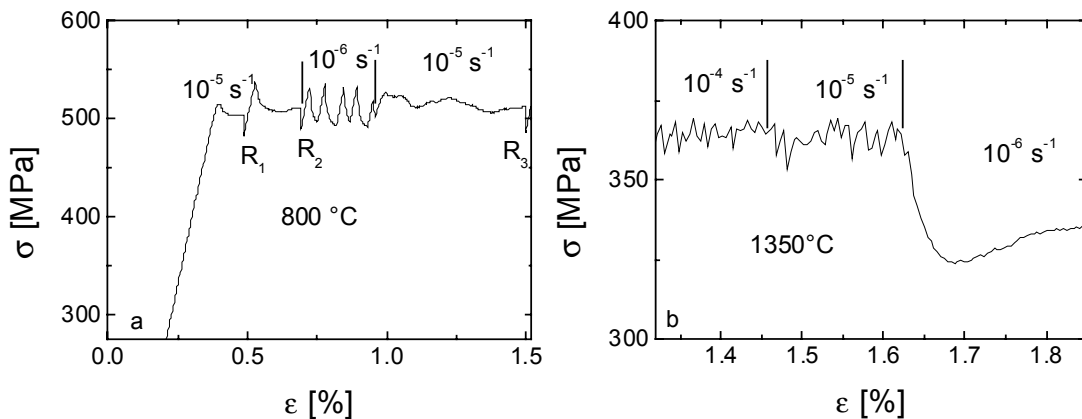
Fig. 5.3.2. Parts of the stress-strain curves of ZrO_2-15mol%Y_2O_3
deformed in $\langle 112 \rangle$; a: 800°C, b: 1350°C.

Fig. 5.3.3 summarizes all plastic instabilities occurring in the 15mol% material. Their amplitude along the corresponding stress-strain curves, which is measured in MPa, was chosen to represent the magnitude of plastic instabilities. Since this variable turned out to depend both on the experimental temperature and strain rate, a three-dimensional plot was needed.
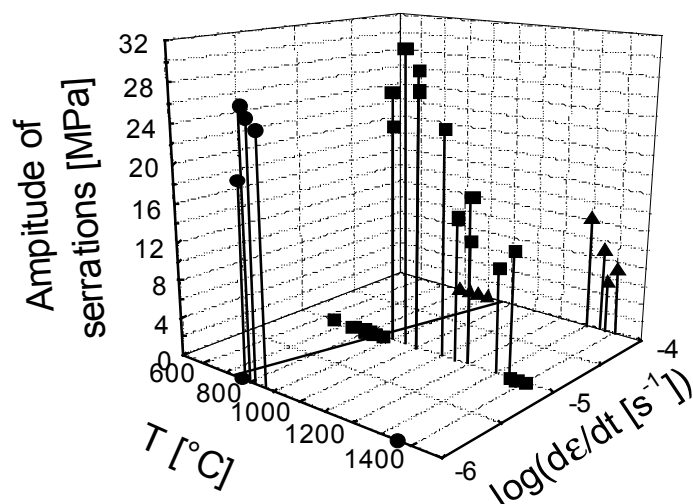
Fig. 5.3.3. The temperature and strain rate effects on the amplitude of the plastic instabilities in ZrO_2-15mol%Y_2O_3 deformed in $\langle 112 \rangle$

According to the plot, the lower border of the instability range shifts from about 750°C at a strain rate of 10^{-6} s^{-1} to probably 950°C at 10^{-4} s^{-1}, i.e. no serrations take place below these temperatures at the respective strain rates.

The magnitude of plastic instabilities attains 24-28 MPa at small strain rates and temperatures from 800°C to 1000°C, whereupon the amplitude starts to decrease down to 12-17 MPa with increasing temperature. This value exceeds the amplitude of serrations at 10^{-4} s^{-1} at yet higher temperatures, which ranges from 8 MPa up to 12 MPa.

Well expressed plastic instabilities had not been observed on cubic zirconia with 10mol% yttria. At 20mol% yttria and a strain rate of 10^{-5} s^{-1}, the upper border of the

instability range is shifted to higher temperatures above 1450 °C with respect to the 15mol% crystals. The lower border is below the brittle to ductile transition temperature.

When serrated flow takes place, the shape of the stress-strain curves depends on the temperature as demonstrated by Fig. 5.3.4.
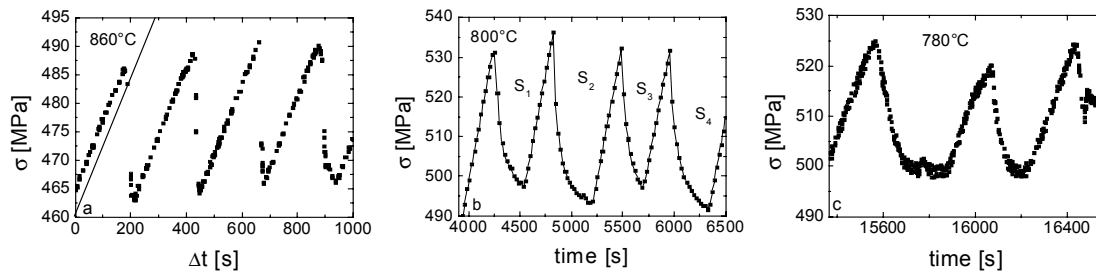
Fig. 5.3.4. The temperature effect of the shape of the stress-strain curves in ZrO$_2$-15mol%Y$_2$O$_3$ deformed in $\langle 112 \rangle$, $\dot{\varepsilon} = 10^{-6}$ s^{-1}

In the middle of the instability range, the stress drops are occurring very fast (Fig. 5.3.4a). The reloading curves are straight. Their slope $\dot{\sigma}$ divided by the strain rate of $\dot{\varepsilon} = 10^{-6}$ s^{-1} yields $d\sigma/d\varepsilon = 125$ GPa (straight line at the left side). Within the experimental accuracy, this value equals the stiffness modulus S of the sample measured during unloading. Thus, the reloading takes place in the elastic mode. If the
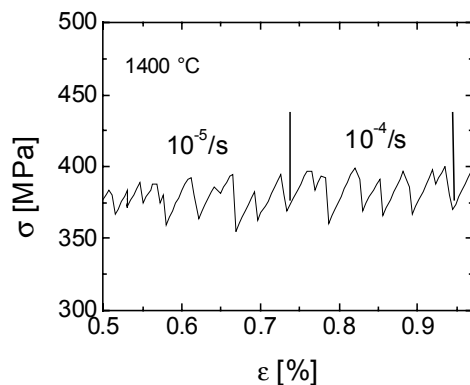
Fig. 5.3.5. The effect of the strain rate on the serrations in ZrO$_2$-20mol%Y$_2$O$_3$ deformed along $\langle 112 \rangle$ at 1400°C

lower border of the stability range is approached at 800 °C, the yield drop becomes more smooth (Fig. 5.3.4b). At an even lower temperature of 780°C (Fig. 5.3.4c), the deviation of the reloading curve from a straight line indicates that plastic deformation occurs during the reloading, too. The serrations are mainly controlled by the stress levels where the stress drop starts
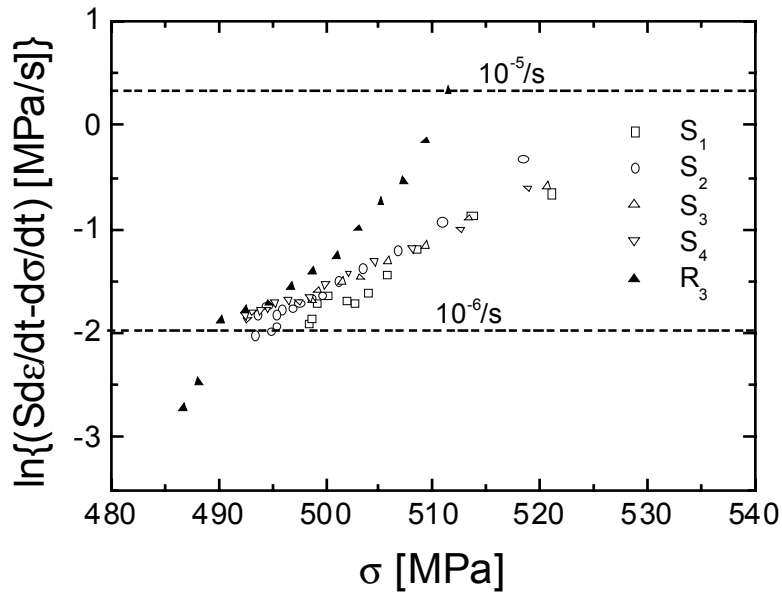
Fig. 5.3.6. Dynamic deformation behavior of the stress drops
of plastic instabilities in ZrO_2-15mol%Y_2O_3 deformed in
$\langle 112 \rangle$ in comparison with that during stress relaxation tests

and ends. As a consequence, the increase of strain during one serration, i.e. during one stress drop, is almost independent of the strain rate, as demonstrated by the strain rate change in Fig. 5.3.5. Besides, there is no change of the average stress level after changing the strain rate, i.e. the strain rate sensitivity obtained from a strain rate change experiment is close to zero (Fig. 5.2.6.).

The stress drop during a serration corresponds to plastic deformation under a decreasing stress. Apart from the superimposed (slow) drive rate of the testing machine, this situation is similar to that during a stress relaxation test. This is shown in Fig. 5.3.6. It compares the dynamic deformation behavior during the relaxation with that during the stress drops of the serrations.

On the ordinate, the quantity $\ln (S\dot{\varepsilon}_t - \dot{\sigma})$ is plotted. $\dot{\varepsilon}_t$ equals the imposed total strain rate of the machine during deformation and is zero during relaxation. With this quantity, both the drops during serrations and the relaxation curves can be plotted using one and the same scale. The figure presents, as open symbols, the data from the serrations of the part of the stress-strain curve at 10^{-6} s^{-1} of Fig. 5.3.2a shown with a

higher resolution in Fig. 5.3.4b (S_1 to S_4). The plot contains two horizontal dashed lines indicating the strain rates of 10^{-6} and 10^{-5} s^{-1}. While the imposed average strain rate during the serrated yielding was 10^{-6} s^{-1}, the plastic deformation rate during the stress drops was always higher than 10^{-6} s^{-1}. Since the serrations start occurring on the condition of almost elastic loading, they should correspond to repeated relaxations. The data of a stress relaxation test (R_3 in Fig. 5.3.2a), which occurred in the stable range at 10^{-5} s^{-1} after the unstable range had taken place, is plotted as full symbols. This relaxation is started out of the steady state deformation. Thus, the curves of serrations and of the relaxation test are related to each other in the same way as do the repeated relaxations and the original ones, e.g. in Fig. 5.1.4. taken from the material with 10mol% yttria. Repeated relaxations start at lower relaxation rates than primary relaxation curves, though both types of the curves tend to coincide at low relaxation rates. Similar curves are obtained for the 15 and 21mol% materials. Consequently, stress relaxation curves describe the dynamic deformation behavior during serrations
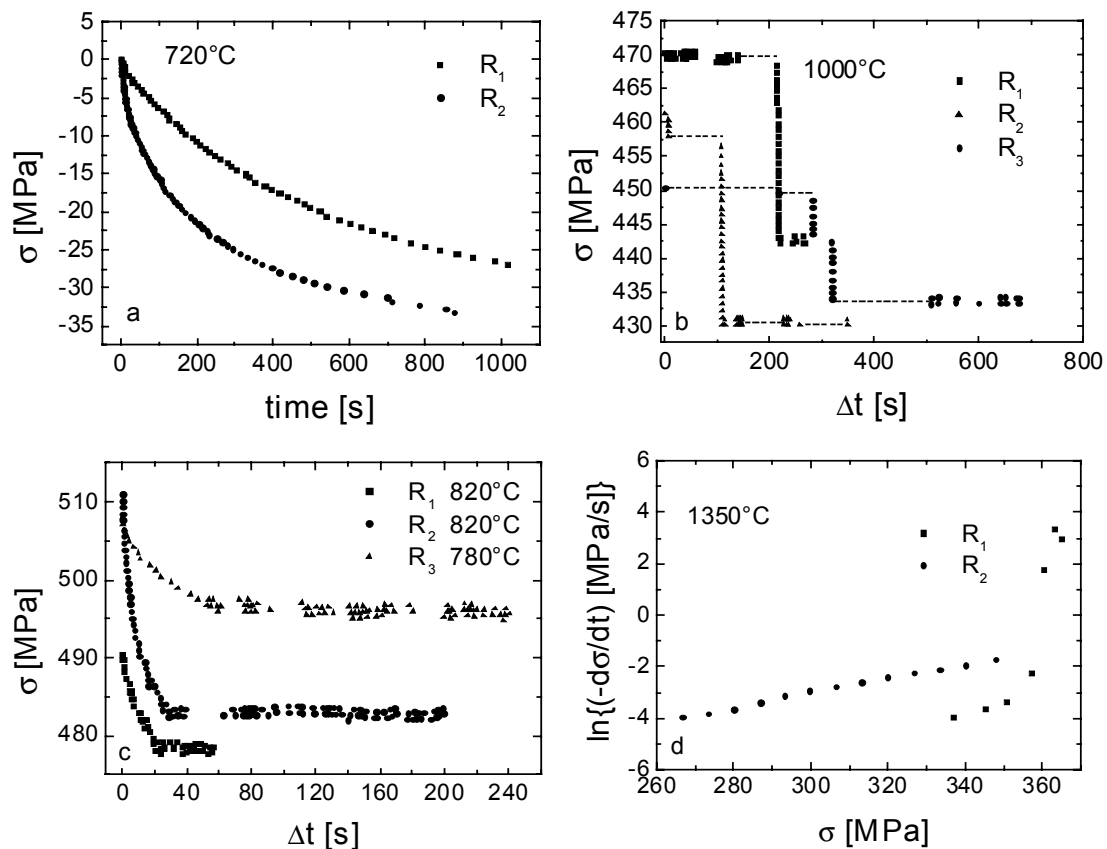
Fig. 5.3.7. The relaxation behavior of the stable deformation versus that of the instabilities in ZrO$_2$-15mol%Y$_2$O$_3$ deformed along $\langle 112 \rangle$.
a, d: stable deformation; b,c: instabilities

at low deformation rates. At the lower end of the relaxation curve, the relaxation rate falls down to very low values as will be discussed below. For the serrations, these low rates do not occur.

Because of the resemblance between the dynamic deformation behavior during the stress drops at serrated yielding and stress relaxation experiments, the latter can be used to study the dynamic deformation behavior in the instability range in more detail. Fig. 5.3.7 compares the relaxation behavior in the stable deformation range with that in the instability range at different temperatures.

At about 720°C, the deformation is stable and the stress versus time plots of the relaxations exhibit usual continuous smooth curves (Fig. 5.3.7a). In the instability range, relaxation tests should be started near the tips of the reloading curves. Frequently, the stress remains at the level of the stop of the deformation machine and decreases only after some incubation time passes (curves 1 and 3 in Fig. 5.3.7b). After the drop, the stress is constant again. Sometimes, further drops may occur (curves 1 and 3). The stress drops are presented at a higher time resolution in Fig. 5.3.7c. At first, the stress relaxes in the usual way. However, if a certain (low) relaxation rate is
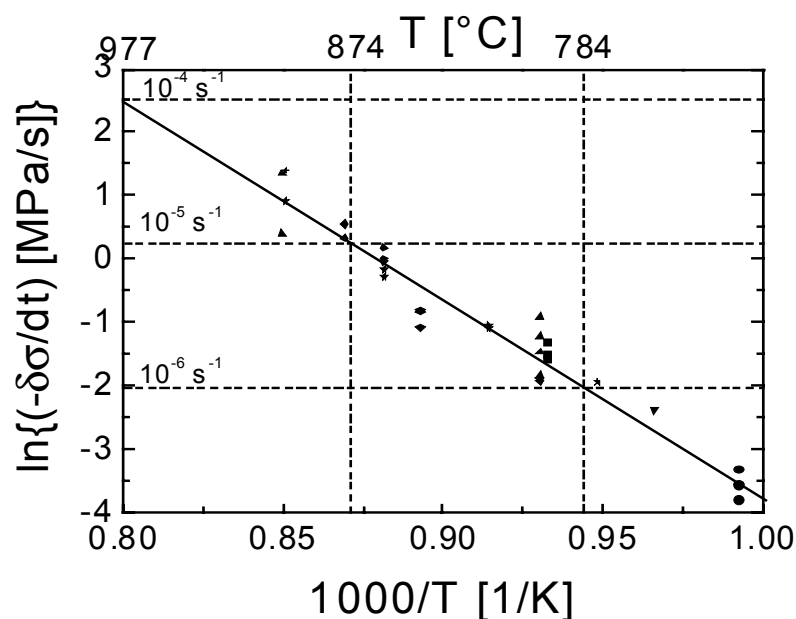
Fig. 5.3.8. Arrhenius plot of the minimum relaxation rates in ZrO_2-15mol%Y_2O_3 deformed in $\langle 112 \rangle$

reached, the stress versus time curves show a sharp knee. Then, the stress remains constant, i.e. the relaxation rate drops to zero. This stress level is only slightly below the lower stress level of the serrations. The zero relaxation rate is even observed at 780 °C, where the deformation is stable again. The observed behaviour indicates that the material deforms continuously only if the strain rate exceeds a defined minimum strain rate. Below it, the deformation is statically blocked. At high temperatures slightly below the upper border of the instability range, the relaxation rate does not decrease to zero, as shown in the relaxation curves of Fig. 5.3.7d. At these temperatures, the specimens relax to stress levels far below the lower level of the serrations. Fig. 5.3.8 exhibits an Arrhenius plot of the minimum relaxation rates. A straight line fits the data points relatively well. Its slope corresponds to an activation energy of about 2.7 eV.

Strain rates which correspond to relaxation rates above the solid line should allow unstable deformation. Strain rates corresponding to relaxation rates below the solid line are impossible for serrated flow to occur. The dashed horizontal lines mark experimental strain rates of 10^{-6}, 10^{-5} and 10^{-4} s^{-1}. These lines intersect the Arrhenius curve at the points corresponding to temperatures of 784°C, 874°C and 977°C. These temperatures agree well with the lower limits of the instability range in Fig. 5.3.3.

The processes which cause the locking of dislocations in the instability range may also lead to transient phenomena at other deformation conditions, e.g., at stress relaxation tests and the following reloading in the stable deformation ranges. As shown for the relaxation test R_1 in Fig. 5.3.2a and some relaxations in the 802°C section of Fig. 5.3.1, prominent yield drop effects appear during reloading after the relaxations at deformation conditions close to the lower border of the instability range. Within this range, the yield drop effects after changes of the deformation conditions are suppressed by the serrated flow. In conclusion, plastic instabilities occur if the strain rate drops below a temperature dependent minimum strain rate below which the deformation is statically blocked. The minimum rates obey an Arrhenius-type relation with the temperature with an activation energy of 2.7 eV.

6.   Microstructure of deformed cubic zirconia single crystals

In this chapter, the microstructures of some of the deformed ZrO_2 samples are presented. The microstructures were investigated by optical interference and birefringence microscopy as well as by transmission electron microscopy in the HVEM as described in Chapter 4.2. The Burgers-vectors were determined by taking micrographs of the same specimen area at different $\vec{g}$-vectors and using contrast extinctions according to $\vec{g} \cdot \vec{b} = 0$. That the slip planes engaged in dislocation glide could be identified, wide-tilting experiments in the transmission electron microscope were performed.

6.1. Optical microscopy of cubic zirconia

Fig. 6.1.1. demonstrates the stress-birefringence patterns of ZrO_2-10mol%Y_2O_3 deformed in the $\langle 100 \rangle$ compression direction at 1100°C, i.e. in the intermediate temperature range of low strain rate sensitivities.

a   b
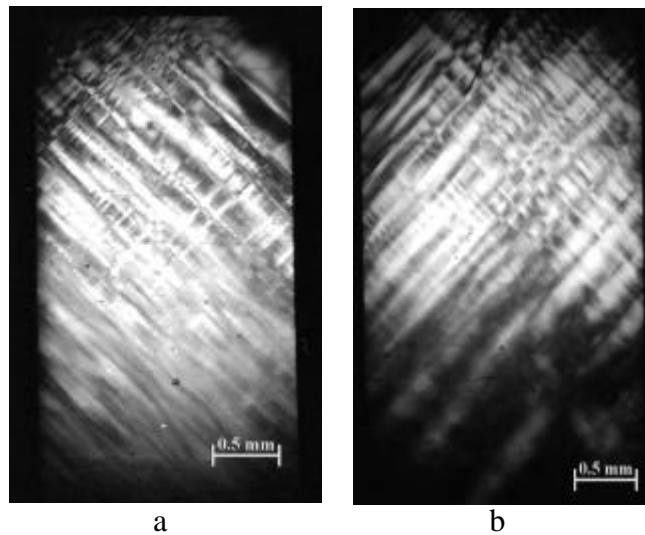
Fig. 6.1.1. Stress-birefringence patterns of ZrO_2-10mol%Y_2O_3
deformed along $\langle 100 \rangle$ at 1100°C with $\dot{e} = 10^{-5}$ s^{-1} till $e = 2.5\%$;
(010) and (001) observation planes, respectively

The images correspond to the (010) and (001) side faces. On both faces, well defined slip bands run in the $\langle 110 \rangle$ directions. Surface steps are only visible in $\langle 100 \rangle$

directions. This is consistent with the activation of slip on the four equivalent sets of planes of {110} type with non-zero orientation factor.

Fig. 6.1.2. displays the stress-birefringence patterns of the same material deformed in the same compression direction at 1400°C. Unlike intermediate temperatures, the slip
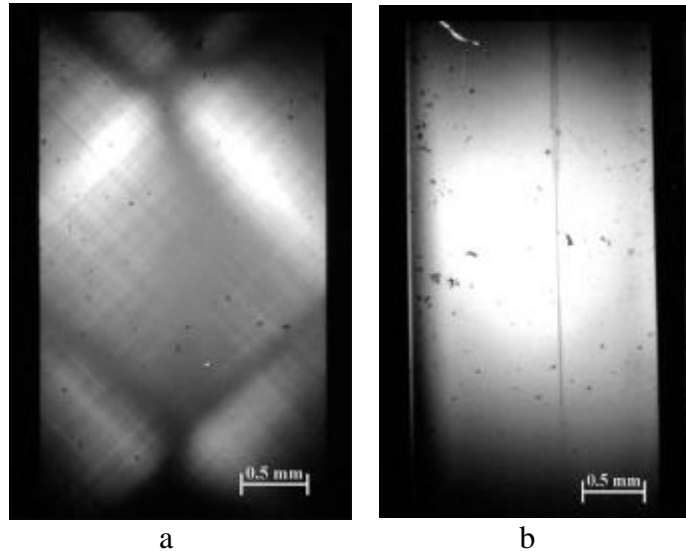
Fig. 6.1.2. Stress-birefringence patterns of ZrO_2-10mol%Y_2O_3 deformed along $\langle 100 \rangle$ at 1400°C with $\dot{e} = 10^{-5}\,s^{-1}$ till $e = 2.8\,\%$; (001) and (010) observation planes, respectively

bands are now much finer and more homogeneously distributed. In the particular case, slip is concentrated on two sets of orthogonal {110} planes, as no contrast appears on the face in Fig. 6.1.2b.

In the following, results are presented on the ZrO_2-15mol%Y_2O_3 material deformed in the $\langle 112 \rangle$ compression direction. At low temperatures in the range of stable deformation, only single Lüders bands develop near the ends of the sample. These bands grow to a remarkable width so that the specimens has a kinked shape. According to Fig. 6.1.3. taken from a specimen deformed at 1000°C, i.e. in the range of unstable deformation, slip is now localized in several narrow Lüders bands still at the ends of the compression sample. The orientation of the bands at an angle of about 54.74° with respect to the compression direction on the {110} face and of 90° on the {111} face corresponds to the easy slip system on {100} glide planes.

a   b
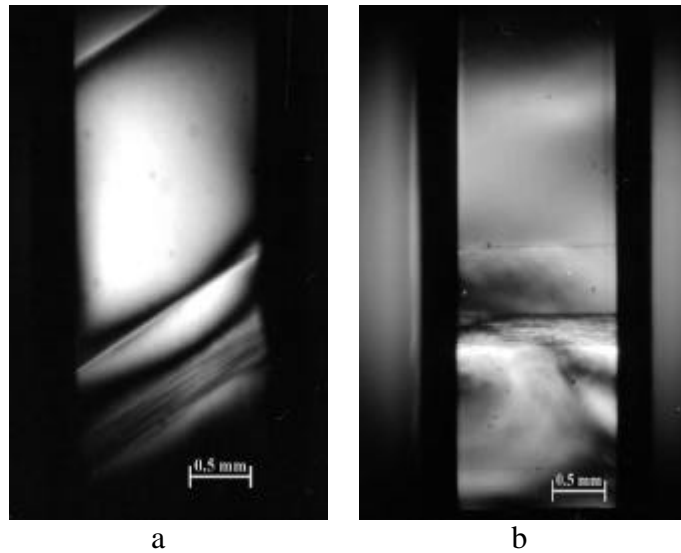
Fig. 6.1.3. Stress-birefringence patterns of ZrO_2-15mol%Y_2O_3
deformed in $\langle 112 \rangle$ at 1000°C with $\dot{e} = 10^{-5}\,s^{-1}$ till $e = 1.5\,\%$;
(110) and (111) observation planes, respectively

Fig. 6.1.4. displays the stress-birefringence patterns of the same material deformed at 1200°C.

a   b
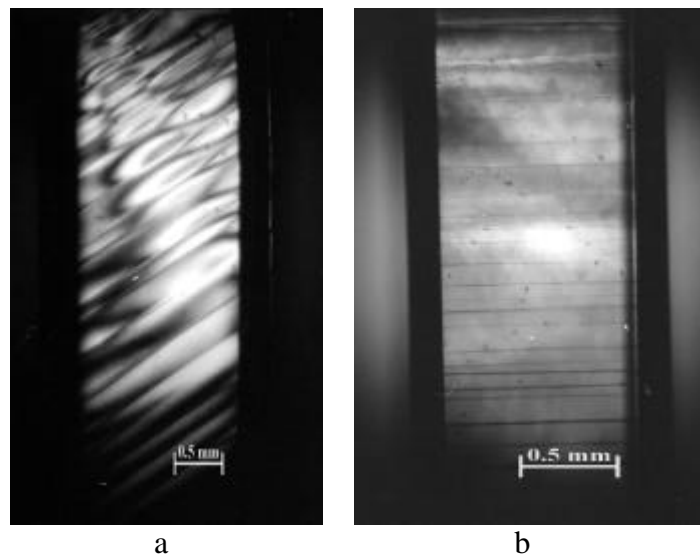
Fig. 6.1.4. Stress-birefringence patterns of ZrO_2-15mol%Y_2O_3
deformed in $\langle 112 \rangle$ at 1200°C with $\dot{e} = 10^{-5}\,s^{-1}$ till $e = 1.8\,\%$;
(110) and (111) observation planes, respectively

The dislocation bands on parallel {100} planes propagate now over the entire length of the sample. The distance between the Lüders bands decreases with increasing temperature so that the slip becomes quite homogeneous at 1400°C as shown in Fig. 6.1.5.

a   b
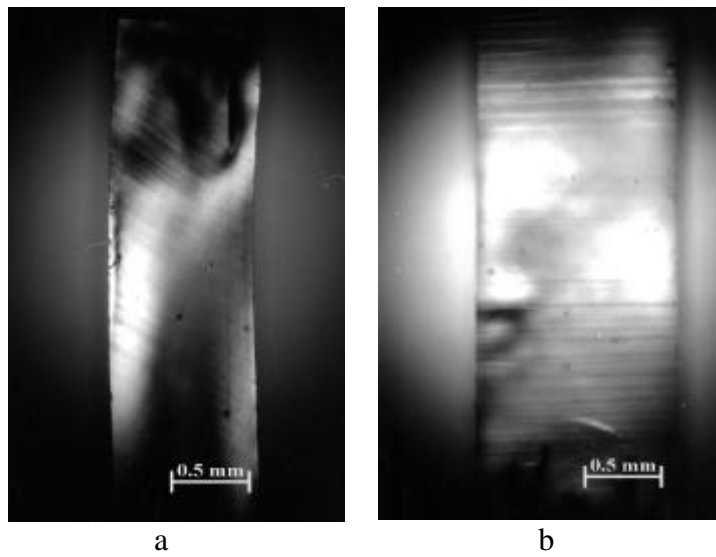
Fig. 6.1.5. Stress-birefringence patterns of ZrO_2-15mol%Y_2O_3 deformed in $\langle 112 \rangle$ at 1400°C with $\dot{e} = 10^{-5}$ s^{-1} till $e = 3.5\%$; (110) and (111) observation planes, respectively

6.2. Transmission electron microscopy in the HVEM

The following series of figures presents the dislocation structure of ZrO_2-10mol%Y_2O_3 crystals deformed along $\langle 100 \rangle$ at different temperatures. In the micrographs, the compression direction is indicated by the vector $\vec{d}$. All micrographs were taken near [001] poles perpendicular to the {001} side faces. It was tried to identify the activated slip planes by the following criteria. In the projection used, two sets of orthogonal slip planes run in $\langle 110 \rangle$ directions and are oriented edge-on. Dislocations on these planes should therefore be imaged as straight lines. The other two sets of orthogonal {110} planes intersect the specimen surface along the [010] direction and are inclined with respect to the surface by 45°, so that the dislocations may show their curved shape. {111} planes intersect the specimen surface always along $\langle 110 \rangle$ directions and are also inclined, so that the respective dislocations may show a curved shape, too. In addition, the directions of the Burgers vectors were used to back up the identification of the slip planes.

At low temperatures, slip is concentrated in slip bands, as shown by optical microscopy for the intermediate temperature range in Fig. 6.1.1. The following figures

show crystal regions within these bands. Fig. 6.2.1. is a micrograph of a sample deformed at 700°C.

6.2.1. Microstructure of ZrO_2-10mol%Y_2O_3 deformed along $\langle 100 \rangle$ at 700°C till $e = 1.3\%$, shown with the [020] $\vec{g}$ -vector at [001] pole

The Burgers vectors of the dislocations are 1/2[110] or 1/2[1$\bar{1}$0]. The straight dislocations in the lower part of the figure run parallel to these directions and belong therefore to {110} slip planes. The bowed-out dislocations in the upper part of the figure extend on {111} planes. The bowing of short dislocation segments results from pinning of the dislocations by localized obstacles.

Fig. 6.2.2. displays the dislocation structure of a sample deformed at 800°C. In Fig. 6.2.2.a., dislocations of all possible slip systems with non-zero orientation factors are imaged. In Fig. 6.2.2.b., a few dislocations of 1/2[101] or 1/2[$\bar{1}$01] Burgers vectors are extinguished. In Fig. 6.2.2.c., dislocations of 1/2[110] Burgers vectors and in Fig.
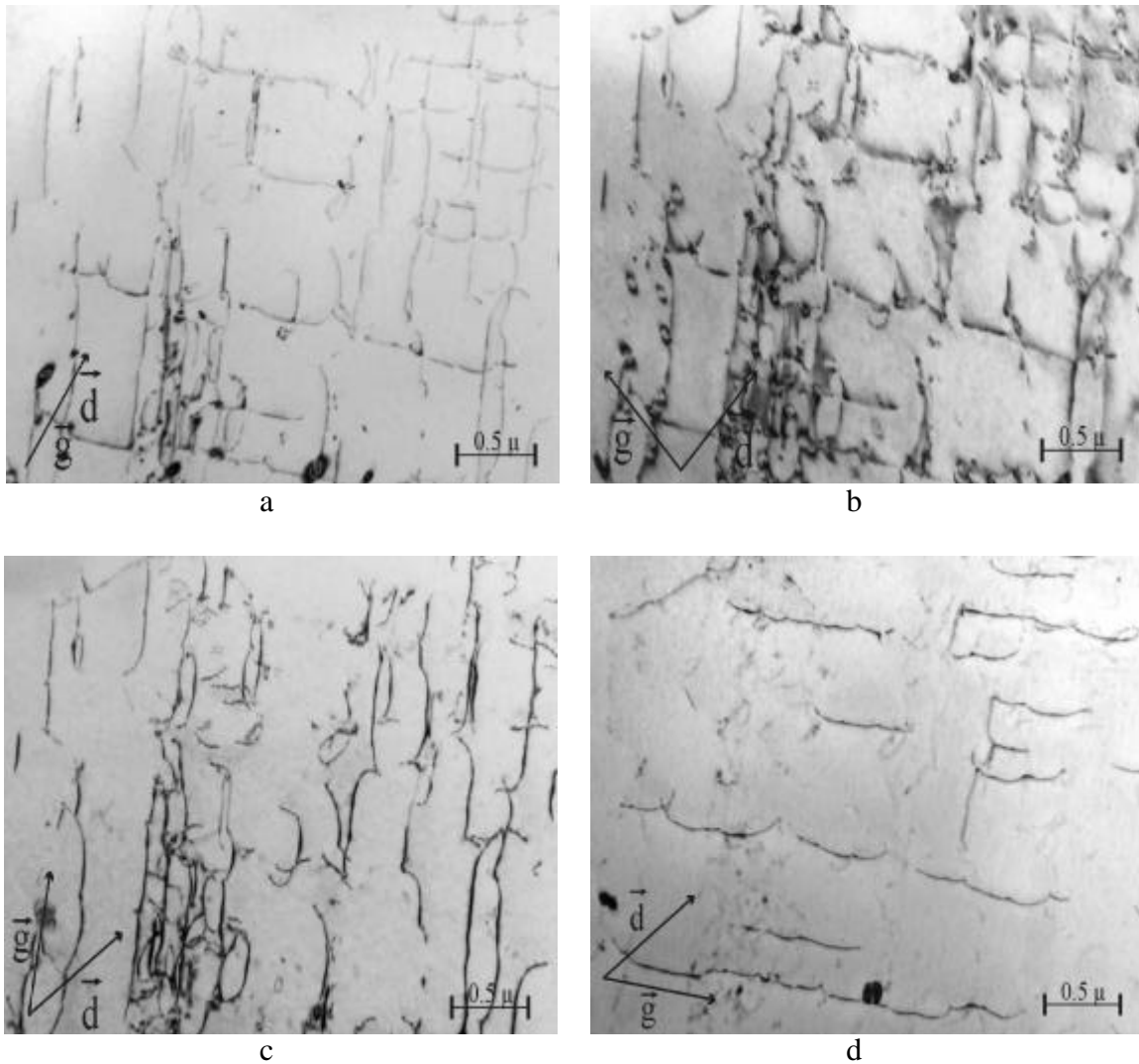
6.2.2. Microstructure of ZrO_2-10mol%Y_2O_3 deformed along $\langle 100 \rangle$ at 800°C till $e = 1.1\%$, shown with different diffraction vectors at the $[001]$ zone axis. a: $\vec{g} = [200]$, b: $\vec{g} = [020]$, c: $\vec{g} = [2\bar{2}0]$, d: $\vec{g} = [220]$.

6.2.2.d. those of 1/2[1$\bar{1}$0] Burgers vectors are not visible. These dislocations belong to {111} slip planes rather than to {110} ones. The angle between the {111} slip planes and {001} observation plane is 54.74°. If the dislocations belonged to {110} slip planes, they would appear as straight lines at the [001] zone axis, which they do not do. The dislocations have the bowed-out shape again.

Fig. 6.2.3. displays the microstructure of a specimen deformed at 900°C. In this figure, dislocations are located in two bands, separated by a region of a lower dislocation density. Since many dislocations are straight and oriented parallel to the
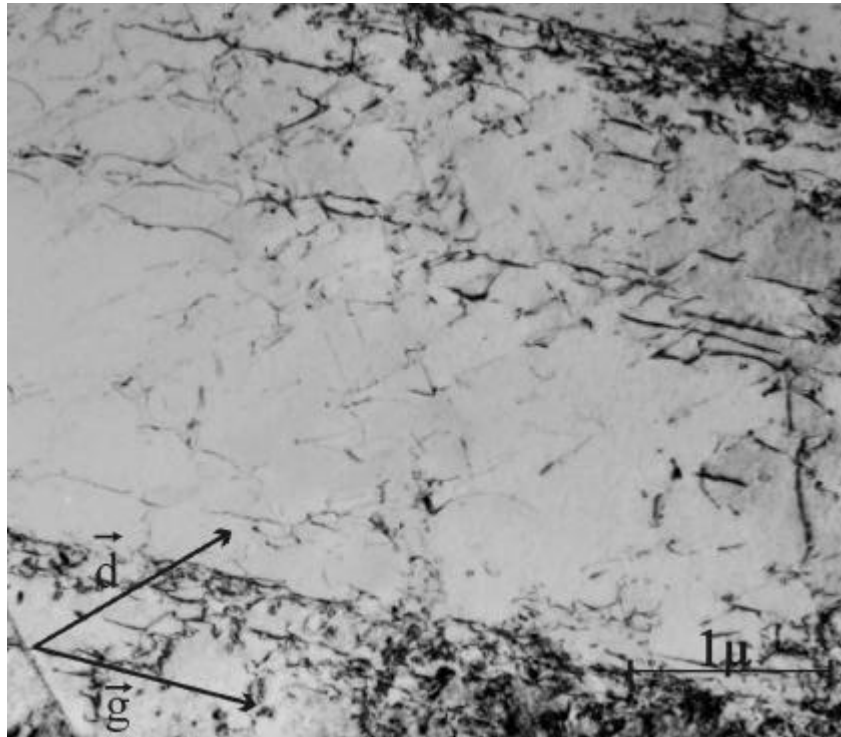
Fig. 6.2.3. Dislocation structure of ZrO_2-10mol%Y_2O_3
deformed along $\langle 100 \rangle$ at 900°C till $e = 2.2\%$, shown with
the $[220]$ $\vec{g}$-vector at $[001]$ zone axis

direction of the diffraction vector $[2\bar{2}0]$, they should belong to the $(110)1/2[1\bar{1}0]$ slip
system. Besides, there is a number of curved dislocations that are randomly oriented.
In accordance with the Burgers vector analysis, these glide on the {101} planes.

a

b
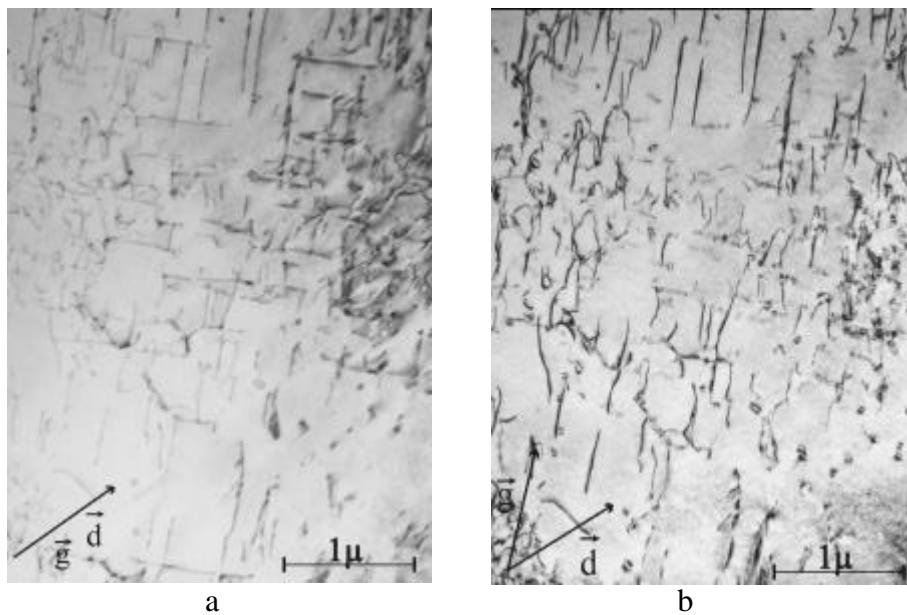
6.2.4. The microstructure of ZrO_2-10mol%Y_2O_3 deformed along $\langle 100 \rangle$ at 1050°C
till $e = 2.1\%$, shown with two different diffraction vectors with the $[100]$ pole. a:
$\vec{g} = [200]$, b: $\vec{g} = [2\bar{2}0]$.

Fig. 6.2.4. presents the dislocation structure of the sample deformed at 1050°C. With the $\vec{g}$ vector in Fig. 6.2.4.a, all dislocations of slip systems with non-zero orientation factors are visible. Many of the dislocations have 1/2[110] or 1/2[1$\bar{1}$0] Burgers vectors as shown for the latter set in Fig. 6.2.4b. Since they are quite straight, slip occurs on {110} planes rather than on {111} planes. Some dislocations are curved, too.

Fig. 6.2.5. of the specimens deformed at the high temperatures of 1300°C (a) and 1400°C (b) were taken with a $\vec{g}$ vector showing all relevant dislocations. Using the above criteria, the dislocations may belong again to both {111} and {110} slip planes. It is characteristic of the high temperatures that the dislocations are distributed homogeneously, in contrast to low and intermediate temperatures. Besides, the dislocations do not bow out between localized obstacles anymore.

| a | b |
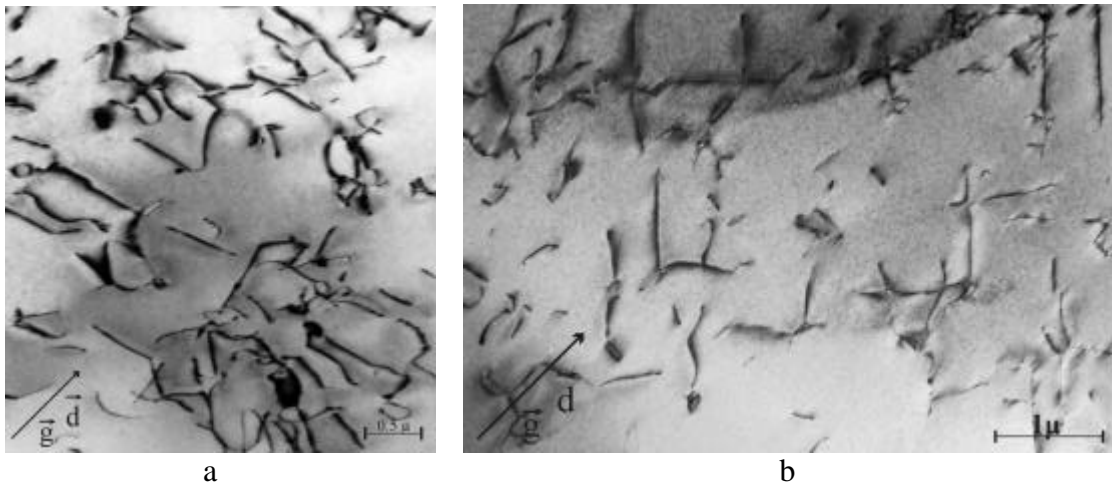
6.2.5. The microstructure of ZrO_2-10mol%Y_2O_3 deformed along $\langle 100 \rangle$ at 1300°C and 1400°C till $e = 2.8\%$, shown with $\vec{g} = [200]$

Summarizing the qualitative observations, it may be stated that both {110} and {111} slip planes are activated at all temperatures during deformation along $\langle 100 \rangle$, where the easy slip systems with {100} planes are out of stress. Slip is localized at low temperatures and becomes homogeneous at high temperatures. At low temperatures, the dislocations bow out between localized obstacles. This mechanism ceases above about 1050°C.
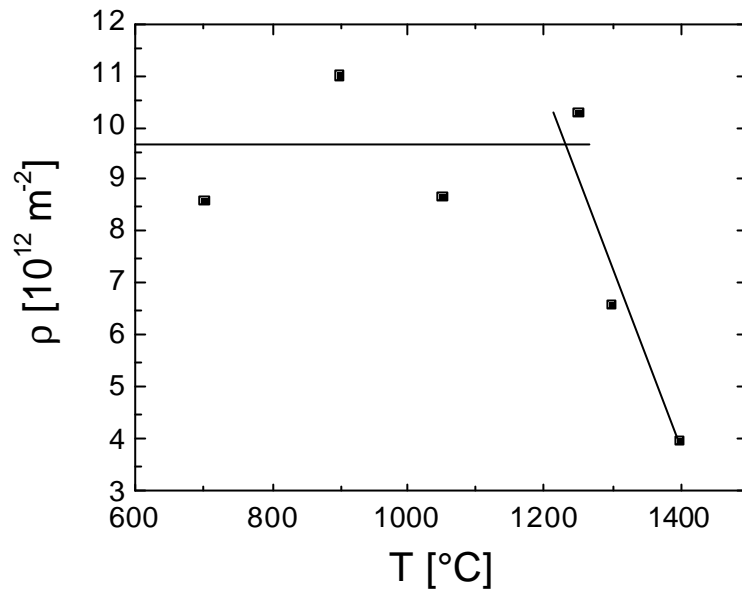
Fig. 6.2.6. Dislocation density of ZrO_2-10mol%Y_2O_3 deformed in $\langle 100 \rangle$ as a function of temperature

In order to obtain quantitative data from the microstructure, the dislocation density ρ was measured from about four selected micrographs for each temperature by counting the numbers of intersections of the dislocation lines N_1 and N_2 with two orthogonal grids of straight lines of lengths P_1 and P_2 according to $\rho = (N_1/P_1 + N_2/P_2)/t$. The specimen thickness t was estimated from the projected length of dislocations crossing the specimen on a known slip plane. As demonstrated by Fig. 6.2.6, the dislocation
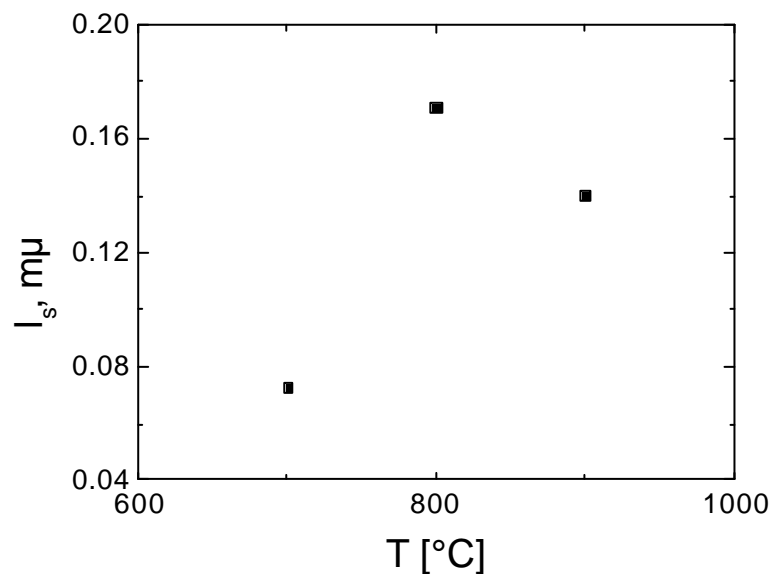
Fig. 6.2.7. Dislocation segment length of ZrO_2-10mol%Y_2O_3 deformed in $\langle 100 \rangle$ as a function of temperature

density is constant up to 1250°C and decreases rapidly above this temperature.

Furthermore, the average length of bowed-out dislocation segments was determined at different temperatures. For this, micrographs were selected showing dislocations with easily visible cusps at obstacles along their lines like Fig. 6.2.2. The cusps at the obstacles are marked by either a reduced or an increased electron microscopy contrast. The average segment length was taken as evaluated dislocation line length l_d per number of cusps m: $l_s = l_d / m$. The segment length increases from about 70 nm at 700°C to 150 nm at 800°C to 900°C (Fig. 6.2.7.). At high temperatures, the dislocations are not pinned anymore, as stated above.

A few micrographs were also taken from a ZrO_2-15mol%Y_2O_3 crystal deformed along $\langle 112 \rangle$ at 1200°C. Fig. 6.2.8 gives such an example. Dislocations on the {100} easy slip plane are imaged edge-on and appear in very narrow slip bands indicating planar slip. The broader band contains dislocations that belong to the {111} slip planes.
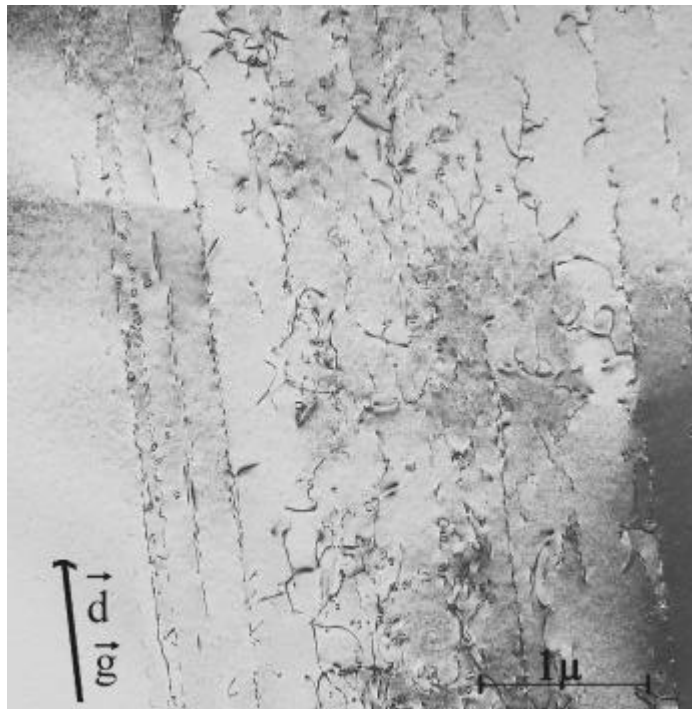
6.2.8. The microstructure of ZrO_2-15mol%Y_2O_3 deformed along $\langle 100 \rangle$ at 1400°C till $e = 1.8\%$, shown with $\vec{g} = [200]$

7.   Discussion of the experimental results

7.1. Introduction

In this chapter, the results of the compression experiments on cubic zirconia single crystals of chapter 5 will be discussed on the basis of the cubic zirconia microstructure presented in chapter 6. In this doctoral thesis, the data on the dislocation structure are available mainly for ZrO_2-10mol%Y_2O_3 deformed in the $\langle 100 \rangle$ compression axis.

In previous works of other working groups, the plastic deformation of cubic zirconia single crystals was mostly studied in compression along $\langle 112 \rangle$ where dislocations with $1/2\langle 110 \rangle$ Burgers vectors were activated on the soft {100} cube planes [10 to 14]. Apart from the experiments between 350°C and 500°C under a confining pressure [78], most of the research was done near 1400°C or even higher temperatures. The deformation in the $\langle 100 \rangle$ compression direction, where the easy slip systems are not activated, was not thoroughly studied before. A few attempts are shortly mentioned in chapter 3.2. of this doctoral thesis.

However, the results of the present experiments performed in the scope of this dissertation can be compared with the results of the 10mol% material deformed in the $\langle 112 \rangle$ soft orientation. The latter were obtained during earlier studies of the plasticity group at the MPI of Microstructure Physics [e.g. 4, 19, 21, 26, 46, 47, 90], so that these data are treated as reference data, as already done in the preceding text. According to them, dislocation models were proposed for the different temperature ranges for the deformation of ZrO_2-10mol%Y_2O_3 along $\langle 112 \rangle$. These were the lattice friction (Peierls mechanism) with a low value of the activation volume of about 2 b^3 at temperatures below 600°C, where b is the absolute value of the Burgers vector, localized obstacles and jogs from 600°C to 1000°C with increasing values of the activation volume, athermal deformation between 1000°C and 1200°C with very high activation volumes, and recovery at higher temperatures.

According to the elastic theory of interactions between moving dislocations and other dislocations, as well as with other crystal defects, the interaction forces are, in the framework of isotropic elasticity theory, proportional to the shear modulus (e.g. [39, 40, 44]). As the shear modulus weakly depends on the temperature, it is useful to normalize the flow stress with respect to the shear modulus in order to separate its influence on the temperature dependence of the flow stress from other temperature-dependent processes like the thermally activated overcoming of obstacles. In order to consider the elastically anisotropic nature of zirconia, the energy factor K_s of screw dislocations of $1/2\langle 110 \rangle$ Burgers vectors calculated by anisotropic elasticity theory is used instead of the shear modulus. The K factors substitute the shear modulus in most formulae of interaction forces and energies. The values of K_s are equal for the {100} and {111} slip planes in ZrO_2. They were calculated in [4] using the formulae presented in [44]. The elastic constants were taken from [71]. Since the K_s values in [4] were available only for several fixed temperatures, these were extrapolated to the temperatures, at which the compression experiments were done in this work.

The calculated values of the normalized flow stresses σ/K_s are presented in Fig. 7.1.1. Only the flow stresses of cubic zirconia stabilized with 10mol% yttria alter with
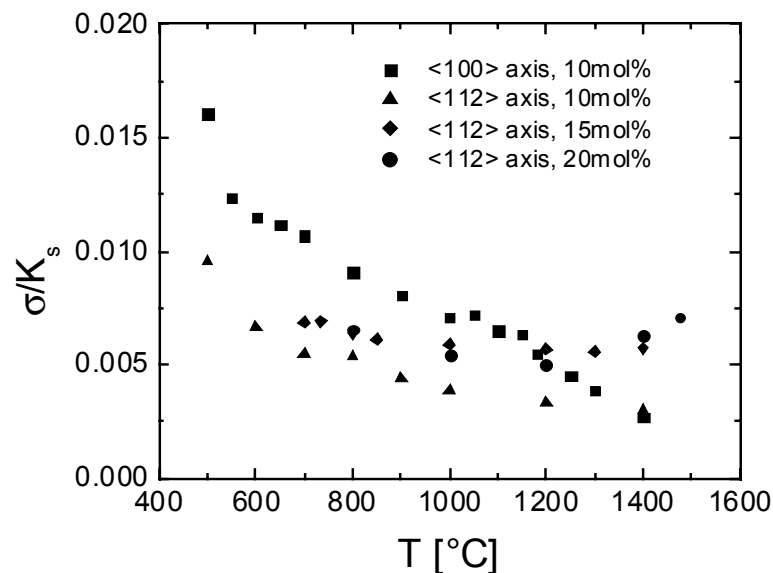
Fig. 7.1.1. The dimensionless stress σ/K_s of cubic zirconia (screw dislocations) stabilized with different contents of yttria and deformed along $\langle 100 \rangle$ and $\langle 112 \rangle$ versus temperature

changing temperature in both orientations of the compression axis. The curve for the ⟨112⟩ orientation shows a very weak dependence above about 1000°C. The flow stresses of the 15 and 20mol% materials are almost independent of the temperature within the experimental accuracy of the data.

As outlined above, the flow stress of cubic zirconia single crystals consists of several components, each of which dominates within a corresponding temperature range, and each of which contributes to the flow stress in a different way. In the following, it will be attempted to estimate these diverse contributions for the material stabilized with 10mol% yttria deformed in the ⟨100⟩ compression direction, since most of the microstructural data are available for these deformation conditions. Afterwards, the influence of the different yttria contents will be discussed, in particular with respect to the plastic instabilities.

7.2.   Flow stress contributions for ZrO$_2$-10mol%Y$_2$O$_3$: Comparison between deformation along the ⟨100⟩ and ⟨112⟩ compression directions

As shown in chapter 5.1. and in Fig. 7.1.1., the flow stresses of ZrO$_2$-10mol%Y$_2$O$_3$ deformed in the ⟨100⟩ and ⟨112⟩ compression axes exhibit different dependencies on the temperature. The flow stress along ⟨100⟩ is mostly higher than that along ⟨112⟩. Both flow stresses are equal only at 1400°C. The differences should be related to the different glide planes activated. At high temperatures, recovery controls the deformation, so that the shear stresses along both orientations become the same.

As described above several times, slip on the easy {100} planes is activated during deformation along ⟨112⟩. As to the microstructure of ZrO$_2$-10mol%Y$_2$O$_3$ deformed in the ⟨100⟩ compression axis, the stress-birefringence observations of chapter 6.1. are most consistent with the slip on {110} planes, while the transmission electron microscopy studies of chapter 6.2. showed dislocations arranged on {111} and {110} planes at the same time, the former type prevailing. It may therefore be assumed that slip on both types of the planes is simultaneously active. This is in contrast to the result in [19], where slip was observed only on {110} planes during deformation

along $\langle 100 \rangle$ at 1400°C. The present experiments refer mostly to lower temperatures. Thus, the {111} planes may become active at lower temperatures.

In the following, the athermal component of the flow stress τ_i is considered. It results from long-range interactions between parallel dislocations τ_p (Taylor hardening) and the back stress of bowed-out dislocation segments τ_b

$$\tau_i = \tau_p + \tau_b \qquad (7.2.1)$$

The calculation of τ_p is based on eq. (2.2.20). The shear modulus μ is replaced by the energy factor K$_s$, so that eq. (2.2.20) reads now [20]

$$\tau_p = \alpha \mathrm{Kbf}_{pm} \rho^{1/2} / 2\pi \qquad (7.2.2)$$

α is a dimensionless factor of about 8 and f$_{pm}$ a dimensionless maximum interaction force between two parallel dislocations on parallel slip planes. Since the factors K$_s$ and the f$_{pm}$ values were available only for {100} and {111} slip planes, the current calculations were hence done for {100} planes for the $\langle 112 \rangle$ compression direction and for {111} planes for the $\langle 100 \rangle$ direction in cubic zirconia single crystals. The interaction forces f$_{pm}$ amount to 0.3 for the {100} planes and to 0.66 for the {111} planes [4, 17]. The dislocation densities were taken from Fig. 6.2.6 of chapter 6.2. of this doctoral thesis. Accordingly, Fig. 7.2.1. presents the respective Taylor
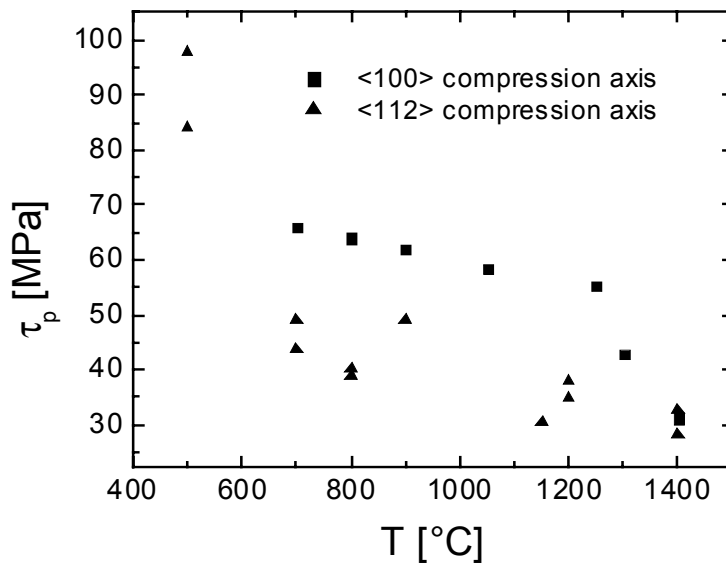
7.2.1. The Taylor hardening contribution τ_p of the athermal component of flow stress τ_i of ZrO$_2$-10mol%Y$_2$O$_3$ deformed along $\langle 100 \rangle$ and $\langle 112 \rangle$ versus temperature

components τ_p of the flow stress. In this thesis, all stresses calculated theoretically are expressed as shear stresses τ. To compare them with the experimentally obtained engineering stresses $\sigma = \tau/m_s$, the orientation factor m_s has to be taken into account.

In the $\langle 100 \rangle$ orientation, τ_p slowly decreases from about 65 MPa between 700°C and 1250°C, but then abruptly falls down to 30 MPa at 1400°C. The rapid decrease originates from the decrease in the dislocation density, which in turn should result from recovery at high temperatures. The Taylor component of the flow stress along $\langle 112 \rangle$ decreases rapidly at low temperatures but gradually above about 700°C. The highest values along $\langle 100 \rangle$ result form the higher value of f_{pm} on $\{111\}$ planes.

The total athermal component of the flow stress τ_i also contains the back stress τ_b from the bowing of dislocation segments. The back stress can be calculated from the line tension of the dislocations and the equilibrium radius of curvature of dislocation segments under stress. The latter can only be measured by in-situ straining experiments in an electron microscope. For deformation along $\langle 112 \rangle$, τ_b was found to be of the same order of magnitude as τ_p [90, 17]. Since in-situ experiments were not carried out in the scope of this doctoral dissertation, the back stress of dislocations could not be calculated. Thus, Fig. 7.2.1. represents a lower limit of the athermal stress τ_i. Considering the orientation factor $m_s = 0.41$ for the $\{111\}$ planes, the athermal stress components may be in the range of one fourth to one half of the total flow stress at, e.g. 900°C. Hence, other components have to contribute to the flow stress, in agreement with the strong temperature dependence of the latter.

In order to estimate the thermal part of the flow stress, the activation parameters of deformation shall be discussed in more detail. Fig. 7.2.2. shows the logarithm of the activation volume calculated by eq. (2.1.15) from the strain rate sensitivity r of the compression experiments whose results are shown in Figs. 5.1.5. and 5.2.6. The orientation factors mentioned above were taken into consideration. The data for ZrO_2-10mol%Y_2O_3 deformed in the $\langle 112 \rangle$ compression direction were taken from [4]. According to the plot, the activation volumes of the four materials behave in a similar way. Starting with small values at low temperatures, ΔV increases upwards until the temperature of about 1000°C, where it begins to decrease with a further rise of the
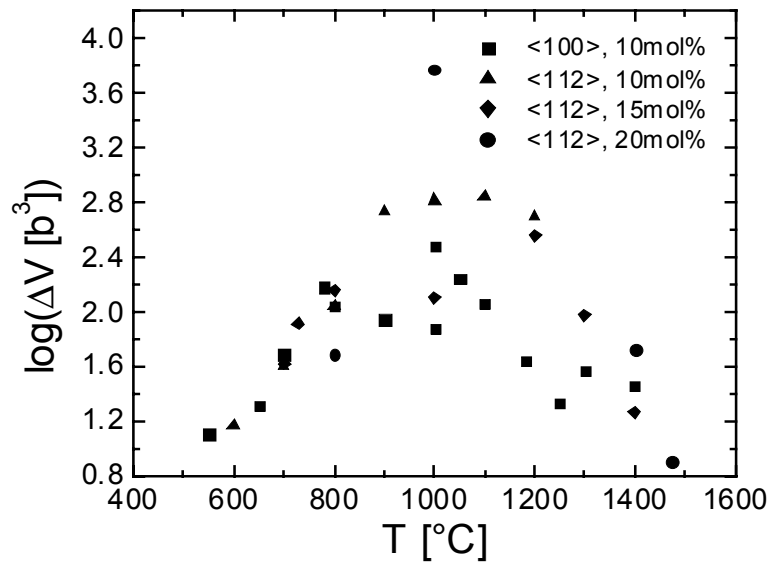
7.2.2. The logarithm of the activation volume ΔV of cubic zirconia single crystals stabilized with different contents of yttria and deformed in two different axes versus

temperature. Up to about 1000°C, the activation volumes of ZrO_2-10mol%Y_2O_3 are equal for both orientations. They are well consistent with the model of overcoming localized obstacles as discussed in [21, 46, 17] for the $\langle 112 \rangle$ orientation. This model is propped up by the shape of dislocations, e.g., in Figs. 6.2.1. and 6.2.2., where dislocations bow out between pinning centers. With the help of the formula 2.1.12., the activation distance $\Delta x = 3\Delta V/2lb$ can be estimated, where l is again the obstacle distance along the dislocation line whose magnitude is taken from Fig. 6.2.7. The factor of 3/2 is included in order to consider the Friedel statistics of the overcoming of localized obstacles [52, 40]. The result is an activation distance of the order of magnitude of 0.5 b. Similar relations between the activation volume and the segment length are observed also in other materials showing bowed-out dislocation segments (e.g. [91]).

The activation enthalpies of deformation ΔH were calculated from the temperature sensitivities in Figs. 5.1.3. and 5.2.4. and the strain rate sensitivities in Figs. 5.1.5. and
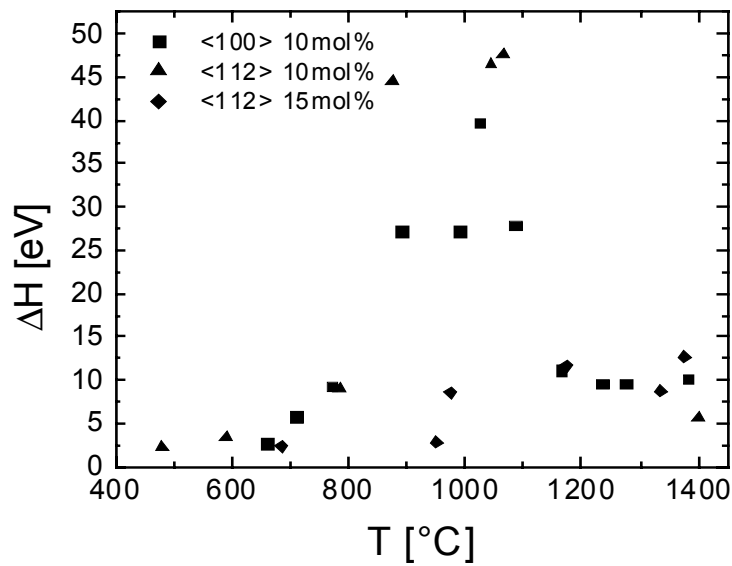
Fig. 7.2.3. The activation enthalpy of cubic zirconia stabilized with different concentrations of yttria and deformed along ⟨100⟩ and ⟨112⟩

5.2.6 using eq. (2.1.16). For the 10mol% material deformed in the two orientations, the activation enthalpies display very similar values in the whole temperature range. From 600°C up to 1000°C, they increase from 3-6 eV up to 40-50 eV and then decrease again to values below 10 eV (Fig. 7.2.3.).
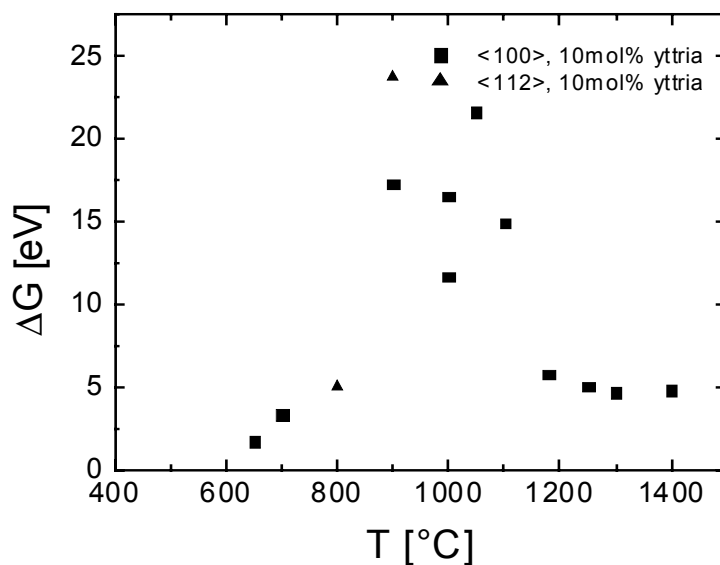
Fig. 7.2.4. Gibbs free energy of activation for ZrO₂-10mol%Y₂O₃ as a function of temperature

For a complete discussion of the thermally activated processes of deformation, the Gibbs free energy of deformation ΔG in the Arrhenius equation (2.1.7) has to be calculated. This is done by eq. (2.1.17), where the shear modulus is again replaced by K$_s$. The result is presented in Fig. 7.2.4. As expected, ΔG is lower than ΔH.

In order to calculate the total activation energy ΔF to overcome the obstacles, the work term ΔW from eq. (2.1.9) has to be estimated, too. First, the effective shear stress τ^* will be determined. It is given by the formula (2.2.1) as the difference between the applied (resolved) shear stress τ and the athermal component of the flow stress described above and presented in Fig. 7.2.1. The applied shear stress τ is described by the equation 2.1.2 as the product of the flow stress and the orientation factor of the activated glide planes.

Fig. 7.2.5. demonstrates the dependence of the effective stress τ^* on the temperature. Since the back stress τ_b is not considered, these data are the upper limits of τ^*. The effective stresses of ZrO$_2$-10mol%Y$_2$O$_3$ deformed along ⟨100⟩ and ⟨112⟩ are equally low at 1300-1400°C, but start increasing and differing with decreasing temperature in accordance with different processes controlling the dislocation mobility on the different slip planes.
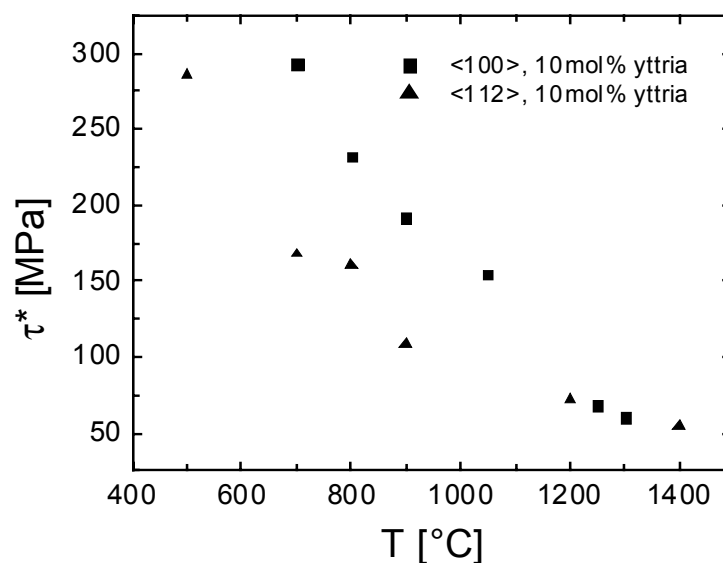
7.2.5. The effective stress of ZrO$_2$-10mol%Y$_2$O$_3$ deformed along ⟨100⟩ and ⟨112⟩
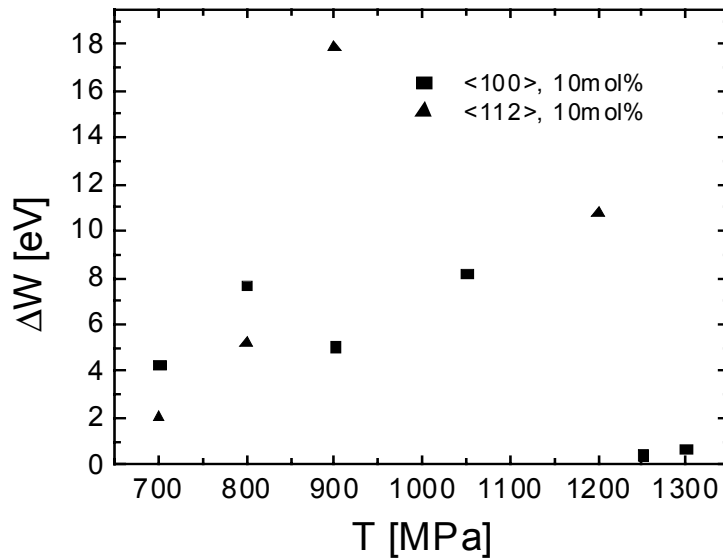
Fig. 7.2.6. The work term of ZrO_2-10mol%Y_2O_3 deformed in ⟨100⟩ and ⟨112⟩ compression directions

Fig. 7.2.6. displays the calculated work term ΔW. The work terms of deformation along the two orientations show a similar temperature dependence. They are small only at high temperatures.

Finally, the Gibbs free energy and the work term can be added to yield the Helmholtz
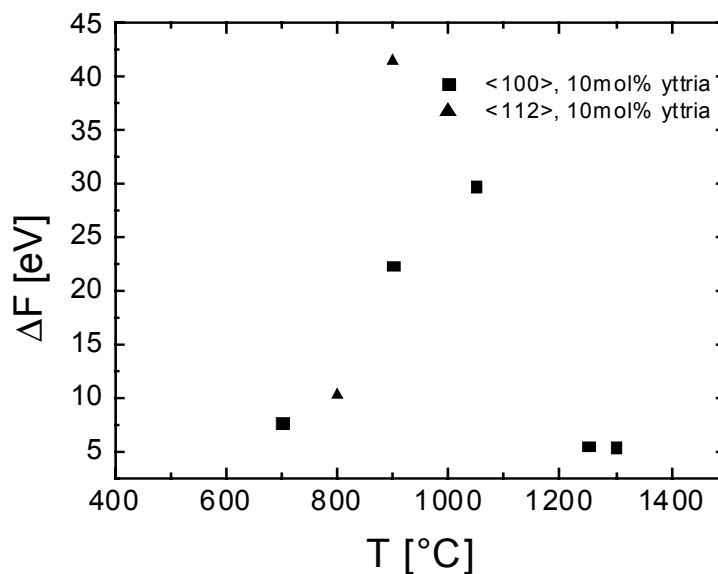
Fig. 7.2.7. Helmholtz free energy of activation for ZrO_2-10mol%Y_2O_3 as a function of temperature

free energy ΔF of activation plotted in Fig. 7.2.7. It is about 7.7 eV at 700°C. This value characterizes the obstacles which pin the dislocations as very strong ones.

The discussion has shown that below about 1050°C the thermal part of the flow stress of ZrO_2-10mol%Y_2O_3 can well be described by the strong localized obstacles visible by the bowed-out shape of dislocations in the electron micrographs like Figs. 6.2.1. and 6.2.2. The curly shape of dislocations disappears above about 1050°C. The nature of the obstacles is not clear. It is argued in [46] that some of them are jogs but most are small precipitates containing nitrogen, based on the observations in [79]. In conclusion, localized obstacles play an important role in the deformation along both orientations ⟨100⟩ and ⟨112⟩. However, for deformation along ⟨100⟩ this interaction seems to prevail up to higher temperatures than for ⟨112⟩. This difference may explain the higher flow stress along ⟨100⟩ as well as its non-vanishing temperature sensitivity.

A suitable explanation of the differences between deformation along ⟨100⟩ and ⟨112⟩ would also be the occurrence of different lattice friction stresses (Peierls stresses) on the different slip planes. Using formula (2.2.2), the Peierls stresses at zero temperature were estimated for screw dislocations on the {100}, {110} and {111} slip planes. The relevant planes should be {400}, {220} and {222}. Only the exponential factor of the formula was considered in order to distinguish between the stresses on the three planes. The results of the calculations are displayed in the following table.

Slip plane	Interplanar distance a, nm	Ratio a/b	Exponential factor $\exp(-2\pi a/b)$, screw dislocations
{400}	0.129	0.354	0.108
{220}	0.182	0.5	$4.32*10^{-2}$
{222}	0.149	0.409	$7.65*10^{-2}$

Hence, the Peierls stress at absolute zero temperature should be the highest for {100} slip planes, which contradicts the experimental observation that these planes are the easy planes. Since this model does not consider the ionic character of bonds in zirconia, it does not produce congruent data. Unfortunately, atomistic calculations of the Peierls stress at zero temperature are not available, yet. The Peierls stress at a

finite temperature is described by eqs. (2.2.4) to (2.2.8). It is shown in [46, 47] that the low temperature increase of the flow stress and particularly the strong rise of the strain rate sensitivity at about 500°C for compression along ⟨112⟩ can well be explained by a superposition of the mechanisms of localized obstacles and the Peierls mechanism, where the latter dominates at low temperature. For deformation along ⟨100⟩, the crystals are brittle below 500°C. At 550°C, the activation volume in Fig. 7.2.2. is about 15 b^3, which is consistent with the Peierls mechanism. Besides, the flow stress in Fig. 5.1.2 shows the same strong increase below 600°C for both deformation orientations. It may therefore be concluded that the Peierls stress acts also on non-cube slip planes below about 600°C, but is apparently negligibly small at higher temperatures.

In the temperature range between about 800°C and 1200°C, both the activation volumes and the activation energies become large. For deformation along ⟨112⟩, where the activation volume is particularly large, this was explained by only athermal processes controlling the flow stress. For the ⟨110⟩ orientation, the contribution of Taylor hardening to the flow stress in Fig. 7.2.1. is larger than for ⟨112⟩, which may indicate that a part of the flow stress difference between both orientations is due to different athermal contributions, in addition to the preservation of the contribution due to the overcoming of localized obstacles up to higher temperatures. The activation volume of about 300 b^3 for the ⟨100⟩ orientation is well in the range for localized obstacles. The large value of the activation energies cannot be explained at present.

As to the ZrO$_2$-10mol%Y$_2$O$_3$ deformed in the ⟨100⟩ compression axis, there is an interesting peculiarity at 1000°C. The stress relaxation curves of Fig. 5.1.4.c show an inverse curvature, thus consisting of two parts, a steep one at the beginning and a flat one at lower relaxation rates, each of which can be characterized by its own value of the strain rate sensitivity of the flow stress in Fig. 5.1.4. The steep part with a small strain rate sensitivity and a large activation volume of about 250 b^3 (Fig. 7.2.2.) corresponds to the processes controlling the dislocation mobility, i.e. the overcoming of localized obstacles. The large value of the strain rate sensitivity indicates the onset of recovery, which will dominate at higher temperatures.

Above 1250°C, the dislocation density decreases rapidly and the athermal component of the flow stress does the same, too. At 1400°C, both the total flow stresses in Fig. 5.1.2. and their Taylor components in Fig. 7.2.1. are the same for the ⟨100⟩ and ⟨112⟩ compression axes. At high temperatures, the deformation along ⟨112⟩ is strongly influenced by recovery [26, 19, 17], which is also true for deformation along ⟨100⟩. In this case, it is appropriate to express the strain rate sensitivity in terms of the stress exponent m* defined by the eq. (2.3.5). It can be calculated from the strain rate sensitivity r by

$$m^* = \sigma/r \qquad\qquad (7.2.3)$$

The results are presented in Fig. 7.2.8. From 1200°C up to 1400°C, the stress
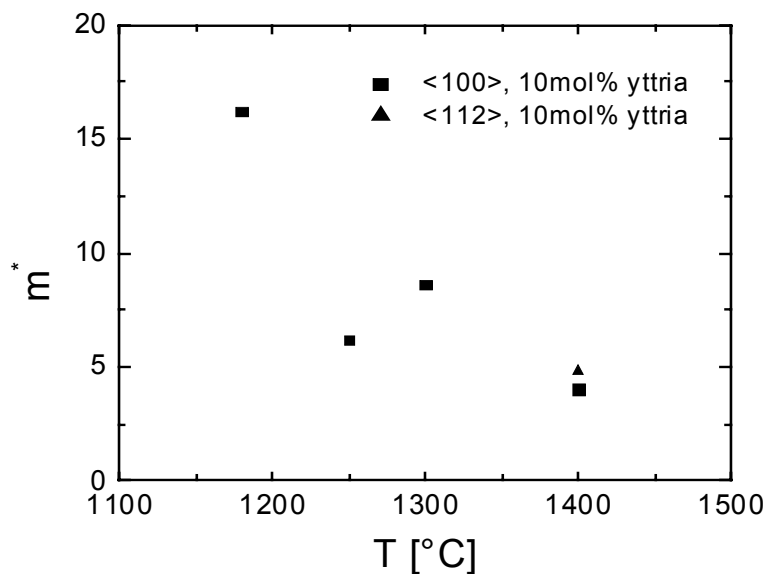
Fig. 7.2.8. The stress exponent of ZrO_2-10mol%Y_2O_3
deformed in ⟨100⟩ and ⟨112⟩ compression directions

exponent decreases from around 15 down to 5. This agrees with recovery controlled deformation, where m* should be around 4 (e.g. [92]). The activation energies are about $\Delta G = 4.8$eV and $\Delta F = 5.4$ eV. If recovery controls the deformation, the activation energy should be equal to the self-diffusion energy. In a binary material, this should be the cation diffusion. The activation energy of Zr diffusion is found to be in the range of 4.5 to 5.5 eV [32, 93, 94], thus well agreeing with the present deformation data. The diffusion coefficient decreases with increasing yttria content [95]. This should be one reason of the dependence of the flow stress on the yttria

concentration at high temperatures [26]. The recovery type of deformation at high temperatures is also expressed in the dislocation structure in Fig. 6.2.5. showing a homogeneous distribution of dislocations.

7.3. Dependence of the deformation parameters of cubic zirconia on the yttria content

In this chapter, the effect of the yttria content on the flow stress of cubic zirconia single crystals will be discussed. As shown in Fig. 7.1.1., the flow stresses of the 15 and 20mol% materials in the ⟨112⟩ compression axis are higher than that of the 10mol% material, particularly at high temperatures. Besides, these flow stresses are almost independent of the temperature in contrast to that of the 10mol% cubic zirconia single crystals. On the other hand, the strain rate sensitivity of the flow stress is virtually independent of the yttria concentration except at the highest experimental temperature. In the early papers (e.g. [27]), the concentration dependence of the deformation parameters is explained by solution hardening described in chapter 2.2., i.e. the direct interaction between dislocations and non-diffusing solutes where the contribution to the flow stress depends on the solute concentration according to eq. (2.2.15.). It is discussed for the first time in [26] that this direct influence of the solutes cannot influence the flow stress at the high temperatures of the present experiments. Part of the flow stress difference is certainly due to a different athermal contributions owing to different dislocation densities. Unfortunately, reliable dislocation density data are not available for the higher yttria concentrations.

An important issue in understanding the plastic deformation behavior of cubic zirconia with higher yttria concentrations is the occurrence of plastic instabilities, i.e. serrated flow stress region. This phenomenon was already observed in [16] for ZrO$_2$ containing 18 and 20mol%Y$_2$O$_3$ deformed along ⟨112⟩. First, the present results given in chapters 5.2. and 5.3. are briefly compared with those obtained in [16]. At 1400°C, serrations take place at a strain rate of ~10^{-5} s^{-1} for the 20mol% material. This is also the case in this work, although the corresponding flow stresses are different, being almost 400 MPa in this work and about 300 MPa in [16]. Cubic zirconia stabilized with 18mol% yttria did not yield a serrated region during an experiment done at

1400°C with 10^{-5} s^{-1} [16], and ZrO$_2$-15mol%Y$_2$O$_3$ studied at the same strain rate and temperature in this dissertation did not exhibit any serrations, either. With decreasing temperature, the occurrence of plastic instabilities was observed both in [16] and in this work for the 18 and 15mol% materials, respectively. According to the results of the stress-birefringence and TEM experiments, the glide systems engaged in slip are of the {100} type for both papers. In [16], it is stated that instabilities always occur if the flow stress exceeds 300 MPa. This does not agree with the measurements of this study at lower temperatures, where the deformation is stable again although the flow stress is high (Fig. 5.3.3.). The stability limits in [16] correspond only to the high-temperature stability border of this study.

In order to classify plastic instabilities, Estrin and Kubin [96] start by analyzing changes of the flow stress of a specimen due to changes in the plastic strain and the strain rate [97]

$$d\sigma = \Theta d\varepsilon_{pl.} + r d\ln\dot{\varepsilon} \qquad (7.3.1)$$

where Θ is the work-hardening coefficient and r is the strain rate sensitivity. Linear stability analysis leads then to the ensuing instability criterion

$$(\Theta - \sigma)/r < 0 \qquad (7.3.2)$$

Thus, instabilities can either occur if the numerator becomes negative, which are called *h* instabilities, or if r becomes negative, which are denominated strain rate-softening or *s* instabilities. Since hardening coefficients of about 2 GPa are registered for the 15mol% material, the numerator of eq. (7.3.2) is positive. In the middle of the instability range at about 1000°C, the strain rate sensitivity assumes very small values in Fig. 5.2.6., but remains positive, too, with all yttria contents. None the less, the corresponding serrations are considered to be strain rate-softening instabilities, in contrast to the conclusion in [16]. A recently refined theoretical analysis of the stability conditions [97], which considers not only localization of slip in time but also in space, shows that instabilities may occur, too, if the strain rate sensitivity is small but still positive. In the theory, it is distinguished between the instantaneous strain rate sensitivity r$_i$, which originates from the strain rate sensitivity of the dislocation mobility and is measured, e.g., at the beginning of stress relaxation tests, and a steady state strain rate sensitivity r$_s$, which results from changes in the dislocation structure and appears only after some time or strain passes after such a test start. It is measured

in strain rate change tests from the differences in the steady state levels of stress before and after the strain rate change. In accordance with the theory, r_s is close to zero as discussed in connection with Fig. 5.3.5. while r_i amounts to 5 MPa under the conditions of this figure. It may therefore be concluded that the present instabilities are essentially s instabilities where the small value of the numerator in eq. (7.3.2.) because of the low work-hardening coefficient may contribute to the unstable behavior, too. The occurrence of s instabilities is in agreement with the oscillatory behavior of the stress-strain curve and with the localization of slip presented in Figs. 6.1.3 and 6.1.4. At 1400°C, where the deformation is stable, slip is homogeneous (Fig. 6.1.5.).

The oscillatory deformation behavior during a deformation test is frequently related to dynamic strain aging (DSA). This mechanism results from the dynamic interaction of moving dislocations with diffusing point defects. The respective instabilities are usually referred to as the Portevin LeChatelier (PLC) effect. It may be caused by the Suzuki, Snoek or Cottrell effects. Mostly, the theory of the instabilities is based on the theory of the Cottrell effect. It is assumed that moving dislocations are aged while they are temporarily held up by barriers which have to be overcome by thermal activation. According to [97], the Gibbs free energy of activation of the dislocation mobility may be considered to increase with the waiting time t_w of a dislocation waiting for activation

$$\Delta G(t_w) = \Delta G_\infty - \Delta G_{DSA} \exp\left[-(\eta t_w)^\varsigma\right] - \Delta V \tau* \qquad (7.3.4.)$$

where ΔG_∞ and ΔG_{DSA} denote the free activation energy of a completely aged dislocation segment and the maximum increase of the free activation energy due to DSA, respectively, η is the characteristic rate of DSA, which is proportional to the solute mobility, and ζ is the characteristic aging exponent, depending on the strengthening mechanism and the type of diffusion. Setting $t_w = \Omega/\dot{\varepsilon}$, where Ω is an elemental strain after activation of all dislocations, introducing ΔG from eq. (7.3.4.) into the Arrhenius relation eq. (2.1.7.) and solving it for $\tau*$, one obtains the dependence of $\tau*$ on the strain rate or temperature schematically plotted in Fig. 7.3.1. At low strain rates or high temperatures, the point defect atmosphere can easily follow the dislocation. The flow stress contribution increases with increasing $\dot{\varepsilon}$ or decreasing T. Above the maximum, the atmosphere cannot follow the dislocation leading to a

decreasing flow stress contribution. Finally, the defects do not diffuse anymore in the time scale of the moving dislocation so that the defects act as localized obstacles with a positive strain rate dependence again. The figure demonstrates that at a fixed strain rate, the unstable range, i.e. that with a falling stress contribution at decreasing temperature, is embedded within two stable ranges, one at high temperatures and one at low ones. The present results in Fig. 5.3.3. show for the first time both these limits of the instability range in cubic zirconia, the high-temperature one already observed in [16] and additionally the low-temperature one.

As described in chapter 5.3., the plastic behavior during the load drops of the stress-strain curves is similar to that during the relaxation tests. As shown in Fig. 5.3.7.c, in the instability range the relaxation rate abruptly becomes zero after it falls below a critical minimum rate. This is a new phenomenon demonstrating that the dislocations become fully pinned in the instability range. Therefore, deformation rates lower than the minimum rates do not occur during the load drops of the serrations. However, the phenomenon of strain aging is obvious not only in the instability range but also during stable deformation. It was discussed already at the end of chapter 5.3. that yield drop effects appear after stress relaxation tests in the stable ranges below the unstable one (e.g. R1 in Fig. 5.3.2.a.). These yield drop effects are due to the blocking of dislocations by the dynamic strain aging. Similar effects are observed also in the
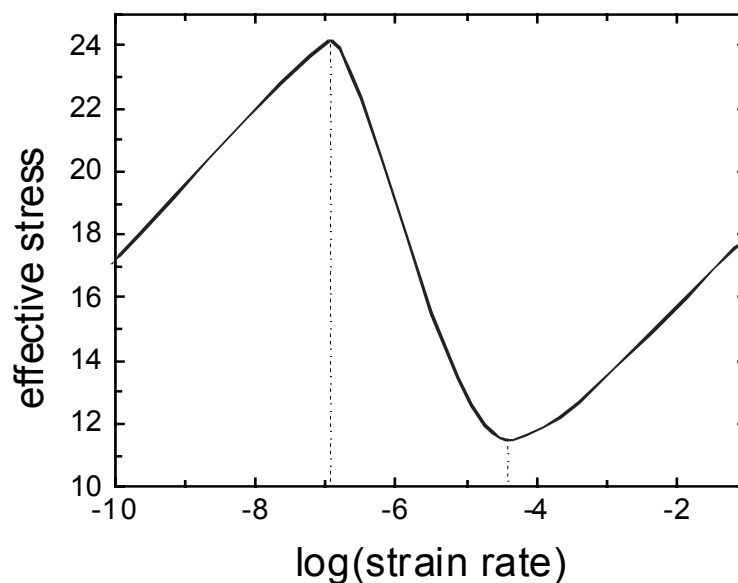
Fig. 7.3.1. Schematic diagram of the dependence of the friction stress on the strain rate or temperature caused by dynamic strain aging [97].

10mol% yttria material deformed in the $\langle 100 \rangle$ orientation in the whole range between 650°C and 1400°C, with a minimum at about 1000°C as discussed in connection with Fig. 5.1.1. They are also observed in the 10mol% material during deformation along $\langle 112 \rangle$ at temperatures below 1000°C [21]. It is demonstrated there that the amplitude of the yield drops increases with increasing aging time. The different kinds of transient effects, which occur after changing the deformation conditions, point at the occurrence of dynamic strain aging in all cubic zirconia materials. Strain aging is connected with an additional contribution to the flow stress which has never been paid attention to before. It may account for part of the difference in the flow stress between the 10mol% material and the materials containing higher concentrations of yttria. In intermetallic materials, similar diffusion processes in the dislocation cores may give rise to a flow stress anomaly, i.e. an increasing flow stress at increasing temperature (e.g. [100]). The constancy of the flow stress in the normalized diagram of Fig. 7.1.1. of the 15 and 20mol% materials below the recovery range, i.e. the missing of the usual decrease with increasing temperature, may be an expression of the flow stress anomaly connected with the dynamic strain aging.

The activation energy of 2.7 eV obtained from the Arrhenius plot of the minimum relaxation rates in Fig. 5.3.8. should correspond to the activation energy of the diffusion of the responsible point defects. The occurrence of the instabilities is clearly influenced by the yttria content of the materials. In this respect, one has to recall that the incorporation of every two yttrium ions into ZrO$_2$ necessitates the appearance of an oxygen vacancy. The yttrium ions are substitutionally solved on zirconium sites. At low temperatures, the oxygen vacancies tend to associate with the incorporated yttrium ions to form elastic dipoles along $\langle 111 \rangle$, the stress-induced reorientation of which gives rise to peaks of the internal friction [35, 31, 93]. However, these peaks are below about 400°C so that this mechanism (induced Snoek effect) cannot be the origin of the observed dynamic strain aging. Besides, direct segregation of oxygen vacancies to dislocations can also not cause the strain aging since their mobility has an activation energy of only about 1 eV [98]. Thus, most probably the yttrium ions themselves are the diffusing species giving rise to the strain aging. The activation energy of 2.7 eV from Fig. 5.3.8. is lower than the energy of yttrium diffusion of 4.4

eV [99]. This is probably due to the fact that the diffusion is of short-range character restricted to a region close to the dislocation cores.

Near 1400°C, recovery also influence the deformation of the 15 and 20mol% materials. Due to the strong dependence of the cation diffusion coefficient on the yttria concentration [95], the recovery is reduced for the materials with a higher concentration yielding a higher flow stress as discussed first in [26].

8.   Conclusions

In the scope of this thesis, a thorough investigation of the plastic deformation of cubic zirconia single crystals was done by compression experiments at a constant strain rate including stress relaxation, strain rate cycling, and temperature cycling tests. For the first time, the deformation behavior of ZrO_2-10mol%Y_2O_3 along the $\langle 100 \rangle$ compression direction, as well as of ZrO_2-15mol%Y_2O_3 and 20mol%Y_2O_3 along the $\langle 112 \rangle$ compression direction was studied in a wide temperature range between 1400°C and the lowest temperatures possible above the brittle to ductile transition. The results were compared with those obtained by other investigators who studied the deformation behavior of ZrO_2-10mol%Y_2O_3 along $\langle 112 \rangle$.

The microstructure of deformed specimens was studied by optical stress-birefringence microscopy and by transmission electron microscopy in a high-voltage electron microscope operating at 1 MeV. According to the stress-birefringence observations, {110} slip planes were activated in ZrO_2-10mol%Y_2O_3 deformed along $\langle 100 \rangle$, where the easy slip systems with {100} planes are out of stress. However, the transmission electron micrographs are mostly consistent with {111} slip planes being engaged, although some micrographs show clearly {110} slip planes, too. Since data of the anisotropic elasticity theory were not available for deformation on {110} planes, the interpretation of the deformation along the $\langle 100 \rangle$ compression axis was based on glide on {111} planes.

The flow stress of ZrO_2-10mol%Y_2O_3 deformed along $\langle 100 \rangle$ exceeds that along $\langle 112 \rangle$ at low and intermediate temperatures owing to the different slip planes activated in these specimen orientations. The difference in the flow stresses decreases with increasing temperature and vanishes at 1400°C. The processes which control the plastic deformation of cubic zirconia deformed along $\langle 100 \rangle$ were identified according to the activation parameters of deformation and the microstructural observations in the TEM. The athermal stress component arising from Taylor hardening calculated from the dislocation density is higher for the {111} planes with respect to the {100} planes because of a stronger mutual interaction between parallel dislocations. Below 600°C, the lattice friction (Peierls) mechanism acts in cubic zirconia deformed both in the

⟨100⟩ and ⟨112⟩ compression directions. This mechanism was concluded from the high values of the strain rate sensitivity leading to small activation volumes in the order of 15 b^3. Above 600°C up to 1050°C, the thermally activated overcoming of obstacles by the moving dislocations becomes dominating. Within this temperature range, the activation volume increases up to about 300 b^3 which, however, is smaller than that for deformation along ⟨112⟩. In this temperature range, the dislocations bow strongly out between the obstacles. The obstacle distances are between 200 and 500 b yielding an activation distance of a fraction of b. The obstacles are probably small precipitates containing nitrogen.

At 1000°C, the stress relaxation curves show an inverse curvature with two ranges of a different strain rate sensitivity. This points to different dislocation mechanisms responsible for the deformation behavior of cubic zirconia deformed in the ⟨100⟩ compression axis at different strain rates. One of the processes at high strain rates is the thermally activated dislocation motion discussed above. Apparently, the other mechanism is the onset of recovery where dislocations start to annihilate. The recovery becomes the dominating thermally activated process at the highest experimental temperature of 1400°C. In the recovery range, the stress exponent is about 5 and the Gibbs free energy of activation equals the cation diffusion energy, which is both consistent with recovery controlled high-temperature deformation.

The flow stresses of ZrO_2-15mol%Y_2O_3 and 20mol%Y_2O_3 along ⟨112⟩ are higher than that of ZrO_2-10mol%Y_2O_3 and do almost not depend on the temperature. Besides, a region of instabilities in the corresponding stress-strain curves occurs from about 1000°C up to 1350°C at a strain rate of 10^{-5} s^{-1}. For the first time, the lower limit of the instability range was observed for cubic zirconia. The borders of the instability range shift to higher temperatures with increasing strain rates. The instabilites are explained on account of the Portevin LeChatelier effect caused by so-called dynamic strain aging. This is a diffusional process in the dislocation cores probably of the yttrium added in order to stabilize the cubic structure of zirconia. The strain aging leads to complete locking of the dislocations below a temperature depending deformation rate. The higher flow stress of the crystals with a higher yttria content results from an additional contribution by the strain aging and, in the recovery

range, from suppressed recovery owing to the reduced diffusion coefficient by the increased yttria concentration.

9.1. Literature

1. E.M. Logothetis, ZrO_2 Oxygen Sensors in Automotive Applications, Advanced in Ceramics, 3, 1981, p. 388.

2. Hans-Heinrich Möbius, On the History of Solid Electrolyte Fuel Cells, J Sol. St. Electrochem., 1, 1997, pp.2-16.

3. 'Reaction-diffusion of fuel with air between planar solid oxide fuels cells stacked with ceramic felt', 1996, R.C. Copcutt, A.C. King & K. Kendall, Proceedings of the Royal Society A, 452, pp. 2639-2653.

4. B. Baufeld, Plastische Verformung von kubishen Zirkondioxid-Einkristallen bei Temperaturen zwischen 400°C und 1400°C, Doctoral Thesis, Halle (Saale), 1996.

5. F.F. Lange, Transformation toughening. Part 3. Experimental observations in the ZrO_2-Y_2O_3, J. Mat. Sci., 17, 1982, pp. 240-246.

6. M. Rühle, Microcrack and Transformation Toughening of Zirconia-Containing Alumina, Mat. Sci. and Eng. A 105/106, 1988, pp. 77-82.

7. A.V. Virkar, R.L.K. Matsumoto, Ferroelastic Domain Switching as a Toughening Mechanism in Tetragonal Zirconia, J. Am. Ceram. Soc., 69, 1986, pp. 224-226.

8. B. Kerkwijk, E. Mulder, and H. Verweij, Zirconia-Alumina Ceramic Composites with Extremely High Wear Resistance, Adv. Eng. Mater., 1, 1999, pp. 69-71.

9. A.H. Heuer, V. Lanteri, A. Dominguez-Rodriguez, High-Temperature Precipitation Hardening Of Y_2O_3 Partially-Stabilized ZrO_2 (Y-PSZ) Single Crystals, Acta metall., 37, 1989, pp. 559-567.

10. A. Dominguez-Rodriguez and A.H. Heuer, Plastic Deformation of Y_2O_3 Stabilized ZrO_2 (YSZ) Single Crystals, Cryst. Latt. Def. and Amorph. Mat., 16, 1987, pp. 117-123.

11. D.-S. Cheong and A.H. Heuer, High-temperature plastic deformation of Y_2O_3-stabilized ZrO_2 single crystals: Part I. The origin of the yield drop and associated glide polygonization, Phil. Mag. A, 1989, 60, pp. 107-121.

12. D.-S. Cheong, A. Dominguez-Rodriguez and A.H. Heuer, High-temperature plastic deformation of Y_2O_3-stabilized ZrO_2 single crystals: Part II. Electron microscopy studies of dislocation substructures, Phil Mag. A, 1989, 60, pp. 123-138.

13. D.-S. Cheong, A. Dominguez-Rodriguez and A.H. Heuer, High-temperature plastic deformation of Y_2O_3-stabilized ZrO_2 single crystals: Part III. Variation in work hardening between 1200 and 1500°C, Phil. Mag. A, Vol. 63, 3, pp. 377-388.

9.1. Literature

14. A. Dominguez-Rodriguez, D.-S. Cheong and A.H. Heuer, High-temperature plastic deformation of Y_2O_3-stabilized ZrO_2 single crystals: Part IV. The secondary slip systems, Phil. Mag. A, 1991, 64, pp. 923-929.

15. Pascal Teracher, Proprietes Mecaniques de la Zircone Cubique Monocristalline: Dislocations et Plasticite, Doctoral Thesis, France, 1990.

16. K. J. McClellan, A.H. Heuer and L.P. Kubin, Localized Yielding During High Temperature Deformation of Y_2O_3-Fully-Stabilized Cubic ZrO_2 Single Crystals, Acta mater., 44, pp. 2651-2662.

17. U. Messerschmidt, B. Baufeld and D. Baither, Plastic Deformation of Cubic Zirconia Single Crystals, Key Engineering Materials, Vols. 153-154, 1998, pp. 143-182.

18. B. Baufeld, U. Messerschmidt, D. Baither, M. Bartsch, A. Foitzik, and M. Rühle, Plastic Deformation of Zirconia Single Crystals by In Situ Straining Experiments in an HVEM at 1150°C, Plastic Deformation of Ceramics, edited by R.C. Bradt, C.A. Brooks, and J. Routbort, Plenum Press, New York and London 1995, p.43.

19. B. Baufeld, D. Baither, M. Bartsch, and U. Messerschmidt, Plastic Deformation of Cubic Zirconia Single Crystals at 1400°C, phys. stat. sol. a, 166, 1998, pp. 127-153.

20. B. Baufeld, U. Messerschmidt, M. Bartsch and D. Baither, Plasticity of Cubic Zirconia between 700°C and 1150°C observed by Macroscopic Compression and by In Situ Tensile Straining Tests, Key Engineering Materials, 97-98, 1994, pp. 431-436.

21. B. Baufeld, M. Bartsch, U. Messerschmidt and D. Baither, Plastic Deformation of Cubic Zirconia at Temperatures between 1150 and 700°C, Acta metall. mater., 43, pp. 1925-1993.

22. U. Messerschmidt, D. Baither, B. Baufeld, M. Bartsch, Plastic deformation of zirconia single crystals: a review, Mat. Sci. Eng., A233, 1997, pp. 61-74.

23. A. Dominguez-Rodriguez, A.H. Heuer, J. Castaing, Dislocations and the mechanical properties of stabilized ZrO_2, Rad. Def. and Def. in Sol., 119-121, 1991, pp. 759-769.

24. D. Holmes, A.H. Heuer, P. Pirouz, Dislocation structures around Vickers indents in 9.4mol%Y_2O_3 - stabilized cubic ZrO_2 single crystals, Phil. Mag. A, 67, 1993, pp. 325-342.

25. B.Ya. Farber, A.S. Chiarelli, A.H. Heuer, A dislocation mechanism of crack nucleation in cubic zirconia single crystals, Phil. Mag. A, 70, 1994, pp. 201-217.

26. U. Messerschmidt, B. Baufeld, K.J. McClellan, A.H. Heuer, Stress relaxation and solid solution hardening of cubic ZrO_2 single crystals, Acta metall. mater., 43, 1995, pp. 1917-1923.

9.1. Literature

27.   A. Dominguez-Rodriguez, K.P.D. Lagerlöf, and A.H. Heuer, Plastic Deformation and Solid-Solution Hardening of Y_2O_3-Stabilized ZrO_2, J. Am. Ceram. Soc., 69, 1986, pp. 281-284.

28.   H.M. Kandil, J.D. Greiner, and J.F. Smith, Single-Crystal Constants of Yttria-Stabilized Zirconia in the Range 20°C to 700°C, J. Am. Ceram. Soc., 67, 1984, pp. 341-346.

29.   H.G. Scott, Phase relationship in the yttria-rich part of the yttria-zirconia system, J. Mat. Sci., 13, 1977, pp. 311-316.

30.   M.L. Mecartney, W.T. Donlon, A.H. Heuer, Plastic deformation in CaO-stabilized ZrO_2 (CSZ), J. Mat. Sci., 15, 1980, pp. 1063-1065.

31.   M. Weller, A. Lakki, Defects in Cubic Zirconia Studied by Mechanical Loss Spectroscopy, Phys. Chem., 101, 1997, pp. 1297-1302.

32.   M. Kilo, G. Borchardt, S. Weber, S. Scherrer, K. Tinschert, Zirconium and Calcium Tracer Diffusion in Stabilized Cubic Zirconia, Ber. Bunsenges. Phys. Chem. 101, 1997, pp. 1361-1365.

33.   N.H. Andersen, K. Clausen, M.A. Hackett, W. Hayes, M.T. Hutchings, J.E. Macdonald, R. Osborn, The defect structure of yttria-stabilized zirconia, studied by quasielastic diffuse neutron scattering, Physica 136B, 1986, pp. 315-317.

34.   R. Osborn, N.H. Andersen, K. Clausen, M.A. Hackett, W. Hayes, M.T. Hutchings, J.E. MacDonald, Neutron Scattering Investigations of the Defect Structure of Y_2O_3-stabilized ZrO_2 and its dynamical behaviour at high temperatures, Mat. Sci. For., 7, 1986, pp. 55-62.

35.   M. Weller, Atomic Defects in Yttria - and - Calcia - stabilized Zirconia, Z. Metallkd. 84, 1993, pp. 381-386.

36.   H. G. Van Bueren, Imperfections in Crystals, North-Holland Publishing Company, Amsterdam, 1961.

37.   Schmidt, E. and W. Boas, Kristallplastizität, Springer, Berlin, 1935.

38.   D. Hull and D.J. Bacon, Introduction to Dislocations, Pergamon, 1994.

39.   G. Schoek, The Activation Energy of Dislocation Movement, phys. stat. sol. 8, 1965, pp. 499-507.

40.   A.G. Evans and R.D. Rawlings, The Thermally Activated Deformation of Crystalline Materials, phys. stat. sol. 34, 1969, pp. 9-31.

41.   G.B. Gibbs, The Thermodynamics of Creep Deformation, phys. stat. sol. 5, 1964, pp. 693-695

42.   G.B. Gibbs, The Thermodynamics of Thermally-Activated Dislocation Glide, phys. stat. sol. 10, 1965, pp. 507-512.

9.1.   Literature

43.   G.B. Gibbs, The Activation Parameters for Dislocation Glide, 16, 1967, pp. 97-102.

44.   J.P. Hirth, J. Lothe, Theory of Dislocations, McGraw-Hill, New York 1968,

45.   T. Suzuki, S. Takeuchi, H. Yoshinaga, Dislocation Dynamics and Plasticity, Springer Verlag, 1991.

46.   B. Baufeld, B.V. Petukhov, M. Bartsch, U. Messerschmidt, Transition of Mechanism Controlling the Dislocation Motion in Cubic ZrO_2 below 700°C, Acta mater., 46, 1998, pp. 3077-3085.

47.   B.V. Petukhov, M. Bartsch, U. Messerschmidt, Temperature dependence of the flow stress and the strain rate sensitivity at the transition from the Peierls mechanism to pinning by localized obstacles, Eur. Phys. J., AP 9, 2000, pp. 89-95.

48.   A. Seeger, Dislocations, CNRS, Paris, 1984.

49.   P. Haasen, Solution Hardening in f.c.c. Metals, in: Dislocations in Solids, Vol. 4, ed. by F.R.N. Nabarro, North-Holland Publ., Amsterdam 1979, p. 155-260.

50.   R. Labusch, A Statistical Theory of Solid Solution Hardening, phys. stat. sol. 41, 1970, pp. 659-669.

51.   V. Gerold, Precipitation Hardening, in: Dislocations in Solids, 4, ed. by F.R.N. Nabarro, North-Holland Publ., Amsterdam 1979, pp. 219-260.

52.   J. Friedel, Dislocations, Pergamon, Oxford, 1964.

53.   U. Messerschmidt, Lectures, Realstruktur und Festigkeit von Werkstoffen, Halle/Saale, 1988.

54.   L. V. Azarov, Introduction to Solids, McGraw-Hill Book Company Inc., 1960

55.   M. Liu and B. Evans, Dislocation recovery kineticks in single-crystal calcite, J. Geoph. Res., 102, 1997, pp. 24801-24809.

56.   S. Takeuchi, A.S. Argon, Steady-state creep of a single-phase crystalline matter at high temperature, J. Mat. Sci., 11, 1976, pp. 1542-1566.

57.   P.P. Gillis, J.J. Gilman, Dynamical Dislocation Theory of Crystal Plasticity. I. The Yield Stress, J. Appl. Phys., 36, pp. 3370-3380.

58.   P.P. Gillis, J.J. Gilman, Dynamical Dislocation Theory of Crystal Plasticity. II. Easy Glide and Strain Hardening, J. Appl. Phys., 36, pp. 3380-3386.

59.   R.W. Cahn, P. Haasen, Physical Metallurgy, North-Holland Physics Publishing, part II, 1983.

60.   U.F. Kocks, Laws for Work-Hardening and Low Temperature Creep, J. Eng. Mater. Technol., 98, 1976, pp. 76-85.

61.   F. Guiu, P.L. Pratt, Stress Relaxation and the Plastic Deformation of Solids, phys. stat. sol. 6, 1964, pp. 111-120.

9.1. Literature

62. U. Kocks, A. S. Argon, M. F. Ashby, Thermodynamics and Kinetics of Slip, Pergamon Press, 1975.

63. K.J. McClellan, S.-Q. Xiao, K.P.D. Lagerhof and A.H. Heuer, Determination of the Structure of the Cubic Phase in High-ZrO_2 Y_2O_3-ZrO_2 Alloys by CBED, Phil. Mag. A, 70, 1994, 185.

64. H.G. Scott, Phase relationships in the zirconia-yttria system, J. Mat. Sci., 10, 1975, pp. 1527-1535.

65. B. Ya. Farber, A.S. Chiarelli, and A.H. Heuer, Dislocation velocities in cubic zirconia (ZrO_2) single crystals, Phil. Mag. A, 72, 1995, pp. 59-80.

66. E.H. Kisi, C.J. Howard, Crystal Structures of Zirconia Phases and their Inter-Relation, Zirconia Engineering Ceramics, edited Erich Kisi, Trans Tech Publications LTD, 1998.

67. C.J. Howard, R.J. Hill, The polymorphs of zirconia: phase abundance and crystal structure by Rietveld analysis of neutron and X-ray diffraction data, J. Mat. Sci., 26, 1991, pp. 127-134.

68. P. Li, I-Wei Chen, J. E. Penner-Hahn, X-ray-absorption studies of zirconia polymorphs. II. Effect of Y_2O_3 dopant on ZrO_2 structure, Phys. Rev. B, 48, 1993, pp. 10074-10081.

69. R.P. Ingel, D. Lewis III, Elastic Anisotropy in Zirconia Single Crystals, J. Am. Ceram. Soc., 71, 1988, pp. 265-271

70. M. Hayakawa, H. Miyauchi, A. Ikegami, M. Nishida, Elastic Constants of Zirconia Single Crystals Determined by X-ray Measurements for Polycrystals, Mat. Trans., JIM, 39, 1998, pp. 268-274.

71. P.J. Botha, J.C.H. Chiang, J.D. Comins, P.M. Mjwara, P.E. Ngoepe, Behavior of elastic constants, refractive index, and lattice parameter of cubic zirconia at high temperatures, J. Appl. Phys. 73, 1993, pp. 7268-7274.

72. W.M. Sherry, J.B. Vander Sande, TEM investigation of the plastic deformation behaviour of calcium fluorite, Phil. Mag. A, 40, 1979, pp. 77-95.

73. R.J. Keller, T.E. Mitchell, A.H. Heuer, Plastic deformation in nonstoichiometric UO_{2+x} single crystals - I. Deformation at low temperatures, Acta metall. 36, 1988, pp. 1061-1071.

74. A.G. Evans and P.L. Pratt, Dislocations in the Fluorite Structure, Phil. Mag., 31, 1969, pp. 1213-1237.

75. D. Gomez-Garcia, J. Martinez-Fernandez, A. Dominguez-Rodriguez, P. Eveno, J. Castaing, Deformation Mechanisms for High-Temperature Creep of High Yttria Content Stabilized Zirconia Single Crystals, Acta mater., 44, 1996, pp. 991-999.

9.1.   Literature

76.   D. Gomez-Garcia, J. Martinez-Fernandez, A. Dominguez-Rodriguez, J. Castaing, Mechanisms of High-Temperature Creep of Fully Stabilized Zirconia Single Crystals as a function of the Yttria Content, J. Am. Ceram. Soc., 80, 1997, pp. 1668-1672.

77.   J. Martinez-Fernandez, M. Jimenez-Melendo, A. Dominguez-Rodriguez, A. H. Heuer, High-Temperature Creep of Yttria Stabilized Zirconia Single Crystals, J. Am. Cer. Soc., 73, 1990, pp. 2452-2456.

78.   P. Teracher, H. Garem and J. Rabier, Dislocation mobilities and plastic deformation of ZrO_2 single crystals, Strength of Metals and Alloys, ed. by D.G. Brandon, R. Chaim and A. Rosen, Freund Publs. London 1991, p. 217 223.

79.   D. Gomez-Garcia, J. Martinez-Fernandez, A. Dominguez-Rodriguez, K.H. Westmacott, Zirconium Nitride Precipitation in Nominally Pure Yttria-Stabilized Zirconia, J. Am. Ceram. Soc., 79, 1996, pp. 487-490.

80.   D. Gomez-Garcia, J. Martinez- Fernandez, A.Dominguez-Rodriguez, K.H. Westmacott, On the influence of heat behaviour of yttria fully stabilized single crystals, Phil. Mag. A, 79, 1999, pp. 1839-1852.

81.   D. Gomez-Garcia, J. Martinez-Fernandez, A. Dominguez-Rodriguez, K.H. Westmacott, On the nature of electron-beam induced loop formation on dislocations in yttria fully-stabilized zirconia, Phil. Mag. A, 73, 1996, p. 681.

82.   Instron, *Instron Model 8500, Instructions for use*, Issues A, B, C, 1990, 1993, 1995.

83.   National Instruments, NI-488.2 Software Reference Manual for MS-DOS, 320282-01, March 1992.

84.   Severn Furnaces Limited, Operating Instr., Furnace Model MDS 1003, Control System CU 1003.

85.   Electron Microscope JEM 1000, Instruction Manual, JEOL CO., LTD.

86.   M. von Heimendahl, Electron Microscopy of Materials, Academic Press, 1980.

87.   Direct observation of imperfections in crystals, ed. by J.B. Newkirk, J.H. Wernick, Interscience Publishers, 1962.

88.   T.J. Marrow, S.G. Roberts & A.K. Pearce-Higgins, The Brittle/Ductile Transition in Cubic Stabilized Zirconia, J. Europ. Ceram. Soc., 14, 1994, pp. 447-453.

89.   J. Lankford, Deformation and fracture of yttria-stabilized zirconia single crystals, J. Mater. Sci., 21, 1986, pp. 1981-1989.

90.   D. Baither, B. Baufeld, U. Messerschmidt, M. Bartsch, HVEM high-temperature in situ straining experiments on cubic zirconia single crystals, Mat. Sci. Eng. A 233, 1997, pp. 75-87.

9.1.   Literature

91.   F. Appel M. Bartsch, U. Messerschmidt, E.M. Nadgornyi, S.N. Valkovskii, Dislocation Motion and Plasticity in MgO Single Crystals, Phys. Status Solidi A 83, 1984, pp. 179-194.

92.   W.R. Cannon, T.G. Langdon, Creep of ceramics, Part 1, Mechanical characteristics, J. Mater. Sci. 18, 1983, p. 1-50.

93.   A. Lakki, R. Herzog, M. Weller, H. Schubert, C. Reetz, O. Görke, M. Kilo, G. Borchardt, Mechanical loss, creep, diffusion and ionic conductivity of ZrO_2-8mol%Y_2O_3 polycrystals, J. Ecers 20 (2000), pp. 285-296.

94.   M. Kilo, C. Funderberger, G. Borchardt, R. Herzog, A. Lakki, M. Weller, S. Weber, S. Scherrer, Oxygen and host cation transport in yttria stabilized zirconia, subm. To J. Am. Ceram. Soc.

95.   F.R. Chien and A.H. Heuer, Lattice diffusion kinetics in Y_2O_3-stabilized cubic ZrO_2 single crystals: a dislocation loop annealing study, Phil. Mag. A, 73, 1996, pp. 681-697.

96.   L.P. Kubin and Y. Estrin, Evolution of Dislocation Densities and the Critical Conditions for the Portevin-Le Chatelier Effect, Acta metall. Mater., 38, 1990, pp. 697-708

97.   M. Zaiser, P. Hähner, Oscillatory Modes Of Plastic Deformation: Theoretical Concepts, Phys. Stat. Sol. (b) 199, 1997, p. 267.

98.   Y. Oishi and K. Ando, Oxygen self-diffusion in cubic ZrO_2 solid solutions, Transport in Nonstoichiometric Compounds, ed. by G. Simkovic and V.S. Stubican, Plenum Publ., 1985, p. 189

99.   Y. Oishi, K. Ando and Y. Sakka, Lattice and grain-boundary diffusion coefficients of cations in stabilized zirconias, Advances in Ceramics (edited by M.F. Yang and A.H. Heuer), 7, 1989, p. 208

100.   U. Messerschmidt, M. Bartsch, S. Guder, D. Häussler, Dislocation Dynamics During the Deformation of Intermetallic Alloys and the Flow Stress Anomaly, Mat. Res. Soc. Symp. Proc. Vol. 552, 1999.

9.2.   The list of figures

9.3.   Abbreviations

a	interplanar distance
A_o	plane of applied compressive force
$A_{sl.}$	slip plane
A	sample cross-section
$\vec{b}$	Burgers vector
b	absolute value of the Burgers vector
c	atomic fraction of foreign atoms
c_k	concentration of kinks
C_{44}, C_{11}, C_{12}	elastic constants
CRSS	critical resolved shear stress
d	shortest repeat distance along the dislocation line
$\vec{d}$	direction of compression axis
d_{sl}	distance between two slip planes
D_k	diffusion coefficient of the drift of kinks
D	diameter of an obstacle
E	Young modulus
ΔF	Helmholtz free activation energy
ΔF_k	kink formation energy
$\vec{f}_c$	compressive force
$\vec{f}_b$	force acting along the Burgers vector of a dislocation
f_r	resisting force that thermally activated obstacles exert on a dislocation line
f_{max}	maximum resisting force
f_{int}	local interaction force
f_{pin}	pinning force exerted by each particle on a dislocation
f_m	maximum force that can be sustained by a particle
f_x	interaction force between two parallel dislocations
f_{pm}	dimensionless maximum interaction force between two parallel dislocations
$\vec{g}$	vector of the reciprocal lattice (diffraction vector)
ΔG	Gibbs free energy of activation
ΔG_∞	the activation energy of a completely aged dislocation segment
ΔG_{DSA}	maximum increase of the free activation energy on account of DSA
ΔH	activation enthalpy

9.3. List of abbreviations

h	kink height
j	strain recording value of the deformation machine
κ	forward distance of a dislocation after a successful activation
k	Boltzman constant
K_s	energetical coefficient
l	obstacle spacing along the dislocation line
l_s	dislocation segment length (equals to the obstacle spacing along the dislocation line, i.e. to l)
l_d	dislocation line length
L	distance between sample and photographic plate (camera length)
m	the number of cusps occurring along the dislocation line
m*	stress exponent
m_s	orientation factor
$\vec{n}$	slip plane normal
N	number of intersections of dislocation lines and orthogonal grid lines
p_o	sample initial length
P	grid line length (dislocation density determination)
R	distance on the photographic plate between the transmitted beam and a diffraction spot
$\vec{R}$	diffraction spot position vector
r	strain rate sensitivity of the flow stress
r_i	instantaneous strain rate sensitivity
r_s	steady state strain rate sensitivity
ΔS	activation entropy
t	time
t_w	aging (waiting) time
T	temperature
$U_{fr.}$	Peierls energy
ΔU	change of internal energy
$\Delta V*$	activation volume
v	velocity of moving dislocations
ΔW	work term
x	displacement of dislocations
Δx	activation distance

y	minimum spacing between two parallel slip planes
Y_{rec}	recovery rate
α	numerical constant
ß	Bragg angle
Γ	line tension
$\dot{\varepsilon}_{st}$	steady strain rate
ε	total macroscopic strain
$\varepsilon_{el.}$	macroscopic elastic strain
$\varepsilon_{pl.}$	macroscopic plastic strain
$\dot{\varepsilon}$	total macroscopic strain rate
$\dot{\varepsilon}_{pl.}$	macroscopic plastic strain rate
$\dot{\varepsilon}_{el.}$	macroscopic elastic strain rate
$\dot{\varepsilon}_{o}$	pre-exponential factor of the Arrhenius plastic strain rate equation
ζ	characteristic aging exponent
Θ	work-hardening coefficient
ϑ	dislocation radius of curvature
η	characteristic rate of DSA
λ	electron wave length
μ	shear modulus
ν	Poisson's ratio
ρ_{m}	mobile dislocation density
ρ	total dislocation density
$\sigma_{up.}$	flow stress of the upper yield point
$\sigma_{l.}$	flow stress of the lower yield point
σ	applied stress
τ_{c}	critical resolved shear stress
τ	resolved shear stress
τ^{*}	thermal component of the shear stress (effective stress)
τ_{i}	athermal component of the shear stress
τ_{p}	stress resulting from the long-range interaction between parallel dislocations (Taylor hardening stress)
τ_{b}	back stress of bowed-out dislocation segments

9.3.   List of abbreviations

$\tau_{fr.}$ lattice friction stress (Peierls stress)

υ_k kink velocity

υ velocity of a kinked dislocation

ψ bending angle

χ frequency of dislocation oscillation

Ω elemental strain after all dislocations are activated

$\tau_{fr.}$ lattice friction stress (Peierls stress)

υ_k kink velocity

9.4.   Curriculum vitae

April 1, 1974	born in Kiev, Ukraine
09/81 – 06/91	Shevchenko Secondary School, Kiev, Ukraine
09/91 – 06/96	National Shevchenko University, Kiev, Ukraine
06/94	internship in the Institute of Material Science, Kiew, Ukraine
09/95 – 05/96	diploma project "Fractogrphy of fracture surfaces of silicon nitride (Si_3N_4)" in the Institute of Material Science, Kiev, Ukraine
	Master of Science, Physics
11/96	entering the doctoral studentship in the Institute of Material Science
03/98	Ph.D. student in the workgroup of Prof. U. Messerschmidt in Max Planck Institute of Microstructure Physics in the framework of the Graduiertenkolleg 415 "Defektstrukturbestimmte physikalische Eigenschaften," Martin-Luther-Universität, Halle-Wittenberg

9.5.   Sincerity statement

I hereby assure that the submitted dissertation:

Plastic deformation of cubic zirconia single crystals: the influence of the orientation of compression axis and yttria stabilizer content

is composed by myself alone, and that all the indicated references are rightly and truly stated. In this dissertation, no other scientific papers were quoted.

Alexander Tikhonovsky

Halle, 07 February, 2001

9.6.   Acknowledgements